UNIVERSITY OF SOUTHAMPTON

Improving fishing vessel stability assessment using cost-effective computing technologies.

by

Nana O.K. Abankwa

A thesis submitted for the degree of
Doctor of Philosophy

in the
Faculty of Engineering and Physical Sciences
Computational Engineering and Design Group

May 2021

UNIVERSITY OF SOUTHAMPTON

ABSTRACT

FACULTY OF ENGINEERING AND PHYSICAL SCIENCES
COMPUTATIONAL ENGINEERING AND DESIGN GROUP

Doctor of Philosophy

IMPROVING FISHING VESSEL STABILITY ASSESSMENT USING COST-EFFECTIVE COMPUTING TECHNOLOGIES.

by Nana O.K. Abankwa

Fishing is one of the most dangerous jobs in the United Kingdom (UK). This work's contribution to knowledge lies in the novel application of cost-effective, off-the-shelf single-board computers (SBCs) coupled with inertial measurement units (IMUs) to the stability assessment of small fishing vessels. This thesis aims to demonstrate how readings from low-cost, off-the-shelf SBCs and IMUs can be used in a roll period test and an inclining test to accurately determine a vessel's roll period and metacentric height respectively.

The results show that cheap SBCs coupled with IMUs can be used to accurately determine a vessel's roll period with an uncertainty of less than 0.1. The cost-effective technologies also provide additional information on roll amplitude that is not available if only a stopwatch is used in the roll period test. When it comes to the ability of the cost-effective technologies to determine changes to a vessel's stability in waves as weights are moved vertically onboard, the results show that the cost-effective technologies do not detect changes in the vessel's roll period but rather record the encounter period of the vessel with the waves in its operating conditions. This is to within 0.02 seconds when compared to results from the potentiometer. Even though no changes in roll period due to weight movements were detected, increases in roll amplitude were detected as the heights of the weights increased. In regards to using cost-effective technologies in inclining tests to determine a vessel's metacentric height, the results show that the cost-effective technologies accurately detect the heel angle due to weight shifts. The metacentric height obtained is further validated by comparing the roll period obtained by a roll period test of the vessel and the roll period calculated using the calculated GM. Finally, measurements from the cost-effective technologies compared with measurements from a state-of-the-art optical motion capture system and a more expensive industrial IMU confirm the potential of the cost-effective technologies in aiding the assessment of fishing vessel stability.

Accurate knowledge of a vessel's roll period and metacentric height is critical to vessel stability and safety. It is hoped that this thesis informs the fishing industry of how cost-effective technologies can be used to assess vessel stability to provide information on roll period and metacentric height.

Improving fishing vessel stability assessment using cost-effective computing technologies.

When referring to this work, full bibliographic details including the author, title, awarding institution and date of the thesis must be given, i.e. Nana O. K. Abankwa, 2021, ‘Improving fishing vessel stability assessment using cost-effective computing technologies’, PhD thesis, University of Southampton.

Contents

Appendices

List of Figures

List of Tables

Nomenclature

2D	two-dimensional
3D	three-dimensional
ASV	autonomous surface vehicle
AIS	automatic identification system
B	centre of buoyancy
BM	height of the metacentre above the centre of buoyancy
CDIP	coastal data information programme
DOF	degrees of freedom
G	centre of gravity
GM	height of the metacentre above the centre of gravity
GUI	graphical user interface
GZ	righting lever
I	moment of inertia
I2C	inter-integrated circuit
IMU	inertial measurement unit
K	keel
KB	height of the centre of buoyancy above the keel
KM	height of the metacentre above the keel
KG	height of the centre of gravity above the keel
M	metacentre
MEMS	micro-electro-mechanical systems
RM	righting moment
SBC	single-board computer
SD	secure digital
SPI	serial peripheral interface
SSH	secure shell
UART	universal asyncronous receiver/transmitter
VTS	vessel traffic service
WAFO	wave analysis for fatigue and oceanography
WPA	wi-fi protected access

Declaration of Authorship

I, Nana O. K. Abankwa, declare that the thesis titled '*Improving fishing vessel stability assessment using cost-effective computing technologies*' and the work presented in the thesis are both my own, and have been generated by me as the result of my original research. I confirm that:

- this work was done wholly or mainly while in candidature for a research degree at this University;
- where any part of this thesis has previously been submitted for a degree or any other qualification at this University or any other institution, this has been clearly stated;
- where I have consulted the published work of others, this is always clearly attributed;
- where I have quoted from the work of others, the source is always given. With the exception of such quotations, this thesis is entirely my work;
- I have acknowledged all main sources of help;
- where the thesis is based on work done by myself jointly with others, I have made clear exactly what was done by others and what I have contributed myself;
- parts of this work have been published as:
  - Abankwa, N. O., Johnston, S. J., Scott, M., and Cox, S. J. 'Ship motion measurement using an inertial measurement unit'. In *2015 IEEE 2nd World Forum on Internet of Things (WF-IoT)*, pages 375 - 380, Milan, Italy, 14 - 16 Dec 2015. doi:10.1109/WF-IoT.2015.7389083.
  - Abankwa, N. O., Squicciarini, G., Johnston, S. J., Scott, M., and Cox, S. J. 'An evaluation of the use of low-cost accelerometers in assessing fishing vessel stability through period of heave motion'. In *2016 International Conference for Students on Applied Engineering (ICSAE)*, pages 59 - 63, Newcastle upon Tyne, UK, 20 - 21 Oct 2016. doi:10.1109/ICSAE.2016.7810161.
  - Abankwa, N. O., Bowker, J., Johnston, S. J., Scott, M., and Cox, S. J. 'Estimating the Longitudinal Centre of Flotation of a Vessel in Waves using Acceleration Measurements'. *IEEE Sensors Journal*, 2018. doi:10.1109/JSEN.2018.2865463.

- parts of this work have been submitted for publication as:
  - Abankwa, N. O., Bowker, J., Johnston, S. J., Scott, M., and Cox, S. J. ‘Measurement of vessel pitch: comparison between low-cost single-board computer, industry standard inertial measurement unit, and an optical motion capture system’. *IEEE Sensors Journal.*
- parts of this work have also been presented as:
  - Abankwa, N. O., Johnston, S. J., Scott, M., and Cox, S. J. ‘Estimation of sea state from measured ship response’. *5th Student Conference on Complexity Science (SCCS2015)*, Granada, Spain, 9 - 11 Sept 2015.

Signed: ....

Date: ....

Acknowledgements

I would like to firstly thank Professor Simon Cox and Steven Johnston for their supervision and support throughout my research. I am also incredibly grateful to Mark Scott for his technical expertise and proofreading. Additionally, I would like to thank Gereon Kaiping, Andrew Poulter, Lasse Wollatz, Mihaela Apetroaie-Cristea, Florentin Bulot and Philip Basford for the insightful discussions during our weekly group meetings.

I would also like to thank Giacomo Squicciarini with whom I had useful discussions on collecting and analysing the data used in comparing accelerometers, and Bertrand Malas, James Bowker, Florentin Bulot and Philip Basford for helping me organise experiments in the Bolderwood towing tank.

Last but not least, I would like to thank my family and friends for all the encouragement and moral support throughout this degree.

This project is funded by the Engineering and Physical Sciences Research Council (EPSRC reference number 1368760).

Chapter 1

Introduction

This chapter provides the background and motivation for this research based on two key points: fishing being one of the most dangerous jobs in the world, and how advances in single-board computers (SBCs) might improve the assessment of fishing vessel stability. Next, this work's primary aim and research questions are presented. Finally, the chapter concludes with an outline showing the structure of this thesis.

1.1 Background and motivation

The sea hosts one of the most dangerous jobs in the world: fishing (Chauvin et al., 2017). Historically, fishing has had and continues to have high mortality rates compared to other industries. In Great Britain between 1976 and 1995, 454 fishermen died from accidents at work and fishermen were 52.4 times more likely to have a fatal accident at work compared to other occupations (Roberts, 2002). The number of accidents between 1976 and 1995 corresponded to a rate of 103.1 per 100,000 worker-years (Figure 1.1). This was the highest fatality rate and double the second highest fatality rate. During their working lives, fishermen in Britain have a one in twenty chance of being killed on the job (British Broadcasting Corporation, 2010). Even though there have been fewer work-related deaths in fishing in recent decades, mortality rates remain high compared to other industries (US Bureau of Labour Statistics, 2017).

This work focuses on vessel's less than 15 m in overall length (small vessels) as large vessels cope with dangerous operating conditions better and are more likely to have expensive state-of-the-art systems to help improve safety. In 2016, fishing vessels lost during operation had an average age of 30 years, and a majority of these were under 15 m in overall length as seen in Table 1.1 (Marine Accident Investigation Branch, 2017). A vessel operator's approach to fishing is typically developed through extensive experimentation over time (McGoodwin, 2001). This combined with the average age of fishing vessels suggests that fishing vessels have not fully benefitted from recent advancements in technology.

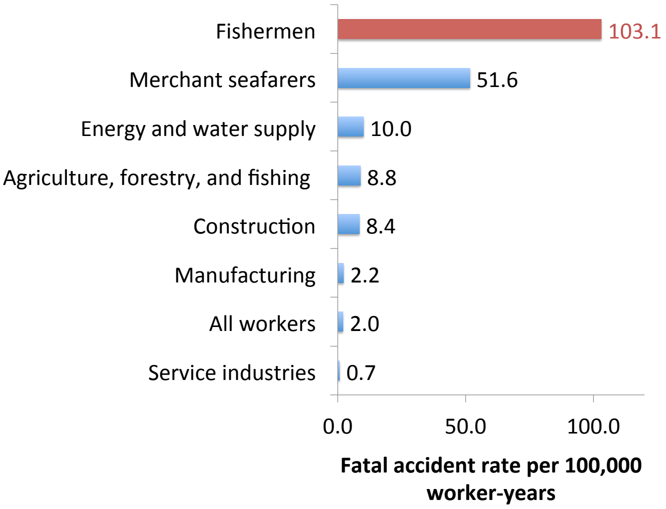

FIGURE 1.1: UK mortality rates for accidents at work in main industrial sectors, 1976-1995. Adapted from *Hazardous Occupations in Great Britain,* by Roberts (2002)

TABLE 1.1: UK fishing vessel losses grouped by vessel length from 2012 to 2016. Adapted from *MAIB Annual Report* by Marine Accident Investigation Branch (2017)

	Under 15m	15m to less than 24m	Over 24m
2012	5	4	-
2013	15	3	-
2014	9	3	-
2015	8	5	-
2016	5	2	1

It is not surprising that the majority of fishing boats lost were under 15 m in overall length (LOA) because in 2016 a majority of the UK fishing fleet consisted of vessels of 15 m and under in overall length as illustrated in Figure 1.2 (Marine Management Organisation, 2017).

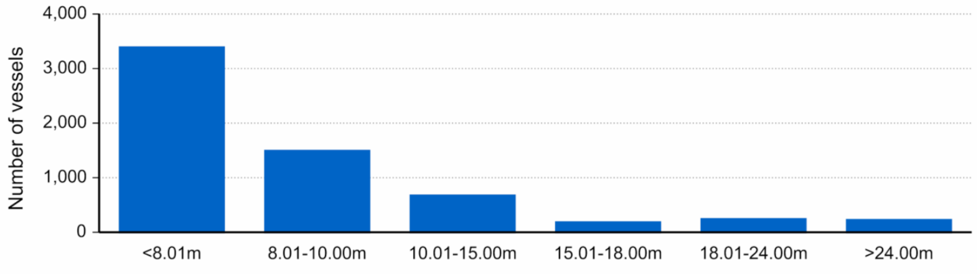

FIGURE 1.2: Overall length of vessels in UK fishing fleet in 2016. Adapted from *UK Sea Fisheries Statistics* by Marine Management Organisation (2017)

A vessel's safety at sea is affected by the vessel's seaworthiness and stability. These have been identified as factors causing many small fishing vessel accidents (Marine Accident Investigation

Branch, 2008). Examples of fishing vessel accidents related to stability include the capsize of *Stella Maris* (9.9 m) in July 2014, and the capsize of *FV JMT* (11.4 m) in July 2015 (Scarponi, 2017). Even though both of these incidents illustrate that small vessels are particularly vulnerable to a loss of stability, 'vessels under 15 m LOA are not currently required to have approved stability that is compliant with statutory requirements. There is presently no intention to introduce statutory requirements for vessels under 12 m registered length' (Maritime and Coastguard Agency, 2010). To reduce costs, fishermen do not purchase expensive safety-related equipment unless it is a legal requirement.

Safety risks can be reduced through the use of vessel motion monitoring systems (Enshaei, 2013), some of which use inertial sensors to measure a vessel's motion during operation (Nunez et al., 2017; Jiao et al., 2017), for assessment of vessel stability. Since there are no statutory stability requirements from regulators for small vessels, stability guidance systems are not conventional for small vessels (Gonzalez et al., 2012). Even though such systems have been used by larger vessels such as cruise ships and ferries, a lack of regulatory compliance and high costs have prevented the development of such systems for fishing vessels. Cost-effective computing technologies such as single-board computers (SBCs) can be used to improve the assessment of vessel stability for small fishing vessels. A reduction in the cost of computing hardware has resulted in the increased application of such devices to solving a large number of problems in a wide range of sectors including home automation, wireless sensor networks, and environmental monitoring. These devices have even been used to build supercomputers (Figure 1.3). It is now cheap enough to use commodity off-the-shelf computing hardware to develop stability assessment solutions for the fishing industry.

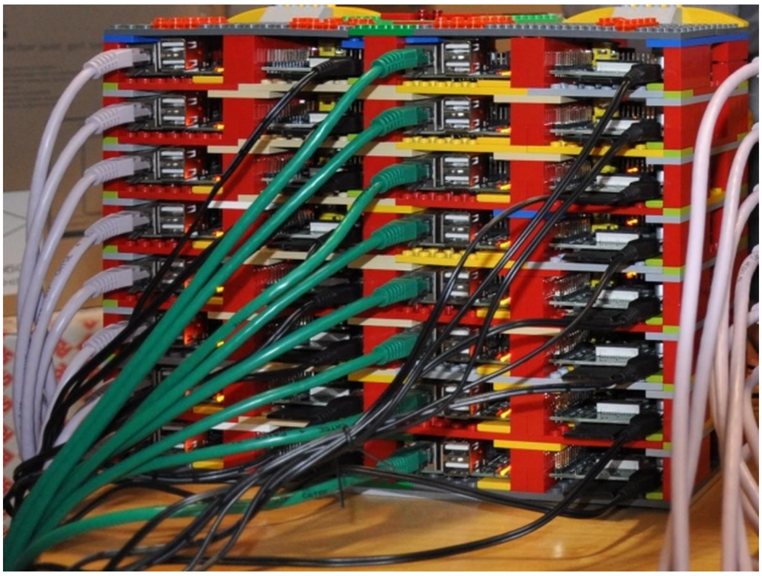

FIGURE 1.3: A supercomputer built using SBCs.
Adapted from *Iridis-Pi: A low-cost, compact demonstration cluster.* by Cox et al. (2014)

This thesis contributes to the field of study and industry by investigating the novel application of cost-effective single-board computers (SBCs) in assessing changes in vessel parameters related to stability (roll period and metacentric height).

1.2 Aims and research questions

Based on the previous section, this work focuses on improving assessment of stability of fishing vessels under 15 m in overall length by demonstrating that cost-effective single-board computers (SBCs) are capable of assessing changes in vessel parameters related to stability (roll period and metacentric height). This thesis shows how SBCs can provide information which fishing vessel operators can objectively use to determine the safety level of vessels and make decisions. It is not intended that a system would automatically make decisions but rather only act as an advisor.

In order to achieve this research's aim, we investigated fundamental questions including:

1. How capable are cost-effective computing technologies in determining changes in roll period, a key parameter for vessel stability and how does this compare to calibrated test equipment?
2. To what extent can cost-effective computing technologies be used to able to assess changes in roll period due to movements of weights in waves?
3. How capable are cost-effective computing technologies in determining a vessel's metacentric height through an inclining test?
4. How do cost-effective computing technologies compare to existing, more expensive methods of measuring vessel motion?

In order to address these questions a number of towing tank experiments were conducted. Firstly, in Chapter 4 a model vessel was induced to roll for a range of roll periods to compare how the cost-effective technologies compare with traditional methods of assessing roll period in a towing tank using a potentiometer. This experiment helped address the first question related to the capability of cost-effective technologies in determining changes in roll period. Next, the second question was addressed in Chapter 5 using the same model to conduct an experiment in which weights were shifted vertically on the vessel. Since the shifting of weights on a vessel affects the vessel's stability, this second experiment was conducted in order to determine whether cost-effective technologies can determine changes in the vessel's stability due to movements of weights. The third research question was addressed in Chapter 6 in which an inclining test was conducted to demonstrate how results from the cost-effective computing technologies can be used in determining the vessel's metacentric height. A final towing tank experiment was conducted in Chapter 7 in order to determine how the cost-effective technologies compare against a state-of-the-art optical motion capture system and a more expensive industrial IMU in measuring vessel motion.

1.3 Thesis outline

The thesis is structured as follows:

Chapter 2, 'Literature review': This chapter discusses vessel motion, stability, and methods to assess stability including the use of the righting lever (GZ) curve, roll period, and the metacentric height. Tools for assessing vessel stability and measuring motion are introduced, and each of their advantages and disadvantages are considered.

Chapter 3, 'Functional and technical requirements': This chapter follows on from the identification of the roll period and metacentric height as means of assessing stability, especially for fishing vessels. It presents the hardware and software setup of the devices used in later chapters to assess roll period and metacentric height.

Chapter 4, 'Detection of changes in roll period': This chapter assesses the ability of the low-cost devices to accurately determine the roll periods of a model vessel in a wave tank. This chapter also discusses how the results scale up to actual size and the ability of the low-cost devices to be used at full-scale.

Chapter 5, 'Ability to detect vertical weight shifts in waves': Following on from the identification of changes in weight distribution as a parameter important to stability in Chapter 2. This chapter assesses whether movement of weights as the model vessel operates in waves can be detected by cost-effective technologies.

Chapter 6, 'Ability to detect horizontal weight shifts': This chapter assesses the ability of low-cost devices to determine the metacentric height of the model vessel. The calculated metacentric height is further validated by using it to compute a roll period and then comparing the computed roll period with a roll period determined from a roll period test.

Chapter 7, 'Comparison between cost-effective technologies and the state-of-the-art': This chapter compares an optical motion capture system with the cost-effective technologies and a commodity industry-standard IMU. This is done to assess the suitability of replacing the state-of-the-art methods of measuring vessel motion with cost-effective computing technologies.

Chapter 8, 'Conclusions and further work': Finally, this chapter discusses the work presented in this thesis and whether the research questions were answered. This chapter also shows the direction of further work.

Chapter 2

Literature review

To provide context on how cost-effective computing technologies can be used to improve assessment of fishing vessel safety, this chapter explores current knowledge on vessel stability, inertial measurement units (IMUs) and cost-effective single-board computers (SBCs). Section 2.1 discusses vessel motion and stability, what causes vessels to capsize, and how the stability of vessels is assessed. Section 2.2 examines different tools for measuring vessel motion and assessing stability. This section also discusses SBCs coupled with IMUs as cost-effective methods of improving the assessment of fishing vessel stability. Section 2.3 demonstrates how the roll period can be determined from a time series and Section 2.4 presents an initial exploration of how time series measurements using cost-effective technologies perform when used to compute period of motion. Section 2.5 summarizes the chapter.

2.1 Vessel stability

Vessel motion at sea is a nonlinear phenomenon due to interactions between hydrodynamic forces and vessel dynamics. The combined actions of forces and moments, due to wind and waves, on a vessel as well as the inertia of the vessel itself determine the vessel's motion in six degrees of freedom (DOF). A vessel's motion has three translational components, surge, sway, and heave, and three rotational components, roll, pitch, and yaw.

As shown in Figure 2.1, surge is the longitudinal (forward and back) motion of the vessel, sway is the lateral (side to side) motion of the vessel, and heave is the vertical (up and down) motion of the vessel. Roll is the rotation about the longitudinal axis, pitch is the rotation about the lateral axis, and yaw is the rotation about the vertical axis. The most safety critical components of motion are those in the vertical plane (heave, pitch and roll), with roll being the most critical motion leading to ship capsize (Ibrahim and Grace, 2010).

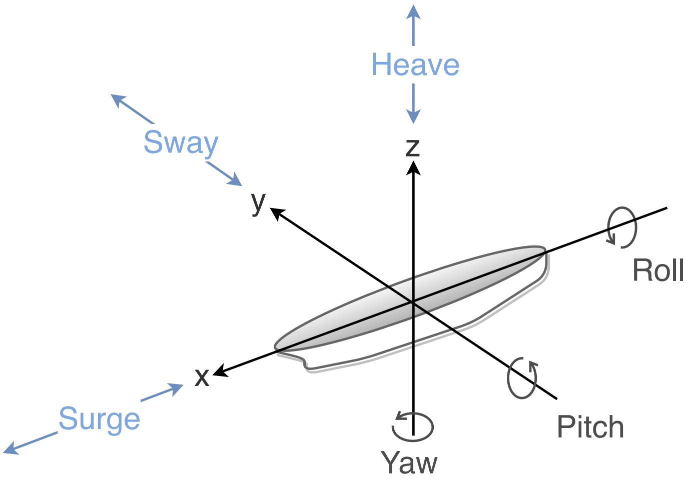

Figure 2.1: Vessel degrees of freedom consisting of three translational components (surge, sway, heave) and three rotational components (pitch, roll, yaw)

2.1.1 Stability theory

A vessel is in stable equilibrium if it tends to return to its initial position after being inclined and in unstable equilibrium if, when inclined to a small angle, it heels over even further (Barrass and Derrett, 2006). In other words, a stable fishing vessel is one which can return to its upright position after being heeled over by any combination of waves, wind, or forces from fishing operations (Womack and Johnson, 2004). Stability can be classified as either static or dynamic. Static stability is measured when there are no external forces acting on a vessel such as wind or waves, and is expressed in terms of the metacentric height (GM) or righting lever (GZ) with the unit of measurement in metres. Dynamic stability is measured when there are external forces acting on a vessel and is expressed in terms of the area under the GZ curve (Gudmundsson, 2009). The dynamic stability of a vessel at different angles of heel cannot be the same, and its unit of measurement is tonne-metre-radian. Sufficient static stability does not guarantee a vessel's stability during operation (Yaakob et al., 2015). This is because static stability is measured under the assumption that there are no external forces on the vessel.

A vessel's classification of stability as either stable or unstable is dependent on moments acting to return the vessel to its upright position, and moments acting to capsize the vessel. A vessel becomes unstable when the capsizing moment exceeds the righting moment. These moments, which determine stability, are related to gravity, buoyancy, and the vessel's metacentres (Barrass and Derrett, 2006). Moments acting on a vessel can be better understood by examining the two forces that interact to determine stability: gravity and buoyancy. Gravity acts downwards at a vessel's centre of gravity (G), which is determined by the distribution of mass such as fuel and fishing equipment on a vessel. Buoyancy acts upwards at a vessel's centre of buoyancy (B), which is the geometrical centre of the immersed part of the vessel. The interaction between gravity and buoyancy can result in either a righting or capsizing force on a vessel as illustrated in Figure 2.2.

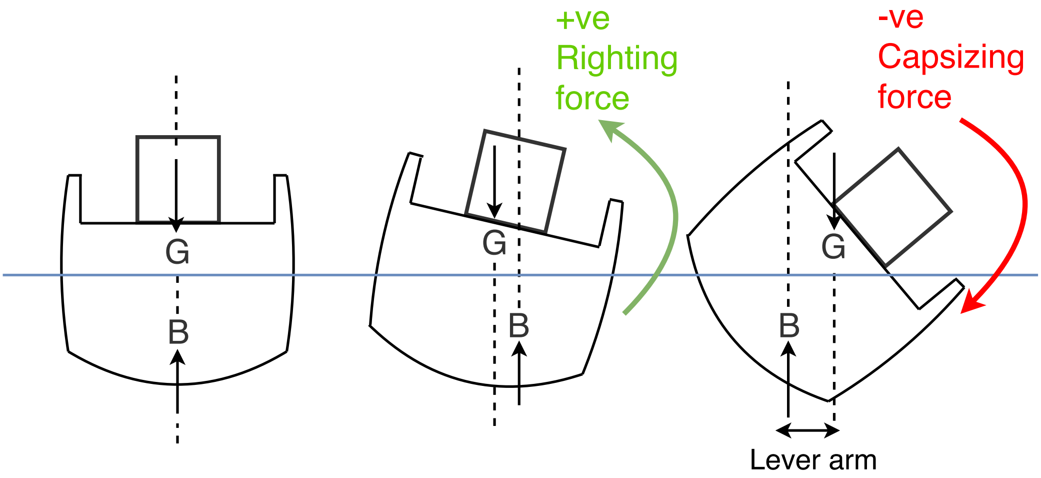

FIGURE 2.2: Forces creating moments on a vessel: gravity and buoyancy.
Adapted from *A guide to fishing vessel safety,* by Maritime New Zealand (2011)

Figure 2.2 shows that with mass evenly distributed and no external forces on a vessel, the centre of gravity and the centre of buoyancy are aligned vertically. When a vessel heels due to an external force such as wind or waves, the centre of buoyancy moves further outboard than the centre of gravity, resulting in a righting force (positive stability). The righting lever is the horizontal distance between the centre of gravity and the centre of buoyancy. When a vessel heels too far, the centre of gravity moves further outboard than the centre of buoyancy resulting in a capsizing force (negative stability).

To use a vessel's metacentric height or righting lever to calculate its stability, the location of its metacentre (M) must be determined. The metacentre is the point of intersection of two vertical axes through the centre of buoyancy at different angles of heel. The transverse metacentre (Figure 2.3a) is considered when a vessel is heeling or listing (transverse inclinations) while the longitudinal metacentre (Figure 2.3b) is considered when a vessel is trimming (longitudinal inclination). From the viewpoint of rotational moment, 'the metacentre of a ship is an example of a dynamically equivalent application point of a resultant force, i.e. the hydrostatic or buoyancy force' (Herder and Schwab, 2004). The rotational moment is zero at the point of application of this resultant force. Even though there are multiple definitions of the metacentre, these have been shown to refer to the same unique point on a vessel for any angle of heel (Mégel and Kliava, 2010).

The height of the metacentre above the centre of buoyancy (BM) is equal to the ratio of the vessel's moment of inertia (I) to its submerged volume (V) (Bouguer, 1746; Nowacki and Ferreiro, 2011). The height of the metacentre above a vessel's keel (KM) can be calculated as the sum of the height of the centre of buoyancy above the keel (KB) and the height of the metacentre above

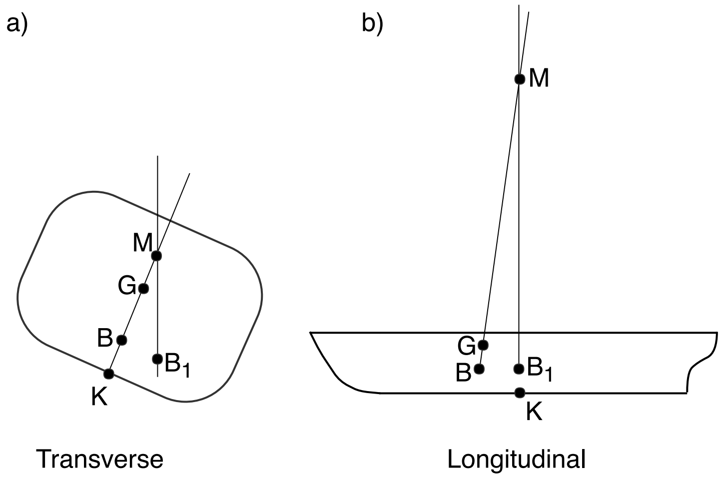

FIGURE 2.3: Transverse and longitudinal metacentres for a vessel inclined by a small angle, resulting in the shift in the centre of buoyancy from B to B_1. Adapted from *Ship Stability: Notes and Examples,* by Young and Barrass (2001)

the centre of buoyancy using Equation 2.1 (Molland, 2008). Using the height of the metacentre above the keel, the metacentric height can be calculated using Equation 2.2 (Patterson and Ridley, 2014).

$$KM = KB + BM \qquad BM = \frac{I}{V} \tag{2.1}$$

$$GM = KM - KG = KB + BM - KG \tag{2.2}$$

The relative position of the metacentre to the centre of gravity determines whether the lever arm is a righting or capsizing lever. When a vessel's metacentre is above the centre of gravity resulting in a positive metacentric height, a vessel experiences a righting force. On the other hand, when a vessel's metacentre is below its centre of gravity resulting in a negative metacentric height, a vessel experiences a capsizing force as shown in Figure 2.4.

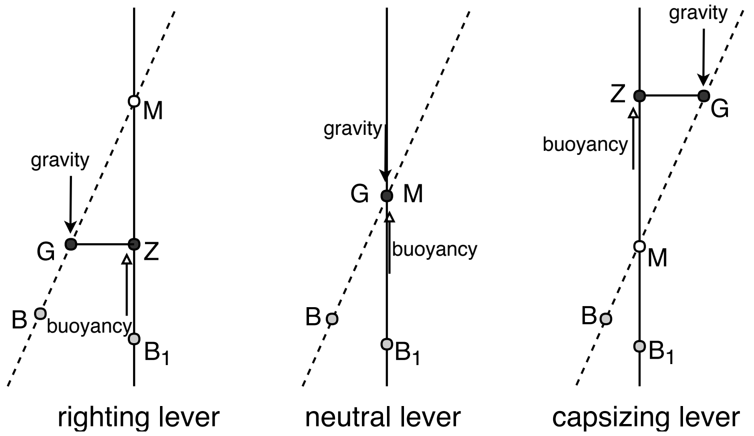

FIGURE 2.4: Types of righting forces/levers depending on whether the centre of gravity is above or below the metacentre. Adapted from *Physical Models for Simulating Ship Stability and Hydrostatic Motion,* Journal of Marine Science and Technology by Ueng (2013)

In terms of stability, the lower a vessel's centre of gravity and the higher its metacentre, the more stable the vessel. An extremely high centre of gravity results in a low metacentric height. This reduces the righting lever leading to an increase in the force required to return a vessel to its upright position and makes the vessel unstable.

At small angles of heel (ϕ), less than 3° (Tupper, 1996), there is a linear relationship between the metacentric height and the righting lever as the metacentre is considered to be a fixed point. From Figure 2.4, it can be observed that the metacentric height and righting lever are related through Equation 2.3. At small angles, $\sin\phi$ is approximately equal to ϕ. At larger angles, the metacentre is not considered a fixed point and methods such as the wall-sided formula, Attwood's formula, and Moseley's formula are used to calculate a vessel's static and dynamic stability (Young and Barrass, 2001) as shown in Figure 2.5.

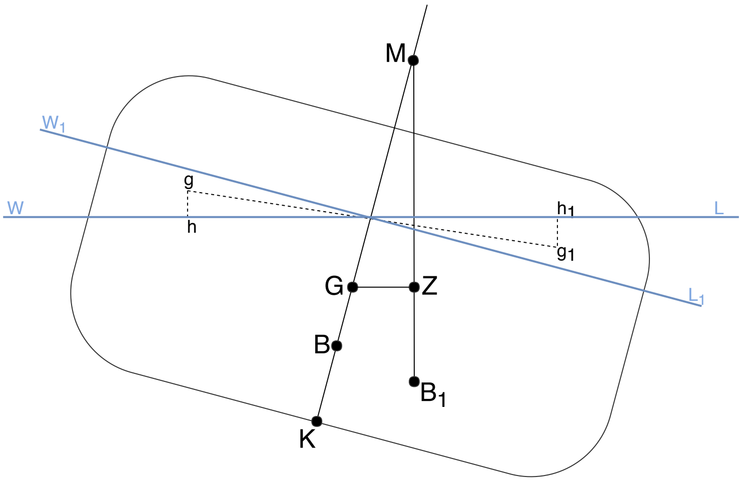

FIGURE 2.5: Calculating the righting lever at large angles.
Adapted from *Ship Stability: Notes and Examples,* by Young and Barrass (2001)

At small angles of heel:

$$GZ = GM \sin\phi \approx GM\phi \tag{2.3}$$

Using wall-sided formula:

$$GZ = \left(GM + \frac{1}{2}BM\tan^2\phi\right)\sin\phi \tag{2.4}$$

Using Attwood's formula:

$$GZ = \frac{v \times hh_1}{V} - BG\sin\phi \tag{2.5}$$

Using Moseley's formula:

$$GZ = \left(\frac{v \times (gh + g_1h_1)}{V} + BG(\cos\phi - 1)\right) \tag{2.6}$$

In Equation 2.5, v is the volume of either of the above sides, hh_1 is the horizontal distance between the centres of the immersed and emersed side, V is the volume of displacement of the vessel, and BG is the vertical distance between B and G. In Equation, 2.6 $(gh + g_1h_1)$ is the vertical distance between the centres of gravity of the immersed edge and the emersed edge.

The righting moment (RM) of a vessel at an angle of heel can be expressed as the product of the righting lever at that angle and the weight (W) of the vessel (Equation 2.7).

$$RM = GZ \times W \tag{2.7}$$

A vessel's GZ curve, also known as a static stability curve, is used to assess a vessel's static stability. Among a number of factors that should be considered when modelling vessel capsize, the GZ curve is the only factor that is key to modelling all capsize scenarios (ITTC Specialist Committee on Stability, 1999). Some of these scenarios are presented in Section 2.1.2. It is important to note that each GZ curve is for a specific loading condition. This is because once a vessel's loading condition changes, for example, due to a reduction in fuel, loading of fish on board, or shifting of weights, this curve is an invalid means of assessing the vessels static stability. Figure 2.6 shows an example of a GZ curve with relevant information numbered and explained.

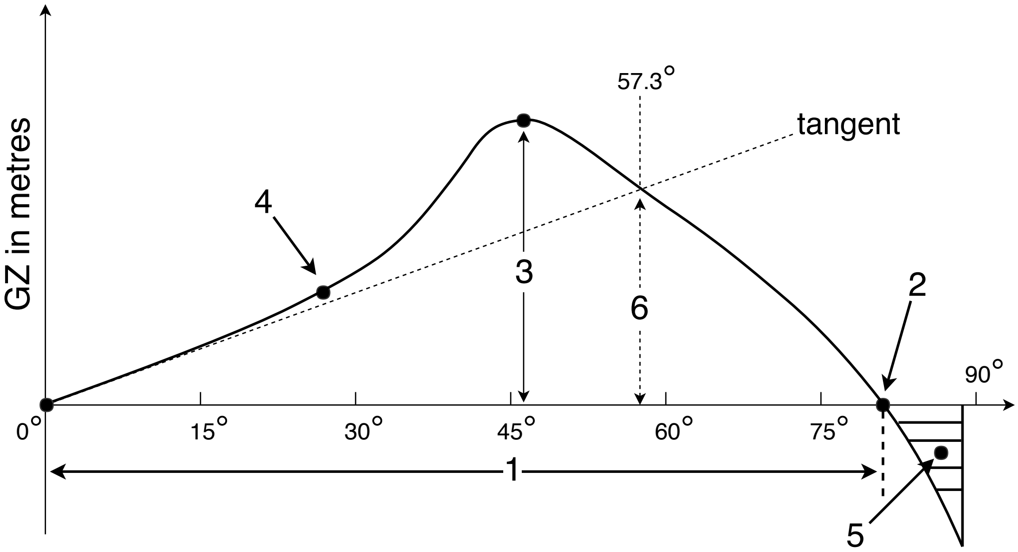

FIGURE 2.6: Example of a static stability curve (GZ curve).
Adapted from *Ship Stability: Notes and Examples,* by Young and Barrass (2001)

In Figure 2.6:

1. Shows the range of stability, when the vessel experiences a righting force, and includes all positive GZ values. Once the GZ is negative, the vessel experiences a capsizing force.
2. Indicates the angle beyond which the vessel capsizes as GZ values become negative.
3. Specifies the maximum GZ.

4. Highlights when the vessel's deck edge immerses. It is known as the point of inflection / contraflecture. At this point, the concavity of the curve changes.
5. Shows negative stability.
6. Indicates the approximate GM, a measure of static stability. It is obtained from the intersection of a tangent to the curve at the origin and a vertical line at 57.3 deg (1 radian).

In Figure 2.6, the area under the curve is 'proportional to the energy needed to heel it to that angle' (Molland, 2008). This area indicates the amount of energy a vessel can absorb from wind and waves without heeling excessively. As shown in Figure 2.6, a vessel can have the same static stability, measured in GZ, at different angles of heel. The dynamic stability at a given angle of heel is measured as the product of the weight of the vessel (W), and the area under the GZ curve up to that angle (Equation 2.8).

$$\text{Dynamic stability} = \text{Area under } GZ \text{ curve} \times W \tag{2.8}$$

Even if a vessel has a high maximum GZ value, it can still capsize easily if there is an insufficient area under the GZ curve. The loading condition of fishing vessels, for which GZ curves are calculated, changes with every voyage as weights change and are shifted on board. In order to easily obtain GZ values for varying loading conditions, cross curves of stability are used for finding GZ values where the location of the centre of gravity is known. Cross curves of stability use the righting lever measured from the keel (KN), and the vertical height of the centre of gravity above the keel (KG) to calculate GZ as shown in Figure 2.7.

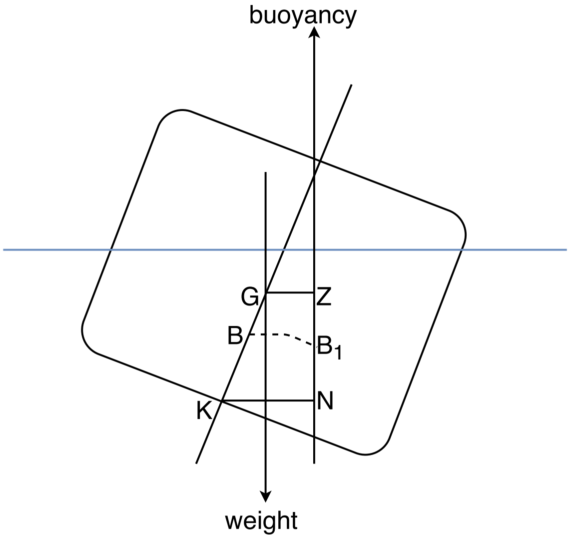

FIGURE 2.7: KN for a ship at any angle of heel
Adapted from *Ship Stability - Understanding Curves of Static Stability,* by Chakraborty (2017a)

From Figure 2.7, the equation for calculating GZ using KN curves is derived as

$$GZ = KN - KG\sin\phi \tag{2.9}$$

KN values in tabulated form can be used instead of curves. Figure 2.8 shows an example of a derived KN curve. KN curves provide stability information for a range of displacements and angles of heel, and remain accurate if a vessel's hull form does not change.

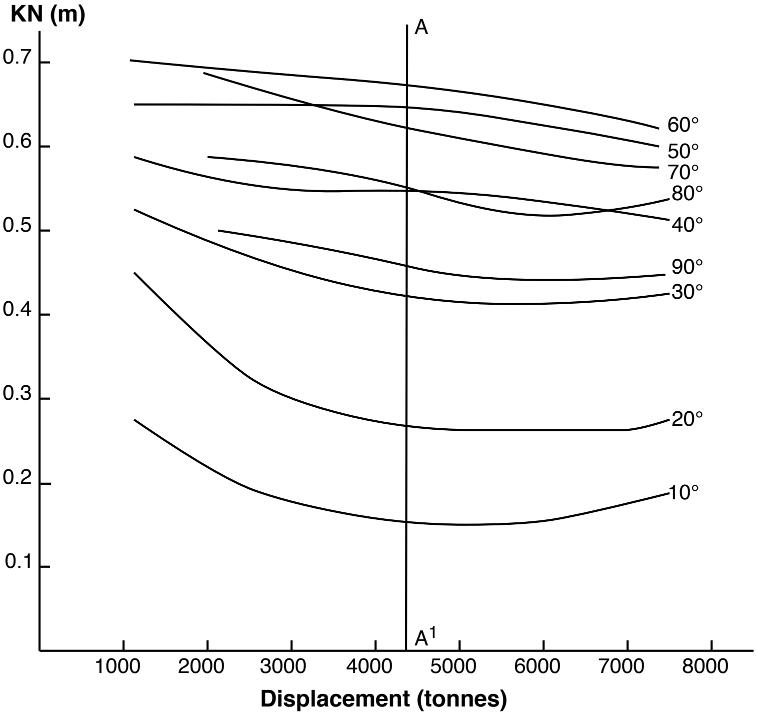

FIGURE 2.8: Cross curves of stability for a vessel
Adapted from *Ship Stability - Understanding Curves of Static Stability,* by Chakraborty (2017a)

There is a relationship between a vessel's roll period (T) and its metacentric height. Comstock (1967) presents a variation of the link between metacentric height in metres and roll period in seconds in Equation 2.10, in which g is the gravitational acceleration in metres per second squared, and k is the radius of gyration in metres. The radius of gyration is defined as the perpendicular distance from an axis of rotation at which the mass of a body may be assumed to be concentrated and at which the moment of inertia of a point mass is equal to the moment of inertia of the actual mass about the axis.

$$T = \frac{2\pi k}{\sqrt{g\overline{GM}}} \tag{2.10}$$

Equation 2.10 is obtained by considering the general equation of roll motion with no coupling from other degrees of freedom (Wawrzynski and Krata, 2016) to be

$$I\ddot{\phi} + B_e\dot{\phi} + K(\phi) = M_\omega \cos(\omega_e t) \tag{2.11}$$

where:

I, is the total moment of inertia (including the moment of added mass),

ϕ, is the roll angle,

B_e, is the roll damping coefficient,

$K(\phi)$, is the righting moment,

M_ω, is the external heeling moment exciting rolling, and

ω_e, is the encounter frequency of waves.

In Equation 2.11, there is added mass moment because as a vessel accelerates and decelerates in water, surrounding water moves with the vessel hull (Sen and Vinh, 2016). The mass moment of inertia and the righting moment at small angles can be substituted using Equation 2.12 and Equation 2.13.

$$I = mk^2 \qquad m = \frac{W}{g} \qquad I = \frac{W}{g}k^2 \tag{2.12}$$

$$K(\phi) = GZ \times W \qquad GZ = \overline{GM}\sin\phi \approx \overline{GM}\phi \qquad K(\phi) = \overline{GM}\phi W \tag{2.13}$$

Substituting the moment of inertia and the righting moment into Equation 2.11 gives

$$\begin{aligned} \frac{Wk^2}{g}\ddot{\phi} + B_e\dot{\phi} + \overline{GM}W\phi = M_\omega \cos(\omega_e t) \\ \ddot{\phi} + \frac{gB_e}{Wk^2}\dot{\phi} + \frac{g\overline{GM}}{k^2}\phi = \frac{gM_\omega \cos(\omega_e t)}{Wk^2} \end{aligned} \tag{2.14}$$

From Equation 2.14 we can deduce the natural frequency and roll period from the coefficient of ϕ as

$$\begin{aligned} \omega_n^2 &= \frac{g\overline{GM}}{k^2} \\ \left(\frac{2\pi}{T}\right)^2 &= \frac{g\overline{GM}}{k^2} \\ T &= \frac{2\pi k}{\sqrt{g\overline{GM}}} \end{aligned} \tag{2.15}$$

The International Maritime Organization (2009) presents the relationship between the roll period and the metacentric height in terms of a vessel's beam (B), length (L), and draft (D) as

$$T = \frac{2cB}{\sqrt{\overline{GM}}} \qquad c = 0.373 + 0.023\frac{B}{D} - 0.043\frac{L}{100} \tag{2.16}$$

There is a simpler variation of the Equation relating T to GM using only a vessel's beam (B) (Noel, 1989; Maul, 2017). In Equation 2.17, the metacentric height is measured in feet and roll period in seconds.

$$T = \frac{0.44B}{\sqrt{\overline{GM}}} \tag{2.17}$$

Equation 2.10, Equation 6.1 and Equation 2.17 show an inverse relationship between a vessel's roll period and the square root of its metacentric height and vessel draft, and a proportional relationship between the roll period and the radius of gyration, length and beam. The inverse relationship between the roll period and metacentric height have led to studies on how roll motion data is used to estimate vessel stability (Garcia et al., 2001; Terada et al., 2016).

The roll period and metacentric height are indicative of the stiffness of a vessel. The lower the metacentric height, the higher the roll period, and the longer it will take the vessel to return to an upright position. Vessels with a high roll period are classified as tender. Even though tender vessels are more comfortable for personnel on board, vessels with the metacentric height too low are unstable and have a high risk of overturning (Paroka and Umeda, 2017). On the contrary, the higher the metacentric height, the lower the roll period, and the quicker the vessel returns to its upright position. These vessels tend to assume the slope of passing waves. Such vessels are classified as stiff and require less force to return it to an upright position. Even though stiff vessels are more stable than tender vessels, vessels with rolling periods too low are uncomfortable for people on board and result in motion sickness.

2.1.2 Modes of capsize

The situations leading to vessel capsize can be grouped into four main categories; static loss of stability, dynamic loss of stability, broaching and combined modes with additional factors (ITTC Specialist Committee on Stability, 1999).

Static loss of stability occurs when there is either a large prolonged reduction in the righting lever in the crest of a wave with critical length and steepness, or negative metacentric height. Experimental evidence (Oakley et al., 1974) has shown that this mode of capsize usually occurs at low encounter frequencies in following to stern quartering waves (Kat and Paulling, 2001).

A vessel loses stability dynamically with extreme roll motions and lack of righting energy under a variety of conditions including dynamic rolling with coupled degrees of freedom, parametric excitation, resonant excitation, and impact excitation (Hosseini, 2009). Dynamic rolling is defined by asymmetric rolling in stern quartering seas. During dynamic rolling, due to the vessel surging, the vessel spends more time in the wave crest than trough leading to a periodic increase and decrease of the righting lever (Umeda et al., 1995). In this case, the roll motion increases steadily over a number of wave encounters and may be significantly larger than the vessel's natural roll period. Parametric excitation, also known as low cycle resonance, occurs due to the repeated passage of a wave in either head or following seas causing recurring changes in the righting lever (Dallinga et al., 1997). These changes cause large roll motions when the natural roll period of the vessel is approximately twice the wave encounter frequency, and the wavelength is between 0.8 and 2 times the ship length (Levadou and Gaillarde, 2003). Resonant excitation occurs when a vessel oscillates close to its natural roll frequency. It is affected by a number of factors including vessel speed, wavelength, wave height, heading angle, and vessel weight distribution. Impact excitation is caused by a breaking wave hitting the side of a vessel, affecting vessel dynamics and causing extreme roll motions. It is particularly relevant to small vessels operating in steep breaking seas.

Broaching occurs when there is a ‘wave-induced undesired, large amplitude change in heading angle’ (ITTC Specialist Committee on Stability, 1999). Capsize due to broaching occurs in three modes. The first mode occurs in situations where a vessel is gradually forced to beam sea in successive steep overtaking waves at low speed. The second mode occurs at a higher speed with low frequency, large amplitude yaw motions. The third mode occurs when a vessel surf-rides a single wave resulting in a steadily increasing yaw angle (Beck and Reed, 2000).

Additional factors leading to vessel capsize include shifting cargo, water on vessel deck, deck edge submergence and extreme wind loads in beam seas. Shifting cargo on a vessel changes the location of the centre of gravity, causing a change in stability. For small fishing vessel, water on the deck is critical to stability because of their small freeboards. As vessels decrease in size, the ratio of the volume of water trapped on deck to vessel displacement increases (Paroka and Umeda, 2017).

2.1.3 General methods of assessing stability

There are a number of ways of assessing vessel stability using factors such as GM, GZ, vessel length, breadth, freeboard, centre of gravity, fuel, and distribution of weights. Methods of assessing stability include the full stability method, the approximate minimum GM formula, the heel test, and the roll period approximation (Maritime and Coastguard Agency, 2010).

2.1.3.1 Full stability method

The full stability method is mandatory for all vessels over 45 metres in overall length (International Maritime Organization, 2009) and involves an inclining experiment conducted for all newly built vessels and after any structural changes to vessels. The experiment determines the lightship weight, centre of gravity, and stability for different loading conditions (GM).

The inclining experiment involves shifting known weights transversely on board a vessel and measuring the inclination using pendulums placed along the longitudinal centre line of the vessel as the centre of gravity changes from G to G_1 as shown in Figure 2.9.

From the inclining experiment, a number of method’s can be used to calculate the vertical centre of gravity and the metacentric height (Karolius and Vassalos, 2018b). The classical method for calculating the metacentric height assumes that as the vessel is inclined for small angles during the experiment, the location of the metacentre is constant. From the inclining experiment, the metacentric height is calculated using the following Equation:

$$GM = \frac{w \times d}{W \tan\theta} \tag{2.18}$$

where:

w, is a known weight,

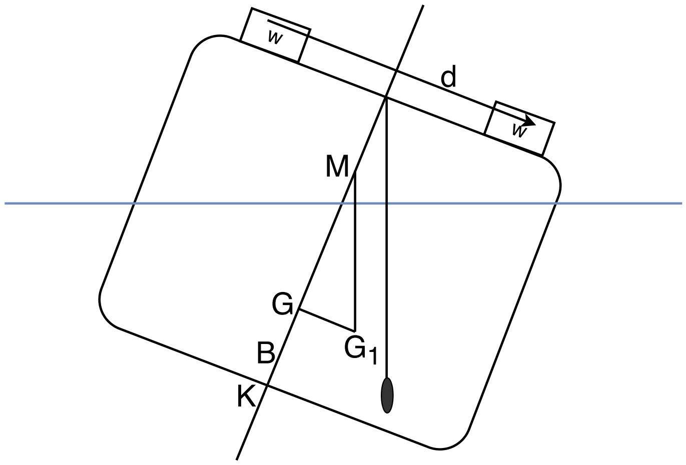

FIGURE 2.9: Inclining experiment for a vessel with a known weight (w) shifted by a distance (d). Adapted from *Ship Stability: Intact Stability Criteria and Inclining Experiment,* by Chakraborty (2017b)

d, is the distance the known weight is shifted, and

W, is the mass displacement of the ship.

There are uncertainties associated with the inclining experiment (Woodward et al., 2016). These are reduced by considering issues including the following:

- Avoid experimenting in beam winds;
- Ensure the vessel is not restrained floating at zero heel angle when upright;
- All loose items on-board are either removed from the vessel or restrained so that there are no unwanted weight shifts during the experiment;
- The free surface effect is made minimal by having tanks either at full capacity or empty;
- Record the temperature, density and salinity of the water during the experiment to calculate the mass displacement of the vessel.

The GZ curve obtained using the calculated metacentric height from an inclining experiment should satisfy the following criteria (Maritime and Coastguard Agency, 2010):

- the area under the curve of righting levers (GZ curve) shall not be less than:
  - 0.055 metre-radians up to an angle of 30°;
  - 0.090 metre-radians up to an angle of 40° ;
  - 0.030 metre-radians between the angles of heel of 30° and 40°;
- the righting lever shall be at least 200 millimetres at an angle of heel equal to or greater than 30°;
- the maximum righting lever shall occur at an angle of heel not less than 25°;

- in the upright position the transverse metacentric height shall not be less than 350 millimetres;

2.1.3.2 Approximate minimum GM formula

The approximate GM formula is used in situations in which GZ curves and cross-curves of stability are unavailable. The GM obtained from an inclining experiment is compared with a minimum GM for all operating conditions calculated as:

$$GM_{min} = 0.53 + 2B\left[0.075 - 0.37\left(\frac{f}{B}\right) + 0.82\left(\frac{f}{B}\right)^2 - 0.014\left(\frac{B}{D}\right) - 0.032\left(\frac{l_s}{Lwl}\right)\right] \tag{2.19}$$

where:

B, is the maximum beam of the vessel,
D, is the depth in the middle of the vessel,
f, is the minimum freeboard (the perpendicular distance from the deck to the waterline),
l_s, is the actual length of the vessel, and
Lwl, is the length of the vessel on the waterline in maximum load condition.

The vessel is stable if the GM calculated from the inclining experiment is greater than the calculated $\mathrm{GM}_{\mathrm{min}}$.

2.1.3.3 Heel test

There are two variations of the heel test; the offset load test and the small commercial vessel code standard. An offset load test requires a weight 25 times vessel length (L) times vessel beam (B) in kg to be arranged along one side of the vessel. The angle of heel should be less than 15° and the freeboard more than 75 mm for the stability to be assessed as sufficient. The small commercial vessel code standard requires the heel resulting from applying the maximum load at the main deck at the maximum outboard position to be less than 7° and there to be sufficient freeboard. This method of assessing stability is applicable to only vessels carrying up to 1 tonne of cargo.

2.1.3.4 Roll period approximation

The approximate roll method is a simple method of estimating stability quickly (Young and Barrass, 2001) and is deemed as a suitable test for vessels up to 70 metres in length. The approximate roll method requires the vessel to be induced to roll under the following conditions;

- The vessel should be loaded as it is before operation with all equipment and supplies placed where they are usually stored.

Table 2.1: Maximum roll period in seconds for vessels with beams less than 4.4 m. Adapted from *Safety Recommendations for Decked Fishing Vessels of Less than 12 metres in Length and Undecked Fishing Vessels,* by International Maritime Organization (IMO) et al. (2012)

Depth (m)	**Beam (m)**														
	1.6	1.8	2.0	2.2	2.4	2.6	2.8	3.0	3.2	3.4	3.6	3.8	4.0	4.2	4.4
0.6	3.2	3.2	3.4												
0.7	3.8	3.5	3.5	3.5											
0.8	4.3	4.0	3.7	3.6	3.6	3.7									
0.9	4.3	4.6	4.3	3.9	3.7	3.7	3.8								
1.0		4.6	4.9	4.5	4.2	4.0	3.8	3.9	4.0						
1.1			4.8	5.1	4.6	4.4	4.2	4.0	4.0	4.1	4.3				
1.2				5.0	5.2	4.8	4.5	4.3	4.2	4.1	4.2	4.3	4.4		
1.3					5.1	5.3	5.0	4.7	4.5	4.4	4.2	4.3	4.4		
1.4						5.3	5.5	5.1	4.9	4.7	4.5	4.4	4.4	4.5	4.6
1.5							5.4	5.6	5.3	5.1	4.9	4.7	4.6	4.5	4.6
1.6								5.5	5.7	5.4	5.2	4.9	4.9	4.8	4.7
1.7									5.7	5.9	5.6	5.2	5.2	5.1	5.0
1.8										5.8	6.0	5.5	5.5	5.4	5.2

- The vessel must not touch the dock or the bottom and there must be sufficient space around the vessel, with a recommended minimum distance of 0.6m to both.
- If possible, there should be no mooring lines attached to the vessel during the test, and if there are these lines should be slack during the test.
- The test should be conducted in as calm an environment as possible to eliminate the influence of external factors such as wind, waves, and current on the vessel's roll.
- The vessel should not roll too much. The limit of roll should be monitored by placing a temporary mark amidship on the vessel's hull. The distance of the mark above the waterline is obtained by dividing the vessel's beam by eight.

The time for five complete rolls is then measured. This is repeated three times, and the average time for one roll is calculated. From this result, the vessel is classified as tender and unstable if its beam in metres is less than the time for one roll in seconds. In this situation the vessel returns to its upright position slowly. Alternatively, the vessel returns to its upright position very quickly. In this case, the vessel is classified as stiff and stable and its beam in metres is greater than the time for one roll in metres (Maritime and Coastguard Agency, 2014).

For vessels with beams less than 4.4 metres and depths less than 1.8 metres, another way of using the roll period test is by comparing the roll period obtained from the roll period test with the values in Table 2.1. The vessel has sufficient stability if the obtained roll period is less than the roll period indicated in the table.

2.1.3.5 Approximate minimum GM formula combined with roll period test

Another method of assessing stability uses a combination of the approximate minimum metacentric height and the roll period test. In this method, a roll period test is conducted and the obtained roll period is used to calculate the GM with the formula:

$$GM = \left(\frac{0.834B}{T}\right)^2 \tag{2.20}$$

where:

B, is the beam of the vessel in metres, and
T, is the roll period in seconds.

Equation 2.21 and Equation 2.22 are then used to calculate the minimum required metacentric height for all operating conditions. Equation 2.21 is used for vessels considered suitable to operate in seas with significant wave heights above 2 m and wind speeds in excess of Beaufort Force 6 (12 m/s) and Equation 2.22 is used for vessels suitable to operate in conditions with significant wave heights less than 2 m and wind speeds below Beaufort Force 6 (12 m/s).

$$GM_{min} = 0.117B\left(\frac{B}{D} - 2.2\right) + B\left[1.773\left(\frac{T}{D}\right)^2 - 2.646\left(\frac{T}{D}\right) + 1.016\right] \tag{2.21}$$

$$GM_{min} = 0.059B\left(\frac{B}{D} - 2.2\right) + B\left[2.085\left(\frac{T}{D}\right)^2 - 2.857\left(\frac{T}{D}\right) + 0.990\right] \tag{2.22}$$

where

B, is the maximum beam of the vessel in metres,
D, is the depth in the middle of the vessel in metres, and
T, is the roll period in seconds.

The vessel has satisfactory stability if GM is greater than $\mathrm{GM}_{\mathrm{min}}$. All the methods for assessing stability presented so far in this section, including the full stability method, the approximate minimum GM formulae, the heel test, and the roll period approximation, are static stability tests involving the estimation of either the metacentric height or the roll period. They do not assess whether a vessel has sufficient dynamic stability and how the dynamic stability changes in different operating conditions.

2.1.4 Safety assessment methods developed for fishermen

An effort to produce a method for assessing safety during a vessel's operation at sea led to the development of the methods discussed in this section.

Wolfson method

The Wolfson method was developed by the Wolfson Unit for Marine Technology and Industrial Aerodynamics (WUMTIA) at the University of Southampton. This method recommends the display of a stability notice on vessels to provide guidance on how operating conditions, including sea state and loading, reduce vessel safety. The Wolfson method assesses safety using a 'traffic light system' with three defined safety zones;

- green indicates 'safe' except when operating in extreme sea states,
- amber indicates 'a low level of safety', suggesting the vessel operates in only low sea states, and
- red indicates 'unsafe and danger of capsizing' suggesting the vessel operates with extreme caution.

The safety zones are defined in terms of the maximum sea state, the minimum freeboard, and the lifting and loading conditions (Maritime and Coastguard Agency, 2010). In terms of the sea state, the boundaries between the safety zones are defined by the significant wave height (Hs) calculated using the length (L)of a vessel as follows:

$$\begin{aligned} &\text{Green/amber boundary}: \quad Hs_{\text{amber}} = \sqrt{1+0.4L}-1 \\ &\text{Amber/red boundary}: \quad Hs_{\text{red}} = \frac{Hs_{\text{amber}}}{2} \end{aligned} \tag{2.23}$$

Using the calculated significant wave height boundaries, Hs_{amber} and Hs_{red}, the safety zone boundaries in terms of the minimum freeboard are defined using the vessel's beam and length as:

$$\begin{aligned} &\text{Green/amber boundary}: \quad \text{Minimum freeboard}_{\text{amber}} = \frac{B}{L}\left(Hs_{\text{amber}}\right) \\ &\text{Amber/red boundary}: \quad \text{Minimum freeboard}_{\text{red}} = \frac{B}{L}\left(Hs_{\text{red}}\right) \end{aligned} \tag{2.24}$$

The Wolfson Guidance suggests a stability guidance/notice contains the following information:

- the significant wave height of the maximum recommended sea state for the safety zones,
- the range of minimum residual freeboards appropriate for each zone,
- for loading cases, definitions of the critical loadings that are identifiable on board,

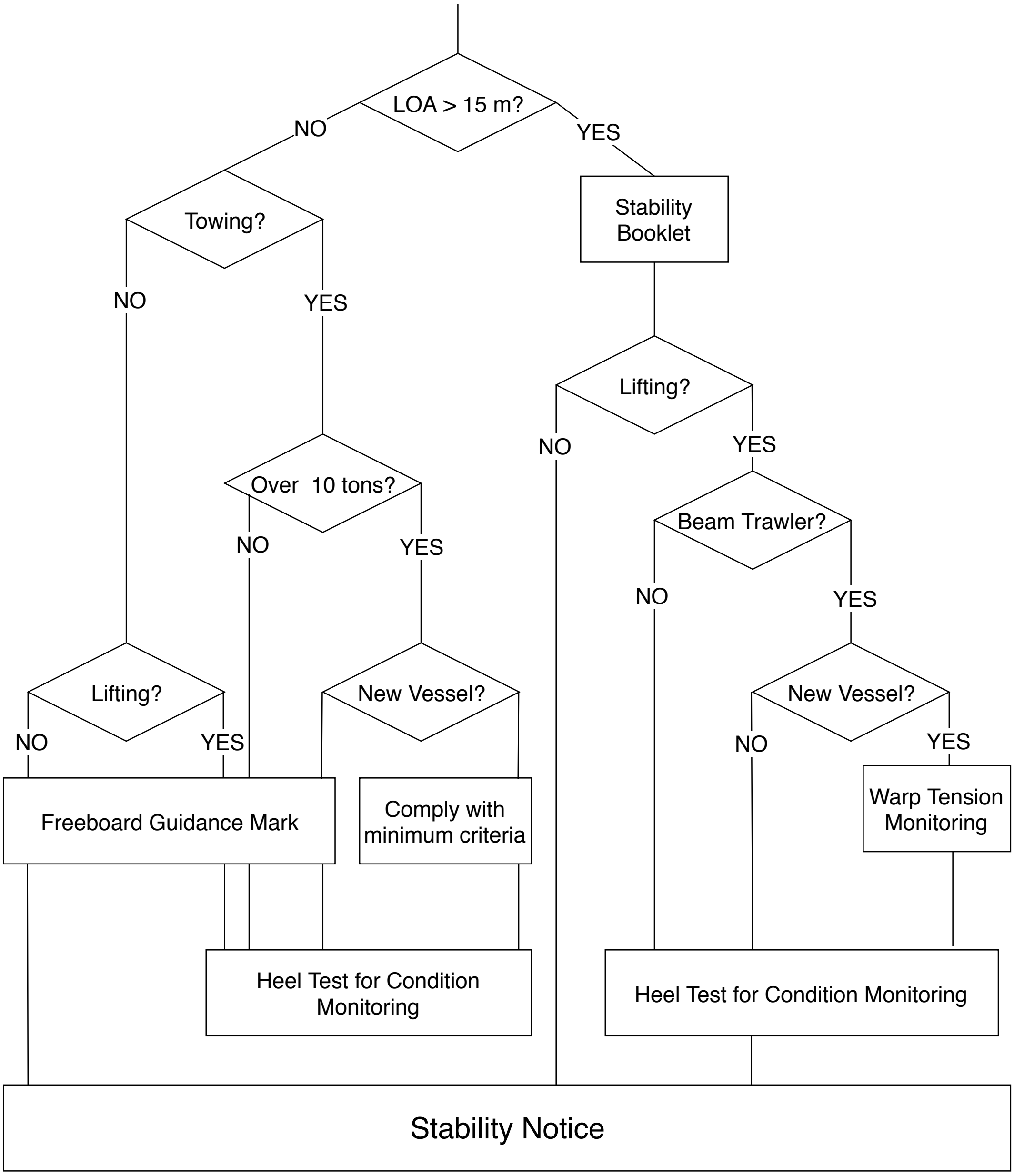

FIGURE 2.10: Flowchart of system of assessment and guidance for fishing vessels using the Wolfson method.
Adapted from *Research Project 560: Simplified Presentation of FV Stability Information for Vessels 12* m *Registered Length and Over,* by Wolfson Unit (2006)

- for lifting cases, the range of heel angles appropriate to each zone, and, or
- where a load cell is fitted, the range of lifting loads appropriate to each zone.

Figure 2.10 shows how the stability notice is obtained for vessels of different types and lengths.

Figure 2.11 shows an example of a stability notice incorporating information from a heel test. Figure 2.12 shows an example of a stability notice with the recommended significant wave heights and freeboard calculated using Equation 2.23 and Equation 2.24.

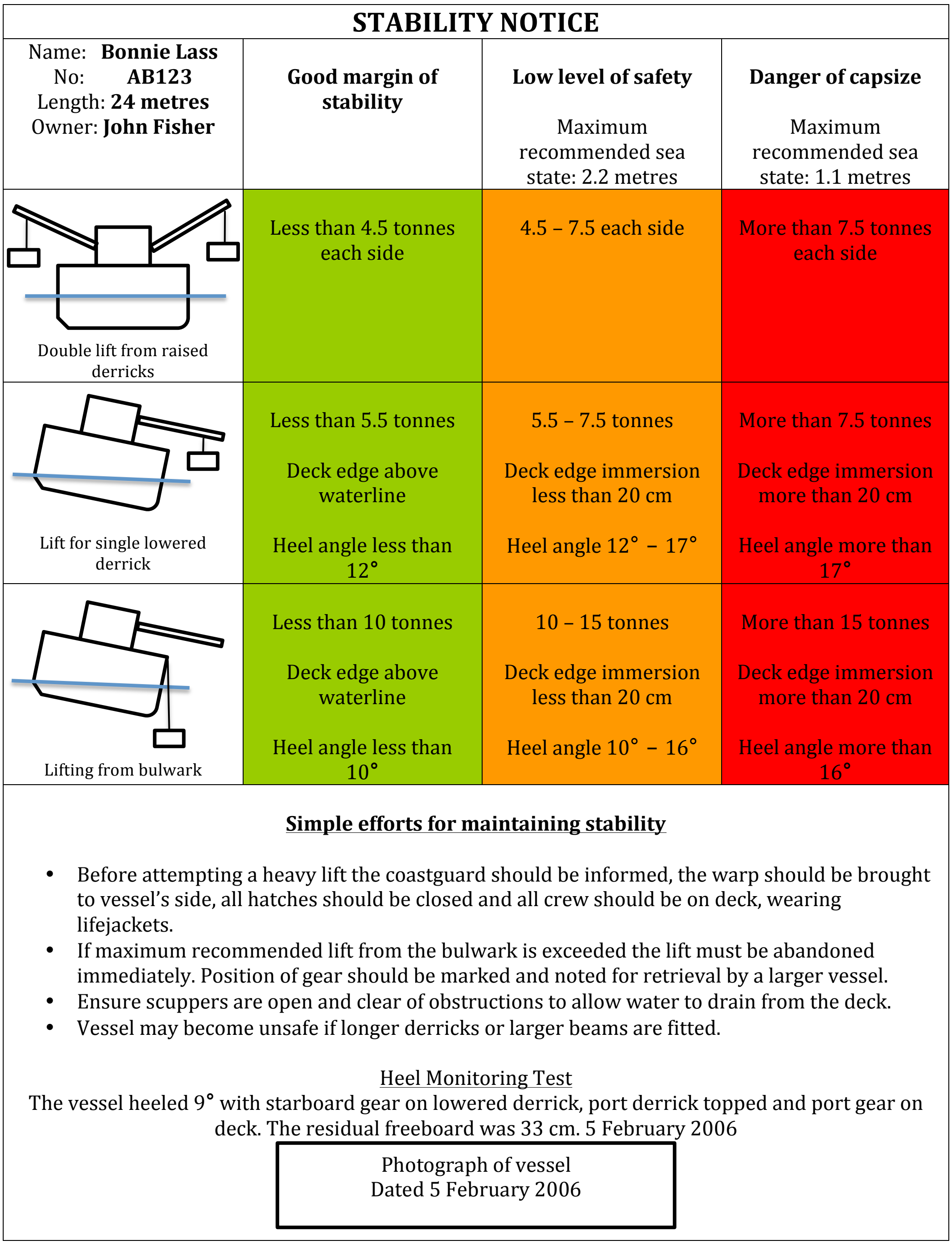

STABILITY NOTICE

Name: **Bonnie Lass** No: **AB123** Length: **24 metres** Owner: **John Fisher**	**Good margin of stability**	**Low level of safety** Maximum recommended sea state: 2.2 metres	**Danger of capsize** Maximum recommended sea state: 1.1 metres
Double lift from raised derricks	Less than 4.5 tonnes each side	4.5 – 7.5 each side	More than 7.5 tonnes each side
Lift for single lowered derrick	Less than 5.5 tonnes Deck edge above waterline Heel angle less than 12°	5.5 – 7.5 tonnes Deck edge immersion less than 20 cm Heel angle 12° – 17°	More than 7.5 tonnes Deck edge immersion more than 20 cm Heel angle more than 17°
Lifting from bulwark	Less than 10 tonnes Deck edge above waterline Heel angle less than 10°	10 – 15 tonnes Deck edge immersion less than 20 cm Heel angle 10° – 16°	More than 15 tonnes Deck edge immersion more than 20 cm Heel angle more than 16°

Simple efforts for maintaining stability

- Before attempting a heavy lift the coastguard should be informed, the warp should be brought to vessel's side, all hatches should be closed and all crew should be on deck, wearing lifejackets.
- If maximum recommended lift from the bulwark is exceeded the lift must be abandoned immediately. Position of gear should be marked and noted for retrieval by a larger vessel.
- Ensure scuppers are open and clear of obstructions to allow water to drain from the deck.
- Vessel may become unsafe if longer derricks or larger beams are fitted.

Heel Monitoring Test

The vessel heeled 9° with starboard gear on lowered derrick, port derrick topped and port gear on deck. The residual freeboard was 33 cm. 5 February 2006

Photograph of vessel
Dated 5 February 2006

FIGURE 2.11: Example stability guidance for a 24m beam trawler
Adapted from *Stability Guidance for Fishing Vessels of under 15m Overall Length*, by Maritime and Coastguard Agency (2010)

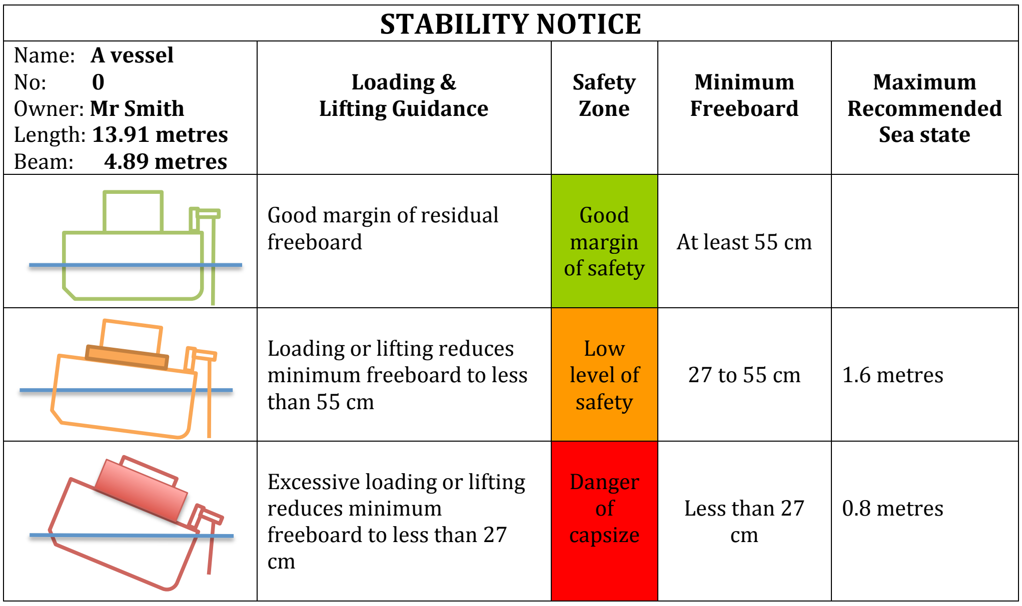

STABILITY NOTICE

Name: **A vessel** No: **0** Owner: **Mr Smith** Length: **13.91 metres** Beam: **4.89 metres**	**Loading & Lifting Guidance**	**Safety Zone**	**Minimum Freeboard**	**Maximum Recommended Sea state**
	Good margin of residual freeboard	Good margin of safety	At least 55 cm	
	Loading or lifting reduces minimum freeboard to less than 55 cm	Low level of safety	27 to 55 cm	1.6 metres
	Excessive loading or lifting reduces minimum freeboard to less than 27 cm	Danger of capsize	Less than 27 cm	0.8 metres

FIGURE 2.12: Example stability guidance for a 13.91m Decked Vessel
Adapted from *Stability Guidance for Fishing Vessels of under 15m Overall Length,* by Maritime and Coastguard Agency (2010)

During operation, vessel operators compare parameters such as freeboard with the stability notice. Since this method is designed to be used while the vessel is at sea, the measurements needed such as the vessel's beam are easily and directly measurable unlike those required for the methods discussed in the previous section (e.g. the metacentric height).

Mobile phones - Small Craft Motion Program (SCraMP)

In 2011, the Small Craft Motion Program (SCraMP) (McCue, 2012, 2013) was released for the iPhone Operating System (iOS 6.0 or later). This application is aimed at providing low budget operators, specifically fishermen, with critical information about the state of their ship, allowing them to assess vessel safety during operation. It makes use of the iPhone's accelerometer, gyroscope, magnetometer, location capabilities and microprocessor. Safety information is presented to the user in real-time in a colour-coded graphical format as seen in Figure 2.13.

Figure 2.13 shows the SCraMP application being tested with an iPhone 5 equipped with a STMicroelectronics L3G4200DH 3-axis digital micro-electro-mechanical system (MEMS) gyroscope (ST Microelectronics, 2010) and the LIS331DLH 3-Axis MEMS accelerometer (ST Microelectronics, 2007). The phone also features an AKM magnetometer and Apple's A6 processor. The application allows the user to set the sample rate of recording between 1 and 50 Hz.

In the application, the user can choose which sensor to use, what to display, limits for roll (ϕ), pitch (θ), and heave (z), and record and email data. The user can also access the data through the mobile device management application, iTunes. One particularly interesting feature

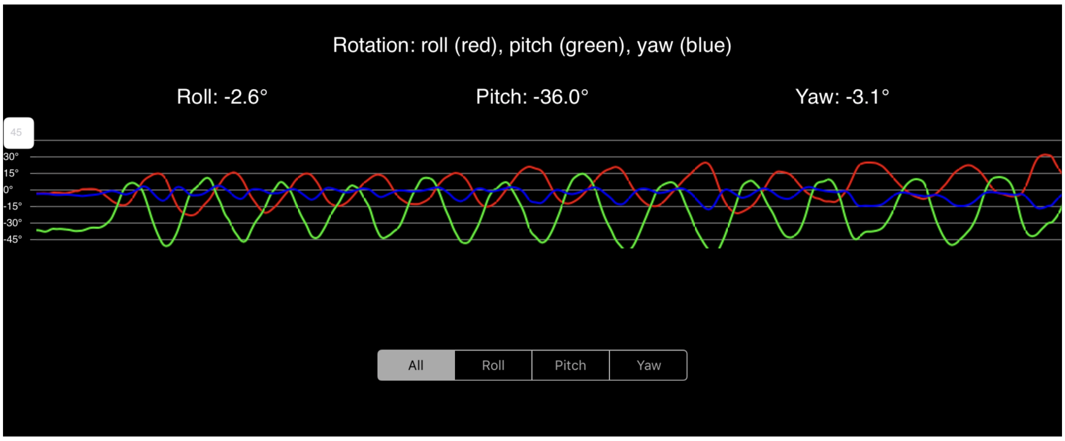

Rotation: roll (red), pitch (green), yaw (blue)

Roll: -2.6°

Pitch: -36.0°

Yaw: -3.1°

(A) Gyroscope data: Real-time rotations (roll, pitch, and yaw)

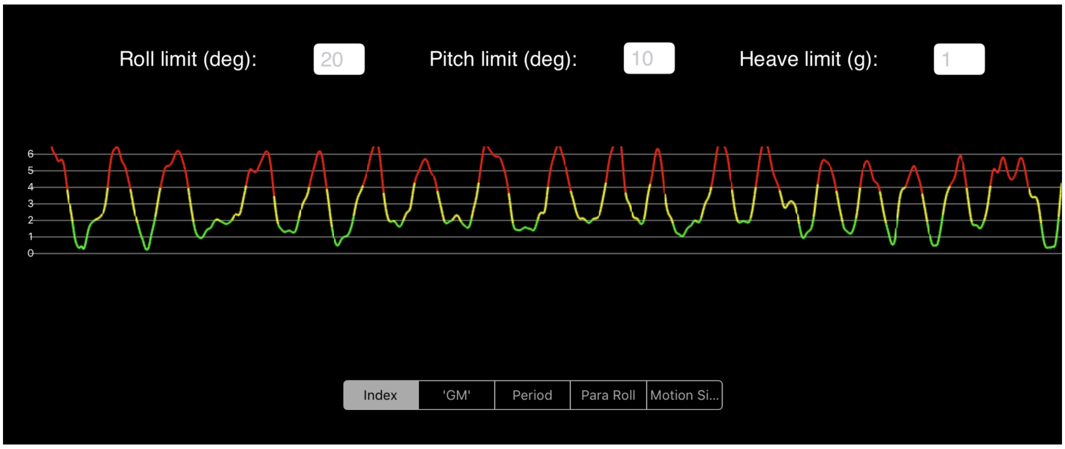

Roll limit (deg): 20

Pitch limit (deg): 10

Heave limit (g): 1

(B) Safety metrics: Real-time index. Other safety metrics include GM, period, and motion sickness

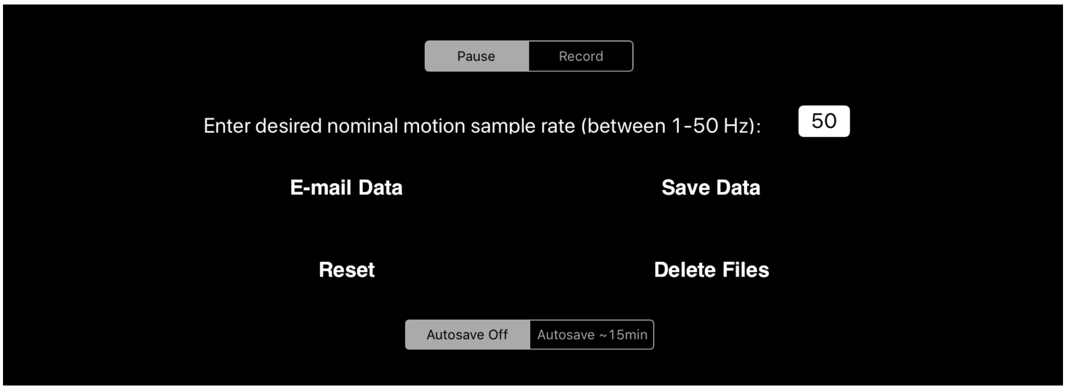

Enter desired nominal motion sample rate (between 1-50 Hz): 50

(C) Data management: Email, save or delete data files

Audible Warning: Off

Rotation Angles: Body: Tait-Bryan

(D) Selection of audible warnings and rotation angles

FIGURE 2.13: Sample screen capture from SCraMP version 3.16

of SCraMP is that it determines the vessel safety level using either an index, the roll period method, or GM as safety metrics. The index metric is loosely based upon Energy Index research by O'Reilly (1987) calculated as:

$$\text{Energy Index} = \sqrt{\phi^2 + \dot{\phi}^2 + \theta^2 + \dot{\theta}^2 + z^2 + \dot{z}^2} \tag{2.25}$$

The Energy Index was developed to identify periods of inactivity in ship motion. It was tested at sea and showed that it could discriminate between times at which large amplitude motions occur, and times of low amplitude motion (Ferrier and Manning, 1998).

Computer systems

Computer software for monitoring vessel safety and assessing risk levels have been developed (Gonzalez et al., 2012; Aronica et al., 2017). Some of these software are part of vessel information systems which also include display, communication, and sensor networks (Liu et al., 2014). These software compute variables such as the metacentric height to assess the stability of vessels (Gonzalez et al., 2016) as seen in Figure 2.14.

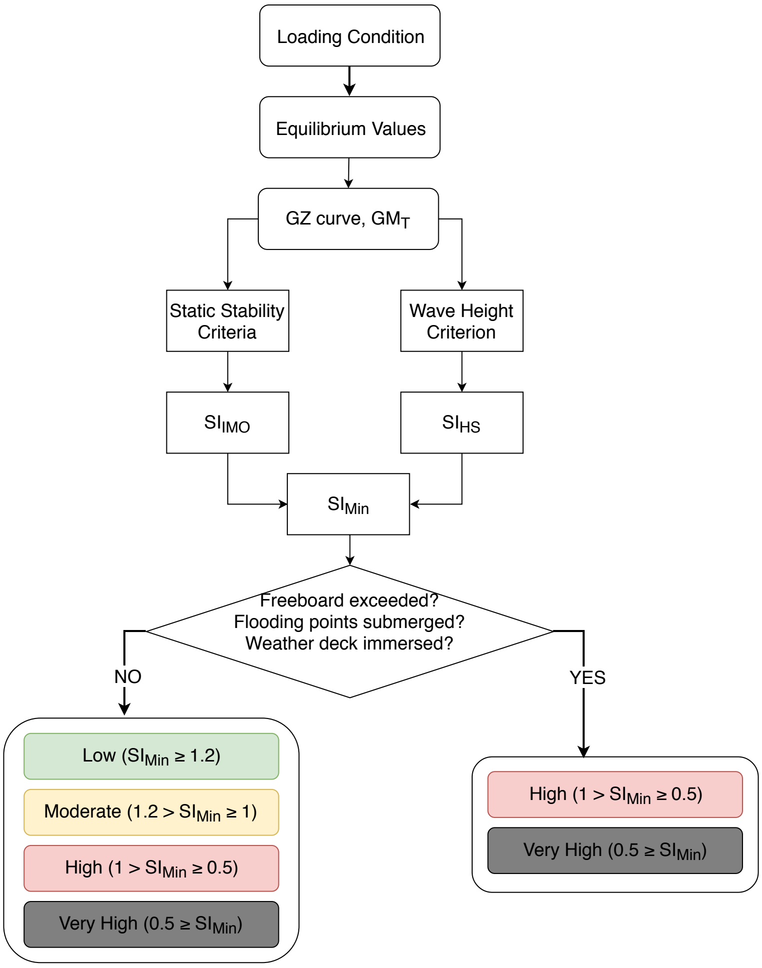

FIGURE 2.14: Calculation of risk level in Skipper stability assessment system. Adapted from *Fishing vessel stability assessment system,* by Gonzalez et al. (2012)

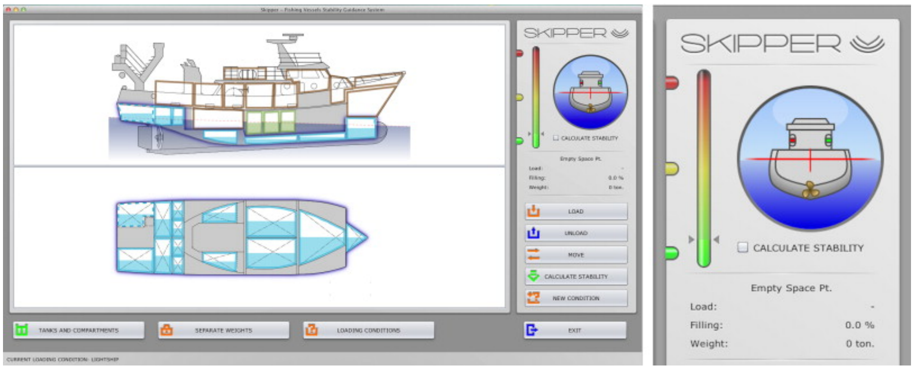

Empty Space Pt.
Load: -
Filling: 0.0 %
Weight: 0 ton.

CURRENT LOADING CONDITION: LIGHTSHIP

FIGURE 2.15: Stability guidance system graphical user interface
Adapted from *Fishing vessel stability assessment system,* by Gonzalez et al. (2012)

Figure 2.15 shows an example of such a system's user interface. Using this interface, a vessel operator views separate weight zones on a vessel and calculates stability. Their operation, installation, and acquisition costs of systems such as the one shown in Figure 2.15 can be further reduced by using single-board computers.

2.2 Vessel motion measurement

In the previous section, we discussed vessel stability and safety assessment methods. In this section, we discuss how vessel motion is measured and how measurements can be used to assess stability.

2.2.1 Single-Board Computers (SBCs)

An SBC refers to a complete computer built on single circuit board with a processor, memory, and input/output (Ortmeyer, 2014). SBCs first became available in the 1970s with one of the first being the dyna-micro (Titus, 1976). The drastic reduction in price and size of computing power over the years has led to the development of more low-cost SBCs and an increase in their popularity. SBCs are penetrating areas which were once dominated by micro-controllers (Burckle) and have been applied in areas ranging from the manufacturing industry (Gomez et al., 2015) to interactive art (Basford et al., 2016). Examples of SBCs, along with their sizes, costs, and interfaces are given in Table 2.2 (Johnston et al., 2016; Slant, 2018). The table shows that SBCs are cost-effective small form-factor devices that have the ability to communicate with a variety of peripheral devices via numerous electronic interfaces. For example, the Raspberry Pi 2 Model B+ costs $30 and can be used with a range of sensors via a number of interfaces including inter-integrated circuit (I2C) and serial peripheral interface (SPI). SBCs provide alternative solutions to continuously taking measurements in a small cost-effective, and easy to install manner. SBCs can be combined with a wide variety of sensor types to measure physical

Table 2.2: List of SBC's specifying their RAM, USBs, interfaces, size, and cost

SBC	**RAM**	**USB**	**Interfaces**	**Size (mm)**	**Cost (USD 2020)**
BeagleBone Black Rev C	512 MB	1 x USB 1 x USB miniB	ADC, 66 GPIO, SPI, I2C, UART, CAN, PWM, LCD, GPMC, MMC1, 4 Timers	86 x 53	70
BeagleBone Green Wireless	512 MB	4 x USB 2.0 Host	SPI, I2C, UART, PWM, 4 Timers	86 x 53	60
ODROID - C1+	1 GB	4 x USB 2.0 Host 1 x USB 2.0 OTG	ADC, 40 GPIO, SPI, I2C, UART, HDMI, RTC, IR Receiver, DMC, PLL/OSC	85 x 56	50
ODROID - C2	2 GB	4 x USB 2.0 Host 1 x USB 2.0 OTG	ADC, 40 GPIO, SPI, I2C, UART, HDMI, RTC, IR Receiver, DMC, PLL/OSC	85 x 56	60
ODROID - XU4	2 GB	1 x USB 2.0 2 x USB 3.0	ADC, 42 GPIO, SPI, I2C, UART, PWM, RTC I2S, HDMI, PMIC	83 x 59	80
Pine A64	512 MB / 1 GB / 2 GB	4 x USB 2.0	ADC, GPIO pins, UART, SPI, I2C, IR Receiver, HDMI	127 x 79	30
Raspberry Pi 4 Model B	2 GB / 4 GB	2 x USB 2.0 2 x USB 3.0	ADC, GPIO pins, UART,SPI,I2C	86 x 57	40
Raspberry Pi 3 Model B+	1 GB	4 x USB 2.0	ADC, GPIO pins, UART,SPI,I2C	86 x 57	40
Raspberry Pi 2 Model B+	1 GB	4 x USB 2.0	ADC, GPIO pins, UART, SPI, I2C	86 x 57	30
Raspberry Pi 1 Model B+	512 MB	2 x USB 2.0	ADC, GPIO pins, UART, SPI, I2C	86 x 57	30
Raspberry Pi Zero W	512 MB	1 x Micro-USB	ADC, GPIO pins, UART, SPI, I2C	65 x 30	20
Udoo Neo	512 MB / 1 GB	1 x USB 2.0 Host 1 x USB 2.0 OTG	ADC, GPIO pins, UART, CAN Bus, PWM, I2C, SPI	89 x 59	100
Udoo x86 Ultra	8 GB	3 x USB 3.0	GPIO pins, UART, CAN Bus, PWM, I2C, SPI	120 x 85	270

properties (Fraden, 2010). When combined with inertial measurement units, SBCs can be used to measure vessel motion.

2.2.2 Inertial Measurement Units (IMUs)

The cost of technology has been consistently falling over the years as seen in Figure 2.16. This makes the use of cheap sensors in cost-effective vessel monitoring systems for low-cost fishermen possible. This reduction in price is accompanied by an increase in computing speed in terms of microprocessor clock speed (Holdowsky et al., 2015).

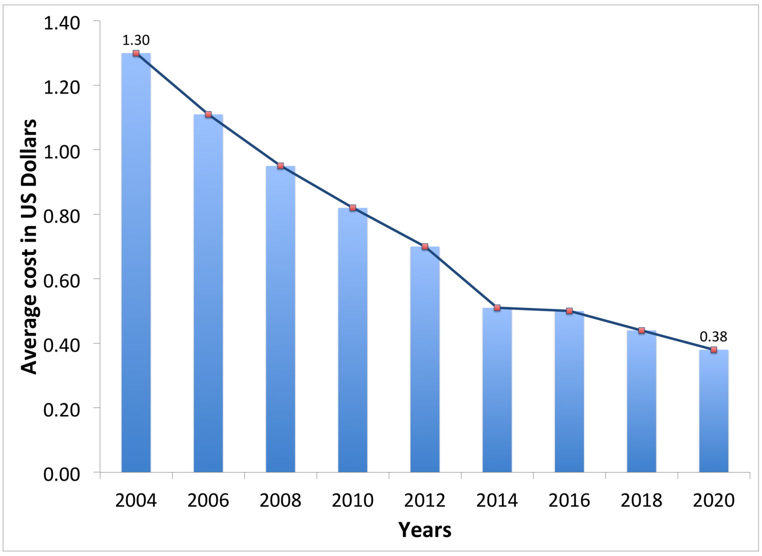

Figure 2.16: Average cost of industrial Internet of Things (IoT) sensors from 2004 to 2020 in U.S. dollars. Adapted from *The Internet of Everything,* by Business Insider Intelligence (2015)

This reduction in price has also contributed to the development of micro-electromechanical systems (MEMS). MEMS devices are micro-scale devices that use manufacturing processes similar to those used in the making of integrated circuits (IC). While IC are strictly electrical systems, MEMS devices are both mechanical and electrical systems allowing them to interact with the real world. Accelerometer, gyroscopes and magnetometers, which are used in inertial measurement units (IMUs) are common examples of MEMS devices.

IMUs are devices used to measure an object's accelerations, angular velocity and magnetic field around the object. They consist of accelerometers, gyroscopes, and magnetometers. They have been used in a varying number of industries ranging from the aerospace industry to determine the centre of gravity during flight (Al-Rawashdeh et al., 2014) to human activity monitoring (Banos et al., 2014). There has also been research into their use in measuring ship hydroelastic response by Bennett et al. (2014). Within the maritime industry, they have been used in vessel monitoring systems such as those offered by Hoppe Marine (2018) and Totem Plus (2015). These systems are aimed at larger operators such as ferries and container ships, rendering them too expensive for fishermen.

Gyroscopes are devices used to measure angular velocity in units of either rotations per minute (RPM) or degrees per second (°/s). They are useful for monitoring changes in the orientation of an object during motion. They measure angular velocity by detecting shifts in a small resonating mass, which is then converted to an electrical signal. Some choices for the resonating masses include vibrating wheels and tuning forks.

Accelerometers are devices used to measure the acceleration of an object. The measured acceleration could be either static, like the acceleration due to gravity, or dynamic due to vibrations. Measurements are made in either meters per second squared (m/s^2) or g-force (g), where 1 g is equivalent to 9.8 m/s^2. The measurement of acceleration in accelerometers can be based on a number of methods. Two of the most popular methods are the piezoelectric effect or capacitance (Dimension Engineering, 2014). With the piezoelectric effect, acceleration is measured using voltage generated as a result of microscopic crystal structures being stressed. With capacitance-based accelerometers, acceleration is measured due to changes in capacitance resulting from the movement of structures. The average price of accelerometers has reduced from $2 in 2006 to 40 cents (Simpson and Lamb, 2014).

Magnetometers are devices used to measure or detect the strength of a magnetic field around an object in units of Tesla. This measurement is done by measuring the change in a variable such as voltage, resonant frequency, or mechanical displacement. The change could be as a result of a number of different phenomena resulting in different approaches for magnetic sensing.

SBCs coupled with IMUs are not traditionally used to measure vessel motion. The next section presents some of these traditional methods.

2.2.3 Related vessel motion measurement solutions

Traditional methods of measuring vessel motion include the use of commercially available IMUs, towing tank dynamometers, and optical motion capture systems.

Commercially available inertial measurement units

Commercially available IMUs are used in a wide range of applications involving motion measurement. Examples of commercially available IMUs are presented in Table 2.3.

The MTi sensors produced by XSens have been used by MARIN Wageningen, a leading research institution, to measure vessel motion in their Lashing@Sea project (Koning, 2009). There are other products on the market similar to this which have also been purposefully built for measuring ship motion such as the Ekinox-A sensor (SBG Systems, 2017). The MTi 10-series gives the systems integrator a choice of three different integration levels (inertial measurement unit, variable reluctance sensor or attitude and heading reference system). These sensors are built specifically for industry, large vessels, and offshore structures and have a significantly higher cost than the IMUs used with SBCs. This high cost usually includes a software suite, allowing users to easily configure the sensors through an easy-to-use graphical interface. For fishermen,

Table 2.3: Size, weight and capabilities of commercially available IMUs. Adapted from *A wearable inertial measurement unit for long-term monitoring in the dependency care area,* by Rodri-guez Martin et al. (2013)

IMU	**Size (mm)**	**Weight (g)**	**Onboard storage unit**	**Wireless capabilities**
XSens Mtw	34.5 x 58 x 4.5	27	No	Yes
XSens Mti-G	58 x 58 x 28	68	No	No
Shimmer MainUnit +	53 x 32 x 25	22	Yes	Yes
Technoconcept KineO	49 x 38 x 19	25	No	Yes
EPFL Physilog 3	50 x 40 x 16	36	Yes	No
Microstrain 3DM-GX1	64 x 90 x 25	74.6	No	No
Sparkfun UAV V3	38 x 70 x 25	34	No	No

the specifications of a high-cost motion measurement unit are not necessary. For instance, the XSens MTi sensor has an output frequency of up to 2 kHz, but for measuring vessel motion, 5 Hz is sufficient (Maritime Research Institute Netherlands, 2012).

Optical motion capture systems

Optical motion capture systems are used for measuring vessel motion in towing tanks (Bockmann and Steen, 2016). They use cameras placed around a desired volume to track the movements of markers placed on a body of interest. The tracking is enabled by either the reflection of infrared light emitted by the camera off the markers or markers that are powered by a battery and emit their own light. The high sampling rates enable them to capture fast movements. The main advantage of these systems is that they have higher positional accuracy and precision than IMUs (Jackson, 2017). This is because using 6 DOF motion estimated using IMUs is extremely sensitive to errors in the accelerometer and gyroscope (Seaman and McPhee, 2012). The major disadvantage of using this system is that they cannot be used by vessels at sea as they require a shore-based setup for the cameras.

2.3 Computing roll period from roll motion measurements

Section 2.1.3 introduced roll period as a method for assessing fishing vessel stability and Section 2.2 discussed methods of measuring vessel motion. This section links the two sections mentioned by discussing how the roll period can be computed from roll motion measurements using spectral analysis to obtain a spectrum from the recorded time series, and the implications for applying the methodology developed at full-scale.

There are different methods for estimating the spectrum which can be divided into two groups: parametric and non-parametric methods (Krishna and Andrews, 2015; Thomas et al., 2015). Non-parametric methods are less computationally complex than parametric methods. A disadvantage of non-parametric methods is their use of windowing functions, leading to distortions in the computed spectra. Fourier analysis is a non-parametric method of estimating spectra from recorded time series.

‘Fourier analysis is one of the most commonly used methods for identifying periodic components in near-stationary time series oceanographic data’ (Emery and Thomson, 2001). The individual components in the fourier series can be used to estimate the energy per unit frequency bandwidth of a recorded time series otherwise known as the power spectrum. Fourier transformations are defined by the forward transform

$$\begin{aligned} \mathcal{F}\left\{x(t)\right\} = S(f) &= \int_{-\infty}^{\infty} x(t)\exp(-i2\pi ft)\mathrm{dt} \\ \mathcal{F}\left\{x(t)\right\} = S(\omega) &= \int_{-\infty}^{\infty} x(t)\exp(-i\omega t)\mathrm{dt} \end{aligned} \tag{2.26}$$

and the inverse transform

$$\begin{aligned} \mathcal{F}^{-1}\left\{S(f)\right\} = x(t) &= \int_{-\infty}^{\infty} S(f)\exp(-i2\pi ft)\mathrm{df} \\ \mathcal{F}^{-1}\left\{S(\omega)\right\} = x(t) &= \frac{1}{2\pi}\int_{-\infty}^{\infty} S(\omega)\exp(-i\omega t)\mathrm{d}\omega \end{aligned} \tag{2.27}$$

Fourier transformations are based on the fourier series, which assumes that a time series $x(t)$ of finite length that repeats itself infinitely with period T such that $x(t) = x(t+T)$ can be represented as a superposition of trigonometric functions (Weisstein, 2018)

$$\begin{aligned} x(t) &= \frac{a_0}{2} + \sum_{n=1}^{\infty}\left[a_n\cos\left(\frac{2\pi}{T}nt\right) + b_n\sin\left(\frac{2\pi}{T}nt\right)\right] \qquad \text{for } n = 0{,}1{,}2{,}... \\ x(t) &= \sum_{n=-\infty}^{\infty}\left[c_n\cdot\exp\left(i\frac{2\pi}{T}nt\right)\right] \end{aligned} \tag{2.28}$$

where

$$\begin{aligned} a_0 &= \frac{2}{T}\int_{-T/2}^{T/2} x(t)\mathrm{dt}, \\ a_n &= \frac{2}{T}\int_{-T/2}^{T/2} x(t)\cos\left(\frac{2\pi}{T}nt\right)\mathrm{dt}, \\ b_n &= \frac{2}{T}\int_{-T/2}^{T/2} x(t)\sin\left(\frac{2\pi}{T}nt\right)\mathrm{dt}, \\ c_n &= \frac{1}{T}\int_{-T/2}^{T/2} x(t)\exp\left(i\frac{2\pi}{T}nt\right)\mathrm{dt} \end{aligned} \tag{2.29}$$

If a continuous time series, $x(t)$ is sampled at a specific frequency, $1/\delta t$, with the time interval between points as δt, the total number of sample intervals, N equals $T/\delta t$. There are therefore $N+1$ sample points meaning Fourier analysis can be used for $n = 0{,}1{,}2$ ... to N. The Nyquist frequency, f_{Nyquist}, which is the highest frequency component that can be resolved without errors, is half the sampling frequency (Oppenheim et al., 1999).

$$f_{\text{Nyquist}} = \frac{1}{2\delta t} \tag{2.30}$$

When sampling a continuous time series to produce a discrete signal of finite uniformly spaced samples, $x(n)$ with N points, the fourier transformation is achieved through the Discrete Fourier Transform (DFT) and its inverse.

$$\mathcal{F}\left\{x[n]\right\} = S[k] = \sum_{n=0}^{N-1}\left[x[n]\cdot\exp\left(-i\frac{2\pi}{N}kn\right)\right] \tag{2.31}$$

$$\mathcal{F}^{-1}\left\{S[k]\right\} = x[n] = \sum_{k=0}^{N-1}\left[S[k]\cdot\exp\left(i\frac{2\pi}{N}kn\right)\right] \tag{2.32}$$

Computing the DFT is very slow therefore the Fast Fourier Transform (FFT) is used instead as it can compute the fourier transforms quicker while maintaining the accuracy of the DFT (Sevgi, 2007). For time series data collected by wave-buoys, this processing results in the wave spectrum from which parameters such as significant wave height are computed and made readily available (Earle, 1996). FFT can also be used to estimate sea state from ship motions (Johnson and Wilson, 2005; Pascoal and Soares, 2008).

The resolution of the frequencies for each DFT is determined by the sampling rate, f_s, and the number of data points, N (Oppenheim et al., 1999). Therefore, time (t) is the only variable affecting frequency resolution as shown in Equation 2.36.

$$\Delta f = \frac{f_s}{N} = \frac{f_s}{f_s\cdot t} = \frac{1}{t} \tag{2.33}$$

The maximum resolution uncertainty of the DFT is assumed as half of the frequency resolution (Fornasini, 2008) as shown in Equation 2.37.

$$\delta f_{max} = \frac{\Delta f}{2} \tag{2.34}$$

Vessel motion recorded as time series data is made up of linear combinations of periodic or quasi-periodic components and random high-frequency noise. The periodic and quasi-periodic components exist because the cause of this motion, i.e. the complex sea surface, can be thought of as a superposition of regular waves as seen in Section 3.2. The high-frequency noises may be from either the sensor or the recording environment. In the context of vessel stability assessment, the aim of analysing the recorded data is to separate the periodic oscillation from the random noise to be able to accurately detect the period of motion. This is important because roll period is related to vessel stability.

There are a number of issues to consider when computing FFT on a discrete time series including aliasing, spectral leakage and scalloping, discussed in the following section.

2.3.1 Sources of error

Aliasing occurs when the sampling frequency is lower than twice the signal's maximum frequency. When this occurs, the signal reconstructed from the Fast Fourier Transform is different from the original signal as a result of a loss of information as shown in Figure 2.17. Aliasing can be prevented through the use of filters to reduce frequency components above half the sampling frequency or sampling at a higher frequency.

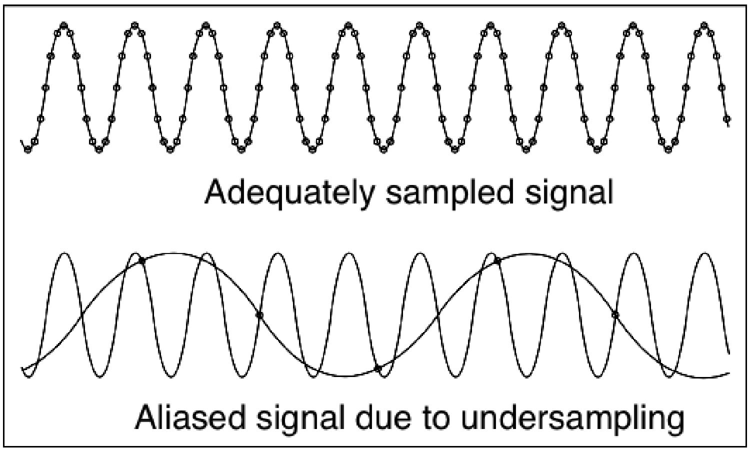

Figure 2.17: Aliasing due to under sampling (Cerna and Harvey, 2000)

Spectral leakage occurs when the total sampling time, T, is not an integer multiple of the period of the signal being measured. According to Walker (1996), 'The time-domain rationale for spectral leakage is that, for a waveform that is not periodic in time, the temporal effect of the sample window becomes visible in the Fourier transform.' Since one is usually measuring an unknown stationary signal, sampling an integral multiple of periods is not guaranteed. Window functions are used to reduce spectral leakage. Even though there is no general method of choosing a window, Table 2.4 suggests some choices based on the content of the signal being measured. The Hann window is appropriate 95 % of the time. It adequately reduces spectral leakage and has good frequency resolution (Cerna and Harvey, 2000).

Table 2.4: Window choice based on signal content (Cerna and Harvey, 2000)

Signal content	**Window**
Sine wave or combination of sine waves	Hann
Sine wave (amplitude accuracy is important)	Flat top
Narrowband random signal (vibration data)	Hann
Broadband random (white noise)	Uniform
Closely spaced sine waves	Uniform, Hamming
Excitation signals	Force
Response signals	Exponential
Unknown content	Hann

The use of windowing functions results in a reduction in the amplitude of spectra. For an N-point FFT of an arbitrary discrete sinusoidal wave with peak amplitude A, the peak magnitude of the calculated spectra M_{peak} falls in the range shown in Equation 2.35. The underestimation of the time-domain peak amplitude using the spectra is known as scalloping (Lyons, 2011). The choice of windows affects the level of scalloping as shown in Figure 2.18.

$$\frac{0.637 \cdot A \cdot N}{2} \leq M_{peak} \leq \frac{A \cdot N}{2} \tag{2.35}$$

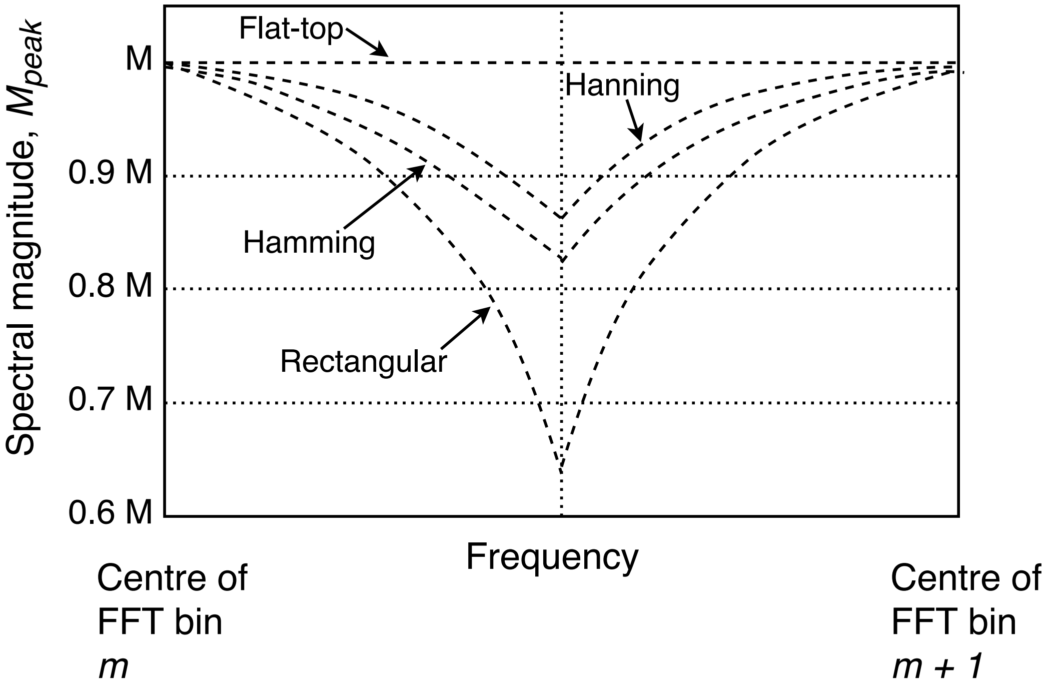

Figure 2.18: Windowed FFT Scalloping (Lyons, 2011)

2.3.2 Welch's method

Welch (1967) developed a method of applying FFT to estimating the power spectra which has the advantage of a reduction in the number of computations. Welch's method estimates the power spectral density by dividing the data into overlapping segments, calculating a modified periodogram (Schuster, 1898; National Semiconductor Corporation, 1980) for each segment and averaging the periodograms as shown in Figure 2.19. If there is no overlap, this method is similar to the method developed by Bartlett (1950).

In order validate Welch's method for computing the spectrum for vessel motion time series data to obtain the period of motion, a time series collected using a wave buoy for a known sea spectrum is used to reproduce the spectrum.

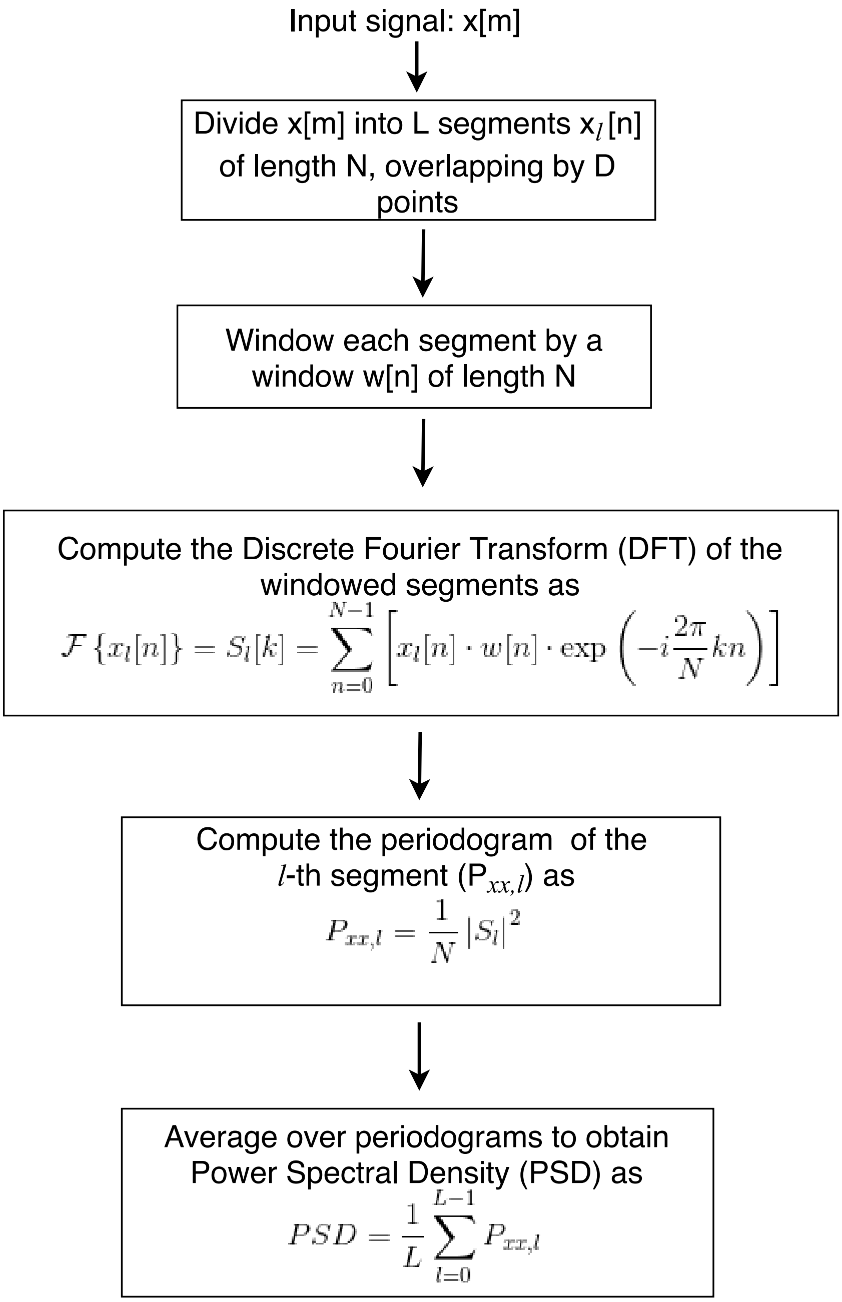

FIGURE 2.19: Welch's method for computing the PSD for time series data.

The data used in this section was obtained from the Coastal Data Information Program (2015) which monitors and predicts waves and shoreline changes. Table 2.5 presents a summary of the details of the wave buoy used to collect the data and Figure 2.20 shows the location of the wave buoy.

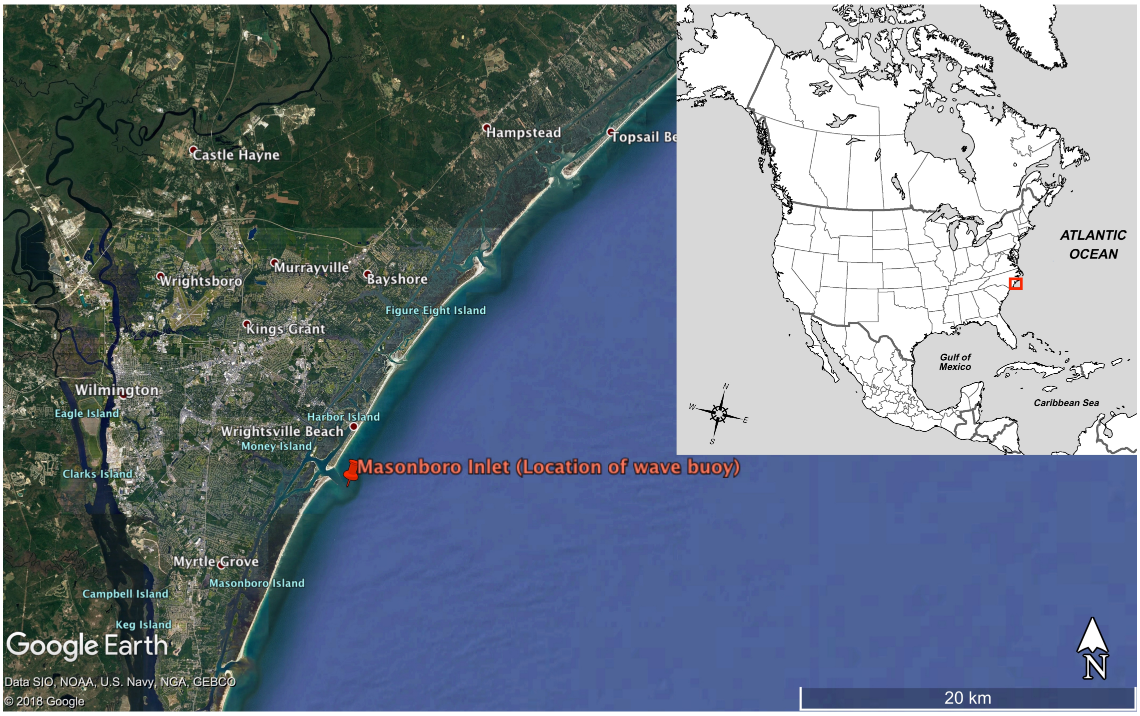

FIGURE 2.20: Location of wave buoy

TABLE 2.5: Wave buoy data

CDIP station ID	15001
Location	34 8.468' (N), 77 42.995' (W)
Water Depth	17 meters
Distance offshore	Approximately 6.5 nautical miles
Measured parameters	Wave energy, wave direction, sea temperature
Sample rate (f_s)	1.28 Hz
Date of data collection	31st July 2015
Length of data collection	30 mins

The x, y, and z motion time series of the wave buoy (shown in Figure 2.21) were obtained, but since the focus of this section was on reproducing the non-directional wave spectrum, the emphasis was on the z time series. Using this time series, we determined a parameter which is recommended to be used to characterise a sea state; peak period (Rye, 1977).

As can be seen from Figure 2.21, determining variables such as the average period from the time series data requires conversion of the time series data into the frequency domain. This was done using the Scipy (2014) library for the Python programming language. During the power spectral density estimation, the entire thirty-minute data recording was divided into fifteen two-minute (120 s) segments, with the segments overlapping by 50% (60 s). These segment lengths and

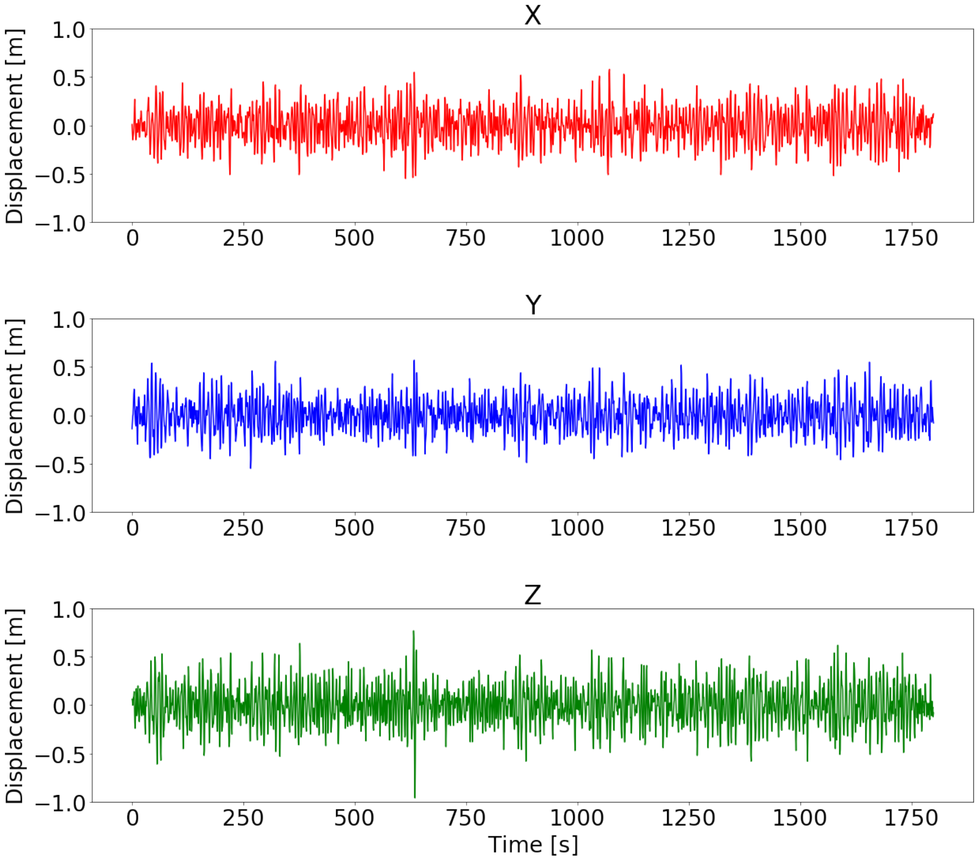

FIGURE 2.21: Wave buoy time series

overlaps are chosen as they are similar to segment lengths and overlap used in current wave buoy data analysis techniques (Earle, 1996).

The resolution of the frequencies for each DFT is determined by the sampling rate, f_s, and the number of data points, N (Oppenheim et al., 1999) as shown in Equation 2.36.

$$\Delta f = \frac{f_s}{N} = \frac{f_s}{f_s \cdot t} = \frac{1}{120} = 0.00833 \text{ Hz} \tag{2.36}$$

The maximum resolution uncertainty of the DFT is assumed as half of the frequency resolution (Fornasini, 2008) as shown in Equation 2.37.

$$\delta f_{max} = \frac{\Delta f}{2} = \frac{0.00833}{2} = 0.00417 \text{ Hz} \tag{2.37}$$

Table 2.6 shows the variables used to compute the spectra shown in Figure 2.22. Appendix A shows the effect of different parameters (the length of segment used, window, typing of scaling, and manner of detrending) on the spectra obtained using Welch's method.

Figure 2.22 shows the spectrum produced from the wave buoy time series data using the Welch method with the Z axis showing the comparison between the computed wave spectrum and the wave spectrum on the CDIP website.

TABLE 2.6: Welch method parameters used to reproduce the wave spectrum

Parameter	**Input**
Window	Hanning
Number of points in each segment (nperseg $= f_s \cdot t$)	154
Number of points to overlap between segments	77 (nperseg / 2)
Detrend	Constant
Scaling	Spectrum

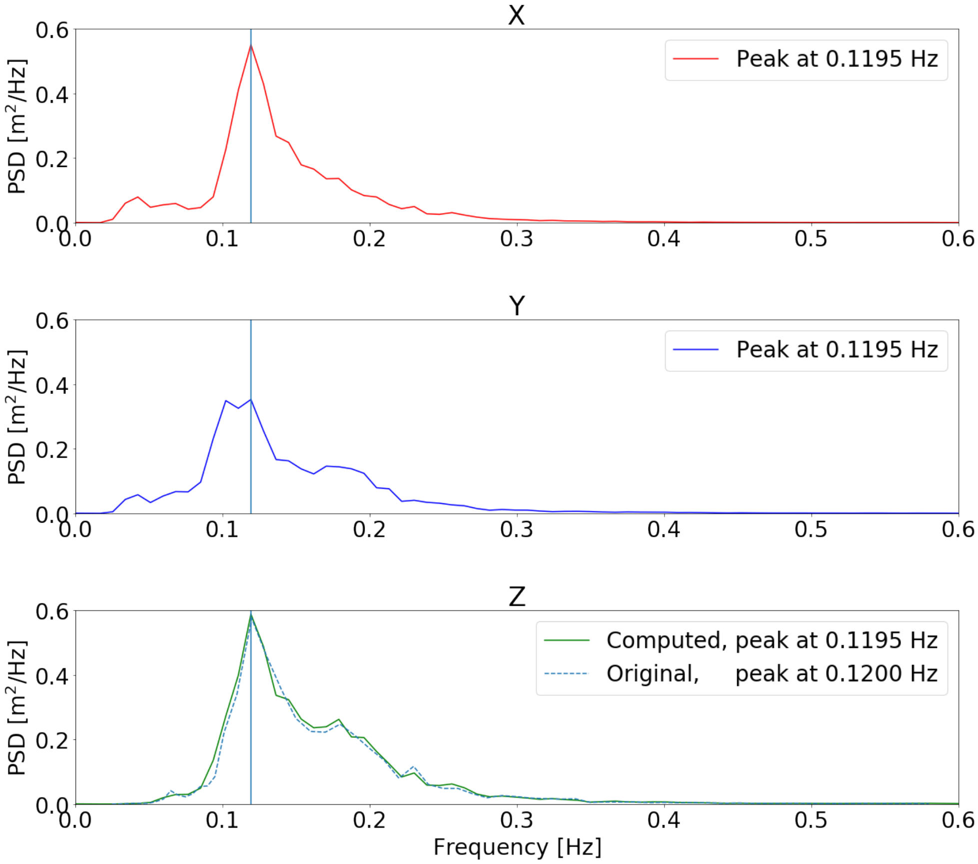

FIGURE 2.22: Wave buoy Spectrum

From Figure 2.22, the peak frequency was determined as the frequency at which the spectrum had a maximum value. The peak period was calculated by taking the inverse of the peak frequency.

TABLE 2.7: Comparison of computed variables with variables stated on the CDIP website

	Computed	CDIP Website
Peak frequency [Hz]	0.1195	0.1200
Peak period [s]	8.37	8.33

2.3.3 Implications for application at full scale

The comparisons of the peak frequency and peak period computed using the proposed methodology against those from the CDIP website as shown in Table 2.7 demostrate that the proposed methodology can be applied to data measured at full scale. To ensure that results from tests in subsequent chapters are applicable at full scale, all measurements at model scale are converted into full-scale according to Froude scaling laws using the conversion factors shown in Table 2.8

TABLE 2.8: Froude Scaling Conversion Factors.
Adapted from *Data analysis methodologies for hydrodynamic experiments in waves,* by Islam et al. (2016)

Quantity	Unit	Scale factor
Acceleration	m/s^2	λ^0
Area	m^2	λ^2
Density	kg/m^3	λ^0
Force	N	λ^3
Frequency	s^{-1}	$\lambda^{-0.5}$
Length	m	λ^1
Mass	kg	λ^3
Moment	$N-m$	λ^4
Pressure	N/m^2	λ^1
Speed	m/s	$\lambda^{0.5}$
Time	s	$\lambda^{0.5}$

Based on the time conversion factor in Table 2.8 and assuming a scale factor of 15, the range of roll periods to be tested equivalent to full-scale roll periods between 5 and 20 seconds can be computed. This range of roll periods is used because this covers the range of typical roll periods for fishing vessels. The equivalent roll periods and frequencies for this range are shown in Table 2.9

TABLE 2.9: Full-scale and model roll periods and frequency

Full scale roll period (s)	Full scale roll frequency (Hz)	Model roll period (s)	Model roll frequency (Hz)
5.0	0.200	1.291	0.775
6.0	0.167	1.549	0.645
7.0	0.143	1.807	0.553
8.0	0.125	2.066	0.484
9.0	0.111	2.324	0.430
10.0	0.100	2.582	0.387
11.0	0.091	2.840	0.352
12.0	0.083	3.098	0.323
13.0	0.077	3.357	0.298
14.0	0.071	3.615	0.277
15.0	0.067	3.873	0.258
16.0	0.062	4.131	0.242
17.0	0.059	4.389	0.228
18.0	0.056	4.648	0.215
19.0	0.053	4.906	0.204
20.0	0.050	5.164	0.194

2.4 Comparison of accelerometers

After introducing the Welch method as a suitable approach to determining the period of motion and evaluating it by reproducing a known spectrum, we assessed different accelerometers in accurately determining the period of motion produced by a vibration shaker table. The accelerometers compared were a PCB piezotronics single-axis accelerometer model 352C22 (PCB Piezotronics MTS Systems Corporation, 2016), a LIS331DLH accelerometer (ST Microelectronics, 2007) in an iPhone 5s, and an LSM303D 3-axis accelerometer (ST Microelectronics, 2013) onboard a Pololu MinIMU-9 v3 (Pololu Robotics and Electronics, 2016) coupled with a Raspberry Pi 2B+ (Raspberry Pi Foundation, 2015).

Experimental setup

The data was collected using the experimental setup shown in Figure 2.23, consisting of a Derritron VP 4 shaker, a signal generator, and a professional mosfet power amplifier.

Input signals used were sinusoidal waves with frequencies between 0.2 Hz to 1.0 Hz and data was collected for 110 seconds. These frequencies were chosen as low frequencies / high period to test the ability of the accelerometers to detect low frequency, low amplitude motions. The

Figure 2.23: Experimental setup showing the shaker, power amplifier, and a signal generator.

PCB piezotronics single-axis accelerometer had a sensitivity of 10 millivolts per g (mV/g), the LIS331DLH 3-axis accelerometer in the iPhone 5s had a sensitivity of 4 (mg per least significant bit) mg/LSB, and the LSM303D 3-axis accelerometer onboard the Pololu MinIMU-9 v3 had a sensitivity of 12 mg/LSB. It is important to note that the sensitivity of each accelerometer is determined by not only the number of bits but also the range of the accelerometer. Twelve bits over an 8 g range is not the same as 12 bits over a 2 g range. Over an 8 g range, 12 bits will give 512 counts/g, and over a 2 g range, 12 bits will give 2048 counts/g, which is 4 times more sensitive (Tuck, 2010).

The Raspberry Pi collected motion data from the LSM303D accelerometer via the Inter-Integrated Circuit (I2C) protocol using a C++ program (Grayson, 2014). The LIS331DLH accelerometer in the iPhone collected measurements using the Small Craft Motion Program (SCraMP) application discussed in Section 2.1.4.2. The PCB Piezotronics accelerometer required the most amount of additional hardware and used a SignalCalc Ace signal analyser (Data Physics Corporation, 2016a) and software (Data Physics Corporation, 2016b) running on a Latitude E6430 laptop (Dell, 2013). All the accelerometers sampled at a rate of 12 Hz.

Once the data was collected by all three accelerometers, the time series were converted to the frequency domain using the Welch Method. Before this method was used to compute the spectra, the first and last five seconds of the data recorded by each accelerometer are discarded to account for ramp up and ramp down times of the shaker.

Figure 2.24 shows the accelerations recorded by the PCB Piezotronics accelerometer at rest and frequencies between 0.2 Hz and 1.0 Hz. There was a gradual reduction in the maximum amplitude of the accelerations as the frequency was reduced. Figure 2.25 shows the spectra computed from the data shown in 2.24 using Welch's method, and the peak frequencies identified using a peak

Table 2.10: Comparison of peak periods for a PCB Piezotronics accelerometer with a sensitivity of 100 mg/mV, a LIS331DLH accelerometer in an iPhone 5 with a sensitivity of 4 mg/LSB, and a LSM303DLHC accelerometer on a Pololu IMU plugged into a Raspberry Pi with a sensitivity of 12 mg/LSB

Input frequency [Hz]	PCB Piezotronics peak frequency [Hz]	iPhone peak frequency [Hz]	Pololu peak frequency [Hz]
0.00	0.24	0.34	0.00
0.20	0.20	0.40	0.00
0.30	0.30	0.30	0.00
0.40	0.38	0.40	0.14
0.50	0.48	0.50	0.50
0.60	0.58	0.60	0.60
0.70	0.68	0.70	0.70
0.80	0.78	0.80	0.82
0.90	0.88	0.90	0.92
1.00	0.98	1.00	1.02

finding algorithm (Negri, 2016). When using Welch's method in this chapter, the data is not divided into smaller segments as the total length of 100 s provided a consistent estimate of the power spectrum in this situation. This was equivalent to computing the periodogram.

The results, as summarised in Table 2.10, show that all of the accelerometers considered were able to accurately detect and differentiate between frequencies from 0.5 Hz to 1.0 Hz, with the PCB Piezotronics accelerometer being able to accurately differentiate between the entire range of frequencies investigated. The accuracy of the detected peak values is ± 0.01 Hz (the maximum frequency resolution error).

These results are as expected considering the sensitivities of the accelerometers used. For the analogue PCB Piezotronics accelerometer, a sensitivity of 10 mV/g (1.0 mV/(m/s^2)) was enough to accurately detect the peak period in the frequency range investigated. For the digital accelerometers, the LIS331DLH accelerometer used in the iPhone gave better results than the LSM303DLHC accelerometer used on the Pololu IMU connected to the Raspberry Pi. This is because the LIS331DLH accelerometer has a sensitivity of 4 mg/LSB while the LSM303DLHC has a sensitivity of 12 mg/LSB. It is important to check the unit of sensitivity when comparing accelerometers as the higher the value in mV/mg (for analogue accelerometers) or in LSB/mg (for digital accelerometers), the more sensitive the accelerometer is. However, if the units are in mg/mV (for analogue accelerometers) or in mg/LSB (for digital accelerometers), the lower the value, the more sensitive the accelerometer.

Besides the sensitivity of the accelerometer, there were other practical issues to consider such as additional hardware required for data collection and processing capability of the sensing platform. The PCB Piezotronics accelerometer required both an analyser and a laptop to store the data as the experiment was conducted. On the other hand, the iPhone and Raspberry Pi stored the collected data locally. With the PCB Piezotronics accelerometer, the analyser software running on the laptop provided time history, windowed time history, linear spectrum,

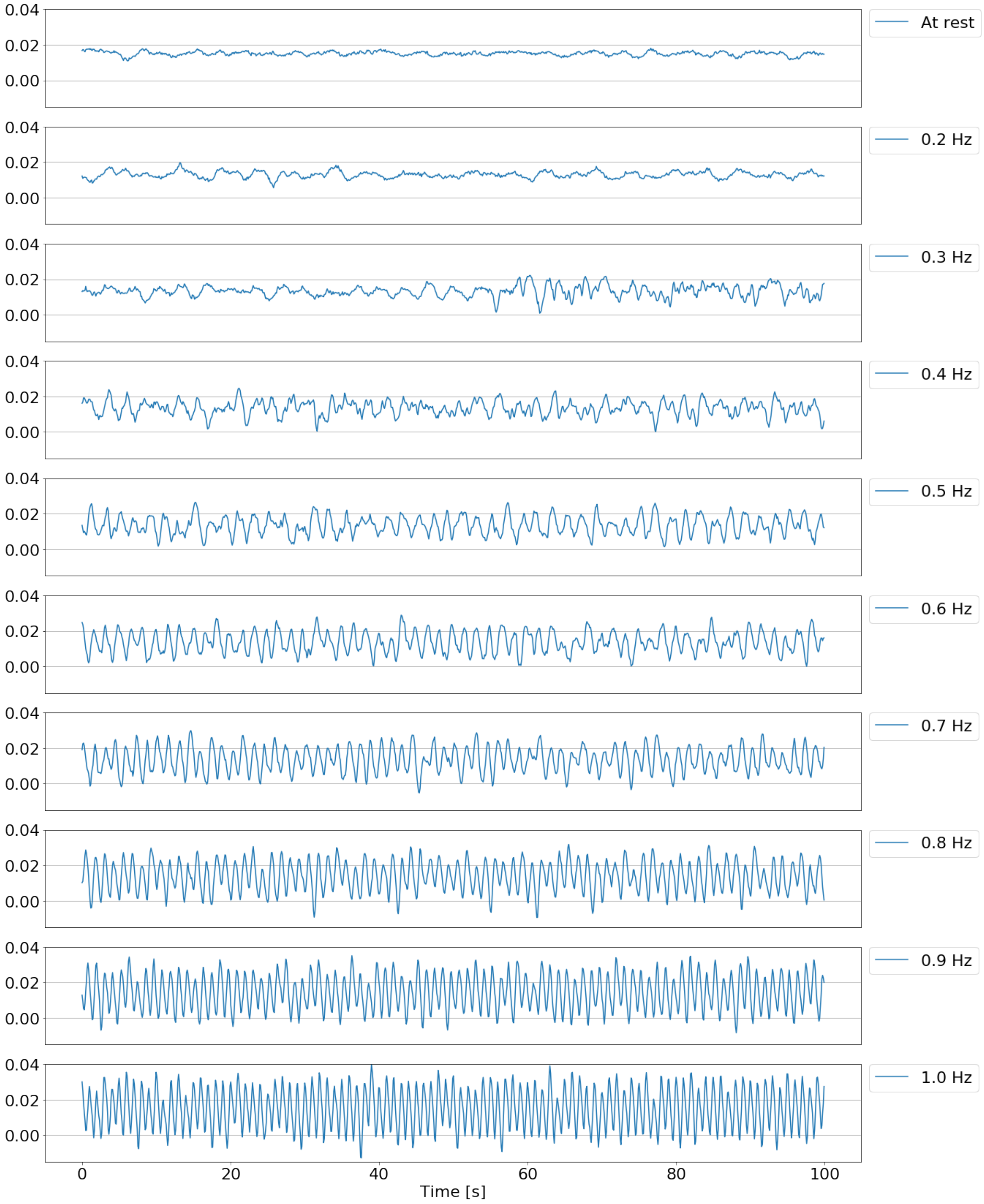

FIGURE 2.24: Accelerations collected with the PCB Piezotronics accelerometer at rest and at frequencies between 0.2 Hz and 1.0 Hz

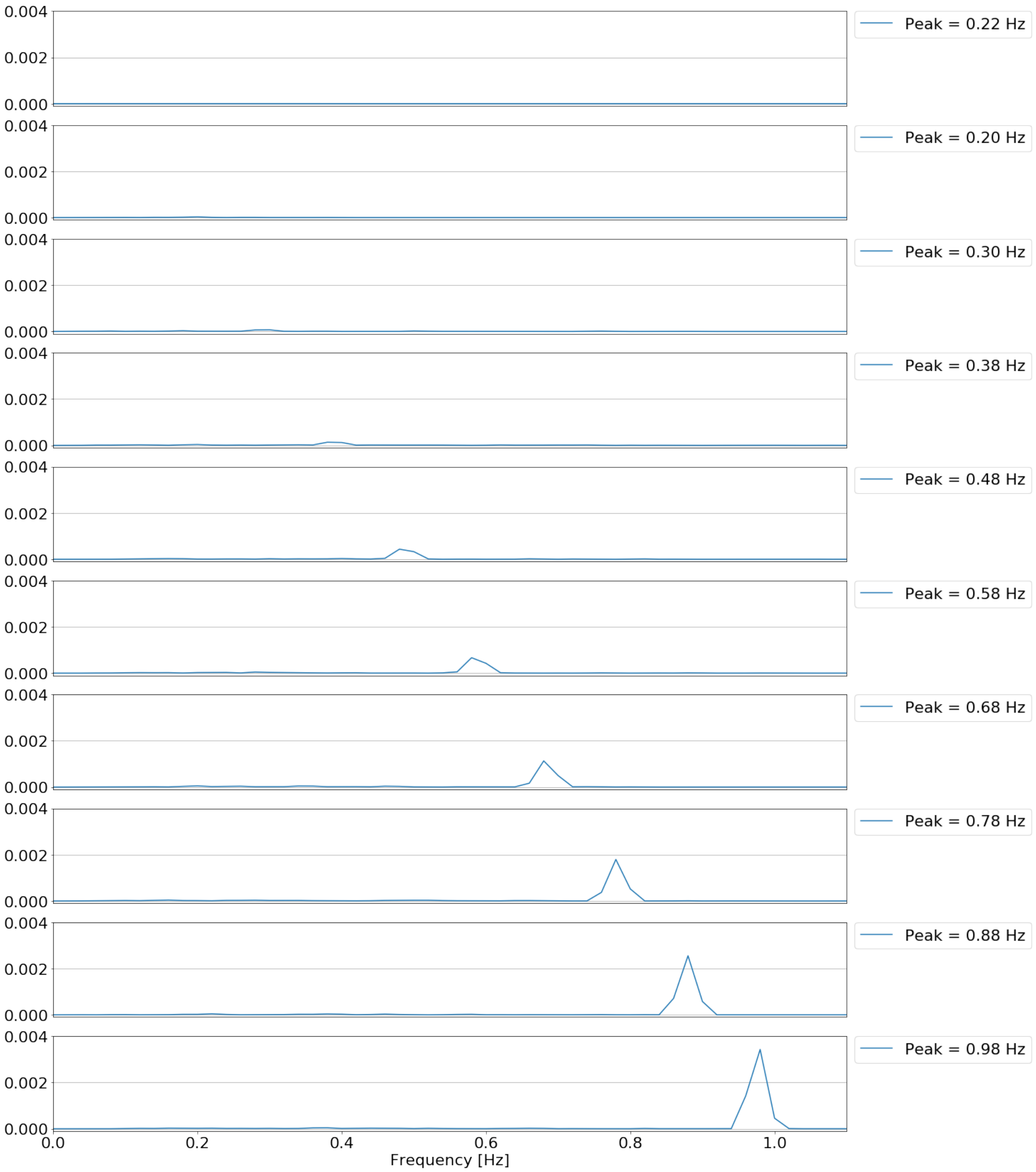

Figure 2.25: PSD computed from accelerations measured by the PCB Piezotronics accelerometer for frequencies between 0.2 Hz and 1.0 Hz

auto power spectrum, and average auto power spectrum. If any of these spectra were required to be computed in a manner different to the method used by the analyser software, this could not have been done in quasi-real-time as one would have to wait for the time history to be completely recorded on the laptop. On the contrary, with the iPhone and Raspberry Pi, some additional processing can be done on the accelerometer data in quasi-real-time without the need for additional hardware.

2.5 Summary

In this chapter, vessel stability was discussed and the metacentric height and roll period were identified as some of the means of assessing vessel stability. Table 2.11 shows a summary of vessel parameters and descriptions related to transverse stability.

Table 2.11: Summary of variables related to transverse stability

	Stable	**Unstable**
Centre of gravity	Low	High
Metacentric height	High	Low
Roll period less than beam	True	False
Returns to upright position	Quick	Slow
Stiff/Tender	Stiff	Tender
Level of comfort	Low	High

From the parameters shown in Table 2.11, the metacentric height and the roll period are typically used in assessing static stability using methods such as the inclining test and the roll period approximation as discussed in Section 2.1.3. Alternative means of stability assessment during operation including the Wolfson method and the SCraMP application, designed to be used by fishermen at sea were presented. These methods are targeted at monitoring dynamic instabilities by taking into consideration the operating conditions including the weather (significant wave height), the amount of load, and a vessel's motions. These are used to establish a safety index such as the traffic light system used by the Wolfson method, or the index used by the SCraMP application. Tools for measuring vessel motion were then discussed, including SBCs and IMUs, and optical motion camera systems.

The roll period test is usually suggested for small fishing vessels because it is easy to conduct, less expensive, not as technically demanding as the inclining test, and gives a quick and reasonably accurate estimate of vessel stability (Hudspeth et al., 2004). Even though the roll period test only provides an approximation of vessel stability, results obtained can be used to calculate the metacentric height of a vessel. In addition, it can be used to assess changes in the vessel's stability due to modifications made to the vessel. Based on this, this research aims to demonstrate that SBCs are a potential cost-effective solution for determining a vessel's roll period, which can be used at full-scale unlike solutions such as optical motion capture systems. The use of SBCs in determining the metacentric height from inclining tests are also demonstrated.

Chapter 3

Functional and technical requirements

In the previous chapter, we introduced the concept of vessel stability and concluded the chapter by focusing on demonstrating that SBCs are a potential cost-effective solution for determining a vessel's roll period and metacentric height. In this chapter, we will discuss the functional requirements for cost-effective technologies, and the hardware and software requirements for demonstrating that SBCs can be used to improve the assessment of vessel stability through the roll period test and the inclining test.

3.1 Functional requirements

In order for cost-effective technologies to improve upon the current method of using a stopwatch to measure the roll period three times and then taking the average, the following are the functional requirements for any solution:

- Accurate: For roll period measurement, the device should produce results more accurate than ± 0.2 seconds. 0.2 seconds is chosen as the benchmark because studies (Faux and Godolphin, 2019; Radner et al., 2017) show that this is the average reaction time of a timekeeper using a stopwatch
- Waterproof: The device should be sufficiently waterproof by having an ingress protection (IP) rating of at least IP65 due to the operating environment.
- Easy installation and calibration: The device should be easy to setup and not require a significant amount of time to install and calibrate
- Wireless communication: The device should have wireless communication capabilities to enable easy data transfer and control

- Full scale usage: The device should be capable of being used at full-scale and not only in a towing tank environment
- Additional information: Considering the device will cost more than a stopwatch the device should be capable of being used to provide more information such as the metacentric height and not only the roll period.

3.2 Hardware

The cost-effective technologies used in the remainder of this thesis are mainly the Raspberry Pi, a single-board computer (SBC), and the Navio2, a sensor board containing inertial measurement units (IMUs).

3.2.1 Raspberry Pi

The Raspberry Pi is a Single-Board Computer (SBC) which was initially created for educational purposes in 2012. Since the initial release there have been a number of versions, with each varying in features. In this thesis the Raspberry Pi 3 B+ was chosen. The Raspberry Pi was chosen because of its low cost (less than 50 USD) and strong user community. It is also quick to learn and is used as a learning tool in education (Ali et al., 2013). Similar to previous versions, it has a small form-factor measuring 85 mm x 56 mm x 16mm as shown in Figure 3.1. The Raspberry Pi 3B+ has a large number of peripherals and features (Mouser, 2019) including

- 2.4GHz and 5GHz IEEE 802.11.b/g/n/ac wireless LAN
- Bluetooth 4.2
- Gigabit Ethernet over USB 2.0
- Extended 40-pin GPIO header
- 4 USB 2.0 ports
- 4-pole stereo output and composite video port
- Micro SD port for loading operating system and data storage
- 5V/2.5A DC power input
- Broadcom BCM2837B0, Cortex-A53 (ARMv8) 64-bit SoC @ 1.4GHz
- 1GB LPDDR2 SDRAM
- 40 GPIO pins

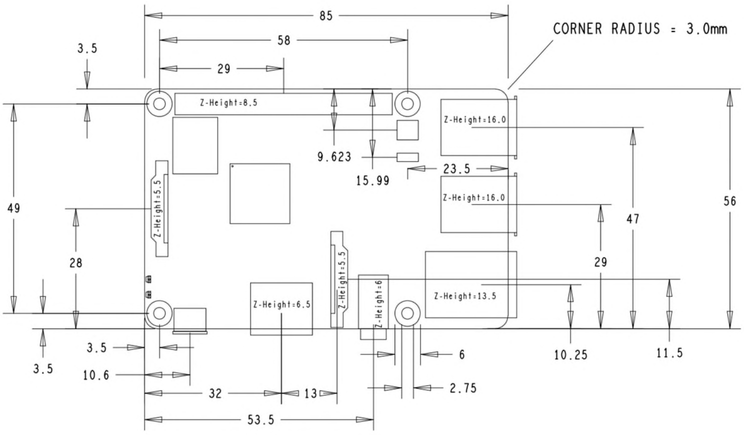

Figure 3.1: Raspberry Pi 3 Model B+ Dimensions. Adapted from *Adafruit Raspberry Pi 3 Model B+,* by Mouser (2019)

For the purposes of this thesis, one of the most important features of the Raspberry Pi are the 40 GPIO pins as these enable the Raspberry Pi to connect to external peripherals, in particular sensors via a number of protocols including serial peripheral interface (SPI), inter-integrated circuit (I2C), and universal asyncronous receiver/transmitter (UART). These pins are used to connect to the inertial measurement units on the Navio2 sensor discussed in the next section.

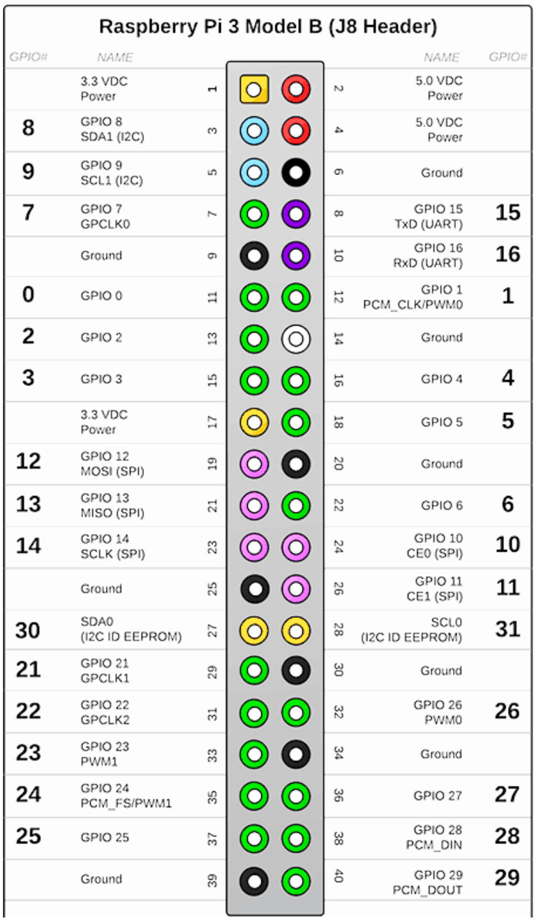

Raspberry Pi 3 Model B (J8 Header)

GPIO#	NAME			NAME	GPIO#
	3.3 VDC Power	1	2	5.0 VDC Power	
8	GPIO 8 SDA1 (I2C)	3	4	5.0 VDC Power	
9	GPIO 9 SCL1 (I2C)	5	6	Ground	
7	GPIO 7 GPCLK0	7	8	GPIO 15 TxD (UART)	15
	Ground	9	10	GPIO 16 RxD (UART)	16
0	GPIO 0	11	12	GPIO 1 PCM_CLK/PWM0	1
2	GPIO 2	13	14	Ground	
3	GPIO 3	15	16	GPIO 4	4
	3.3 VDC Power	17	18	GPIO 5	5
12	GPIO 12 MOSI (SPI)	19	20	Ground	
13	GPIO 13 MISO (SPI)	21	22	GPIO 6	6
14	GPIO 14 SCLK (SPI)	23	24	GPIO 10 CE0 (SPI)	10
	Ground	25	26	GPIO 11 CE1 (SPI)	11
30	SDA0 (I2C ID EEPROM)	27	28	SCL0 (I2C ID EEPROM)	31
21	GPIO 21 GPCLK1	29	30	Ground	
22	GPIO 22 GPCLK2	31	32	GPIO 26 PWM0	26
23	GPIO 23 PWM1	33	34	Ground	
24	GPIO 24 PCM_FS/PWM1	35	36	GPIO 27	27
25	GPIO 25	37	38	GPIO 28 PCM_DIN	28
	Ground	39	40	GPIO 29 PCM_DOUT	29

Figure 3.2: Raspberry Pi 3 pins. Adapted from *How to work with I2C Communication in Raspberry Pi,* by Igor (2018)

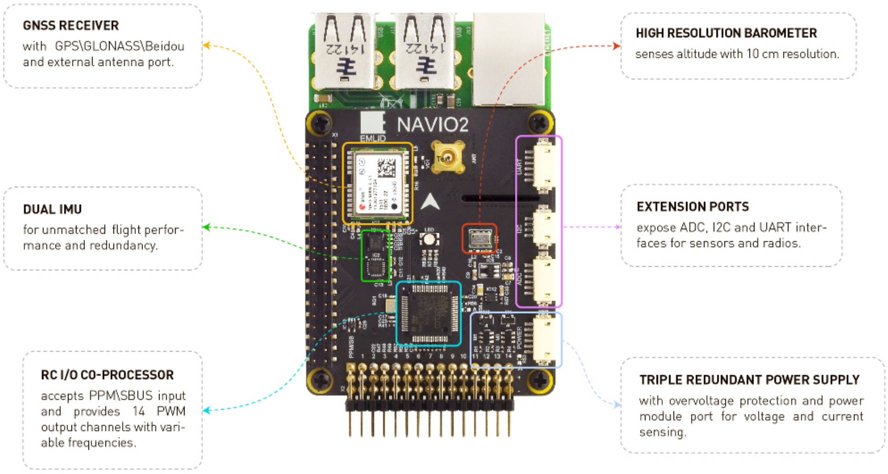

FIGURE 3.3: Navio2 parts

3.2.2 Navio2

The Raspberry Pi 3 was coupled with the Navio2 Autopilot Shield (Emlid, 2018) which has an MPU9250 9DOF IMU (InvenSense, 2016) and an LSM9DS1 9DOF IMU (ST Microelectronics, 2016). The Navio2 Shield was originally developed to be used as an autopilot system in drones and therefore has other features including a barometer, GPS, RC I/O co-processor and RGB LED as shown in Figure 3.3. The Navio2 Shield was chosen because it has 2 IMUs which can be used simultaneously for redundant measurements. Both these IMUs have specifications sufficient for measuring vessel motion (Abankwa et al., 2016). The results presented in the following chapters were from the MPU9250 9DOF IMU unless otherwise stated.

3.2.3 Additional hardware

The following is a list of hardware used in addition to the Raspberry Pi and Navio2 board.

- SD card: This stores the operating system and the data recorded during the roll tests. It should have sufficient storage capacity (64GB recommended)
- Raspberry Pi Real Time Clock (RTC): This device provides the Raspberry Pi with the correct time which is used in the rolling period test in combination with the roll amplitude to determine the roll period
- IP65 Waterproof case: This provides the device and power supply with protection against the operating conditions. A 125mm x 125mm x 100mm weatherproof junction box was used (Amazon, 2019b)
- Wireless USB adaptor: This extends the Wi-Fi range of the device. For this work, the Wi-Fi module had 2 requirements

  - It should work with the Raspberry Pi's operating system without the installation of additional drivers.
  - It should be capable of acting as an access point, allowing other device to connect to it via Wi-Fi.

  Based on the requirements, a Wi-Fi Adaptor with the Ralink RT3070 chipset was chosen (The Pi Hut, 2018)

- Portable battery: This provides power to the device. An Anker Powercore 10000mAh portable battery charger (Anker, 2019) capable of providing power for at least 8 hours continuously was used to power the device. This device was chosen because of its small size and weight relative to its power capacity.

3.2.4 Estimates of hardware cost

As shown in Table 3.1, the total cost of all hardware for a single unit of the proposed cost-effective technology is £247. Considering that full-scale deployment of this technology requires no changes to the hardware, this cost is significantly lower than other sensors deployed on vessels at full scale such as the XSens IMU which costs £800 (Farnell Element 4, 2016)

Table 3.1: Hardware costs

Hardware	**Cost (£)**
Raspberry Pi 3B+ (The Pi Hut, 2019)	34
Navio 2 (Emlid, 2018)	150
64 GB SD Card (Amazon, 2019a)	16
Raspberry Pi Real Time Clock (The Pi Hut, 2021)	6
IP65 waterproof case (Amazon, 2019b)	10
Wireless USB adaptor (The Pi Hut, 2018)	10
Portable battery (Anker, 2019)	21
Total	**247**

3.3 Software

Even though the technology being proposed in this thesis for use in assessing fishing vessel stability are low-cost off-the-shelf hardware, there a number of steps required to bring it all together for use. This chapter discusses the software setup methodology.

The Raspberry Pi acting as an access point, shown in Figure 3.4, which all other Raspberry Pis connect to is setup first. In order to do this a copy of the official operating system for the Raspberry Pi, Raspbian Jessie, downloaded from the Raspberry Pi website (RaspberryPi.org, 2019b) is installed on a 64 Gb SD card formatted to MS-DOS (FAT).

FIGURE 3.4: Access point

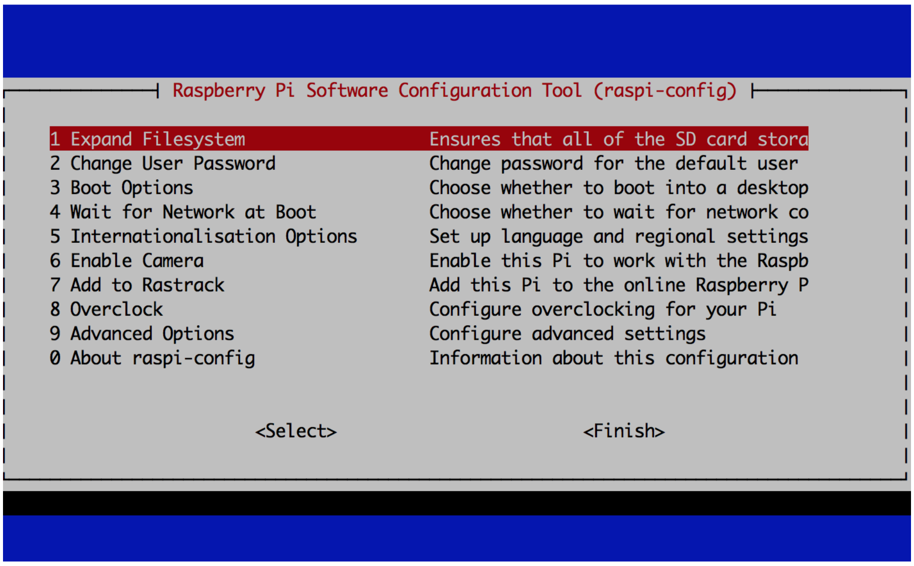

```
┤ Raspberry Pi Software Configuration Tool (raspi-config) ├

1 Expand Filesystem              Ensures that all of the SD card stora
2 Change User Password           Change password for the default user
3 Boot Options                   Choose whether to boot into a desktop
4 Wait for Network at Boot       Choose whether to wait for network co
5 Internationalisation Options   Set up language and regional settings
6 Enable Camera                  Enable this Pi to work with the Raspb
7 Add to Rastrack                Add this Pi to the online Raspberry P
8 Overclock                      Configure overclocking for your Pi
9 Advanced Options               Configure advanced settings
0 About raspi-config             Information about this configuration


              <Select>                      <Finish>
```

FIGURE 3.5: Raspberry Pi Configuration tool

The wireless USB adaptor and the Raspberry Pi clock are connected to the Raspberry Pi, the SD card with the installed operating system is inserted into the Raspberry Pi and powered up. The configuration graphical user interface (GUI) (Figure 3.5) is shown the first time the Raspberry Pi is booted up and can be accessed later by running the following from the command line:

```
sudo raspi-config
```

The configuration GUI is used to expand the filesystem to ensure that the root partition is resized to use the full SD card size. In addition, auto console login is enabled so that the Raspberry Pi automatically logs in the default user without requiring a password.

Next the date and time on the Raspberry Pi is set by running the following command from the command line.

```
sudo date -s 2019-06-16 10:50:00
```

This command sets the system time and not the time on the connected RTC. In order to transfer this time to the RTC the following command is run from the command line:

```
sudo hwclock -w
```

Afterwards the Raspberry Pi is set up as an access point in a standalone network to enable wireless communication via Wi-Fi (RaspberryPi.org, 2019a). This can be achieved manually by

- Installing the required software (DNSMasq and HOSTAPD)
- Configuring a static IP address using a configuration file
- Configuring the DHCP server
- Configuring the access point host software
- Adding routing

The Raspberry Pi used in combination with the Navio2 shield in assessing the roll period is set up in a similar manner. The Navio2 is attached to Raspberry Pi as shown in Figure 3.6.

The same operating system and initial configurations of expanding the filesystem and enabling auto console login are used. Afterwards, rather than configuring the Raspberry Pi to act as an access point, this Raspberry Pi is configured to automatically connect to the access point on the Raspberry Pi previously setup by editing the WPA supplicant file as shown below.

```
ctrl_interface=DIR=/var/run/wpa_supplicant GROUP=netdev
update_config=1
network={
    ssid="Name of Access Point"
    proto=WPA2
    key_mgmt=WPA-EAP
    eap=PEAP
    password= Access Point Password
    phase1="peaplabel=0"
    phase2="auth=MSCHAPV2"
```

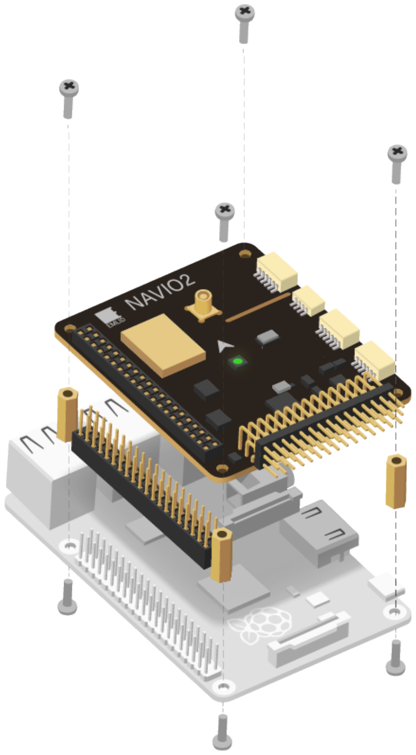

Figure 3.6: Attaching Navio2 to Raspberry Pi pins. Adapted from *Hardware setup,* by Emlid (2019b)

```
    priority=999
    disabled=0
    scan_ssid=0
    mode=0
    pairwise=CCMP TKIP
    proactive_key_caching=1
}
```

The final stage in this device setup is the code required to record the readings from the inertial measurement unit (IMU) on the Navio2. The code used in this thesis is based in a collection of drivers and examples for the Navio2 provided by the manufacturer under a BSD 3-Clause License (Emlid, 2019a).

FIGURE 3.7: Raspberry Pi coupled with the Navio2 and portable battery

3.4 Summary

This chapter presented the functional requirements for a device used in the following chapters to assess fishing vessel stability via the roll period test. It also presented a brief overview of the hardware used the steps required to setup the hardware. The following chapter assesses the ability of the low-cost devices to accurately determine a range of roll periods on a model vessel in a wave tank.

Chapter 4

Ability to detect changes in roll period

The previous chapter presented the functional requirements for a device used in assessing fishing vessel stability via the roll period test. This chapter aims to determine whether cost-effective technologies can be used to accurately detect changes in roll period within the accuracy requirement of ± 0.2 seconds. This is achieved by comparing the Raspberry Pi results for a range of roll periods against results from a potentiometer, a calibrated device traditionally used in towing tank tests.

4.1 Introduction

The rolling period test is a quick estimate of fishing vessel stability performed traditionally by inducing the vessel to roll freely and then timing the roll period using a stopwatch. The vessel has sufficient stability if the roll period in seconds is less than the vessel's breadth in metres. In order to improve upon this current method which determines the roll period using a stopwatch, in this chapter a model will be induced to roll using a pair of rotating weights for a range of roll periods. The accuracy of the computed roll period from cost-effecting technologies is then determined by comparing its results with results from a potentiometer. Even though only a single sensor is required to measure the vessel motion from which roll period is computed, four devices will be used to confirm that the location of the device on the vessel has no effect on the computed roll period and that results are consistent in cases where multiple devices are used.

4.2 Experimental Setup

The data collection process was conducted at the University of Southampton Bolderwood Campus towing tank (Figure 4.1). The tank is 138 m long, 6 m wide and 3.5 m deep, and has a wavemaker that can model sea states up to 0.7 m significant wave height (Figure 4.2).

Figure 4.1: University of Southampton Bolderwood Campus towing tank. Adapted from *Model basins,* by Wolfson Unit (2016)

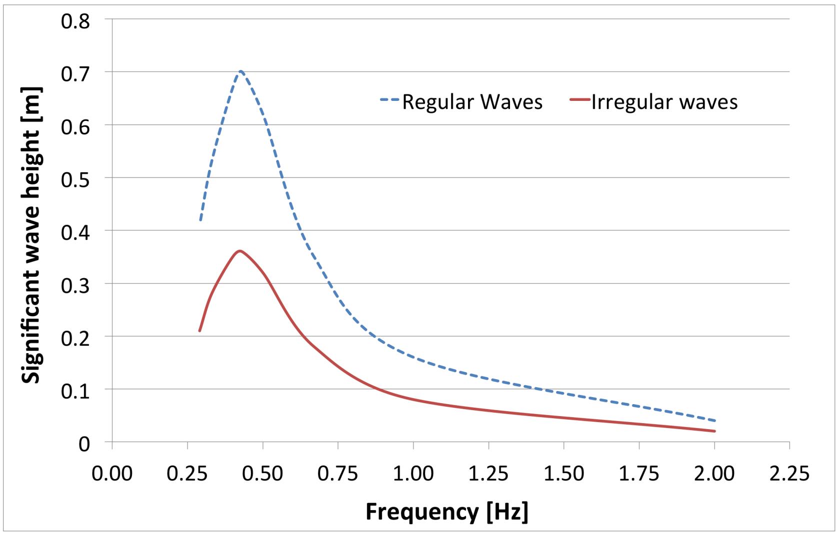

Figure 4.2: Bolderwood Campus towing tank wavemaker capability. Adapted from *Model basins,* by Wolfson Unit (2016)

4.2.1 Vessel model

The vessel used in this experiment is a scale model with the principal characteristics shown in Table 4.1.

Table 4.1: Vessel dimensions

Parameters	Ship	Model
Scale	1:1	1:15
Length (m)	31.575	2.105
Beam (m)	6.120	0.408
Depth (m)	3.900	0.260
Weight (kg)	57405.375	17.009

The data acquired from the model scale is converted into full-scale according to Froude scaling laws using the conversion factors shown in Table 4.2

Table 4.2: Froude Scaling Conversion Factors.
Adapted from *Data analysis methodologies for hydrodynamic experiments in waves,* by Islam et al. (2016)

Quantity	Unit	Scale factor
Acceleration	m/s^2	λ^0
Area	m^2	λ^2
Density	kg/m^3	λ^0
Force	N	λ^3
Frequency	s^{-1}	$\lambda^{-0.5}$
Length	m	λ^1
Mass	kg	λ^3
Moment	$N-m$	λ^4
Pressure	N/m^2	λ^1
Speed	m/s	$\lambda^{0.5}$
Time	s	$\lambda^{0.5}$

4.2.2 Hardware to induce and measure roll

In order to accurately induce and measure the required roll motion to assess the capability of cost-effective technologies in accurately determining a vessel's roll period, the following hardware shown in Figure 4.3 was used.

- National Instruments (NI) PX1-1036 chassis: This is a 6-slot chassis for housing modules which provides power, cooling and a communication bus for modular instruments/IO modules. Its price starts from £1,350. (National Instruments, 2019g). The modules are controlled with either an embedded controller or external PC. Within the NI PX1-1036 chassis there are

  - NI-PX1-8101 embedded controller: A portable PC based platform for industrial control, data acquisition, and test and measurement applications. It is equipped with 10/100/1000 BASE-TX (Gigabit) Ethernet with 2 high speed USB-ports. It also contains an integrated hard drive, serial port and other peripheral I/O (National Instruments, 2019f).
  - NI-PX1-6221 multifunction I/O module: An M-Series multifunction data acquisition unit with 16-bit analog input and 2 analog outputs. It has correlated digital input output with 2 32-bit counters with the ability to add sensor and high voltage measurement capability (National Instruments, 2019a).
  - NI-PX1-6704 analog output module: A 16-bit 32 channel analog output module used to create software-timed voltage and current output applications. It can independently set output voltage range on each channel and includes eight 5V TTL/CMOS digital lines. Its price starts from £1,920 (National Instruments, 2019b).
  - NI-PX1-7330 motion controller: A stepper motor motion controller used for fully programmable motion control for up to 4 independent or coordinated axes of motion. It contains a 32-bit CPU combined with digital signal processor (National Instruments, 2019d).

- NI MID-7602 motor drive: A 4/2 axis stepper motor drive serving as a complete power amplifier and system interface for use with four or two axes of simultaneous stepper motion control (National Instruments, 2019e).
- NI SCB-68 shielded I/O connector block for data acquisition devices with 68-Pin connector (National Instruments, 2019c).
- Bourns 6639S-1-502 precision potentiometer: High precision potentiometer for measuring roll motion.
- A pair of rotating weights connected to a motor to induce roll motion
- A towing post and heel fitting to attach the model to the towing carriage

Figure 4.3: Hardware to induce and measure roll motion on scale vessel in towing tank

4.2.3 Calibration

In order to determine the relationship between voltage and roll angle of the potentiometer, NI LabVIEW software is used to record the voltage angle at -25 degrees, -10 degrees, 0 degrees, +10 degrees and 25 degrees for at least 10 seconds

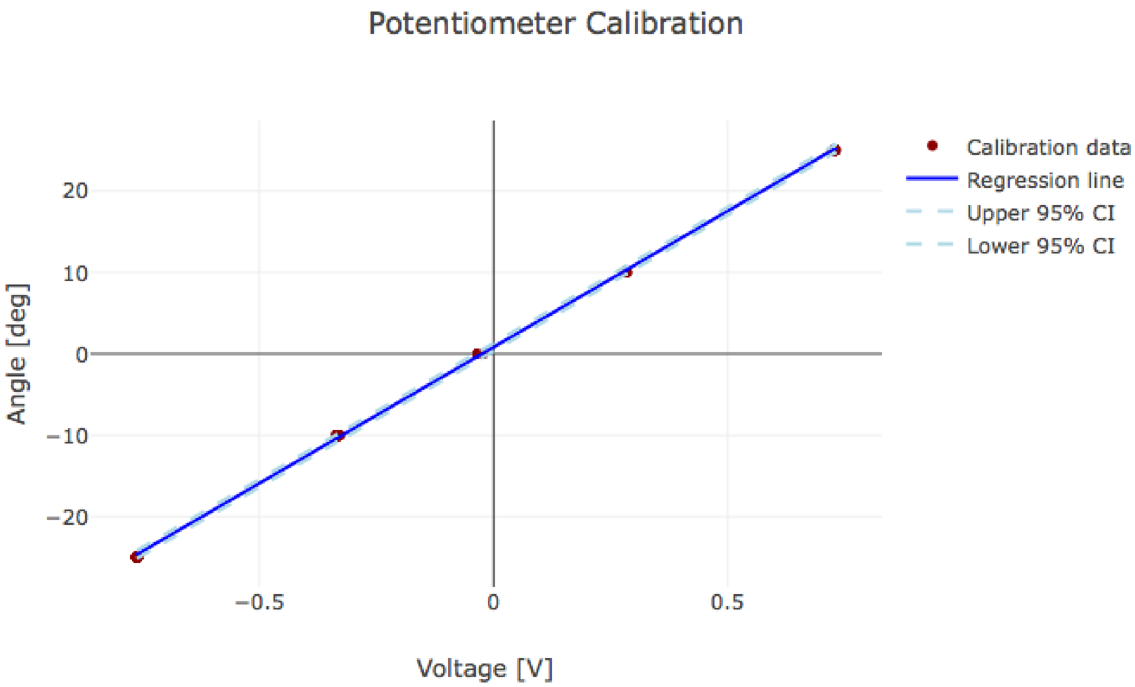

FIGURE 4.5: Potentiometer calibration

Using ordinary least square regression results of the recorded voltages shown in Figure 4.5, the relationship between the voltage and roll angle is determined as Equation 4.1.

$$\text{Roll angle} = 33.448 * \text{Voltage} + 0.808 \tag{4.1}$$

After the calibration readings are taken, the model vessel with the rotating weights to induce roll and the Raspberry Pis are attached are attached to the towing post as shown in Figure 4.4. Even though a single Raspberry Pi would be sufficient to measure the roll period, four are used to confirm that the location of the device on the vessel has no effect on the computed roll period and that results are consistent in cases where multiple devices are used.

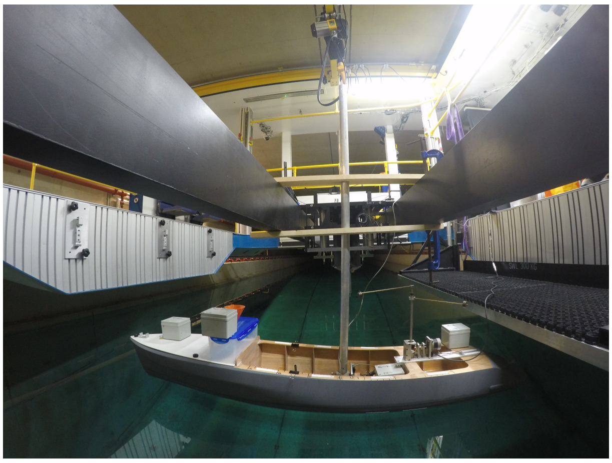

(A) Roll Setup - Side

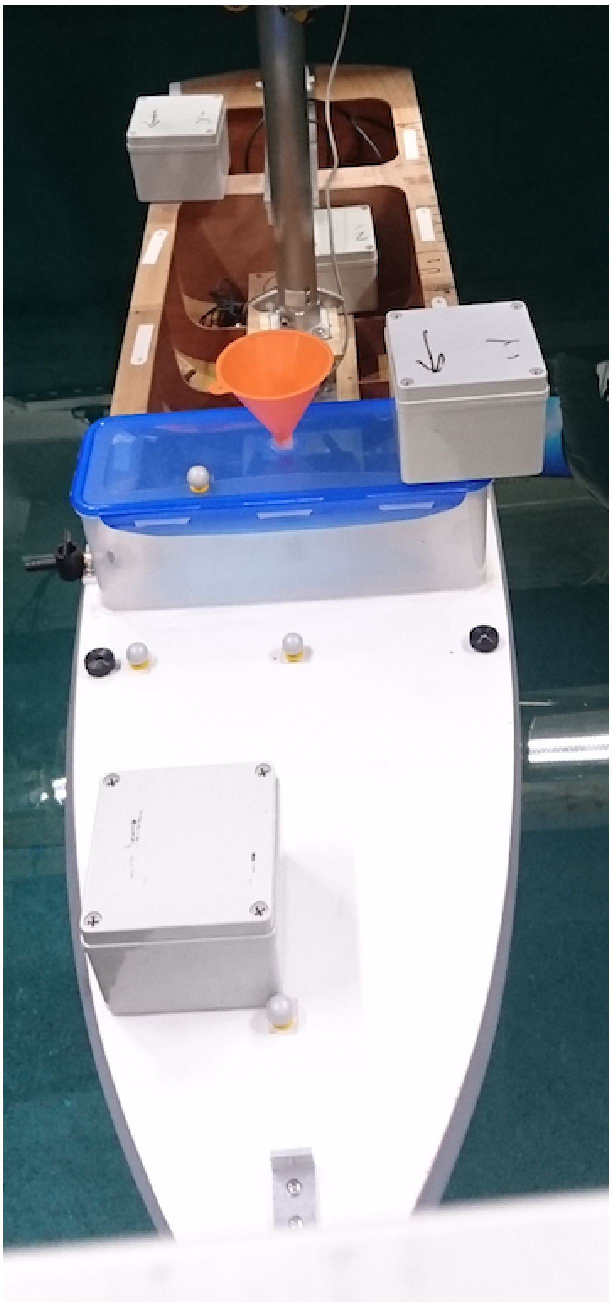

(B) Roll Setup - Front

Figure 4.4: Roll setup

4.3 Methodology

In order to determine the range of roll periods to be tested, scaling effects are considered. For the first 16 runs, full-scale roll periods between 5 and 20 seconds are used as this covers the range of typical roll periods for fishing vessels. The equivalent roll periods and frequencies for this range are shown in Table 4.3

Table 4.3: Full-scale and model roll periods and frequency

Run number	Up-scaled roll period (s)	Up-scaled roll frequency (Hz)	Model roll period (s)	Model roll frequency (Hz)
1	5.0	0.200	1.291	0.775
2	6.0	0.167	1.549	0.645
3	7.0	0.143	1.807	0.553
4	8.0	0.125	2.066	0.484
5	9.0	0.111	2.324	0.430
6	10.0	0.100	2.582	0.387
7	11.0	0.091	2.840	0.352
8	12.0	0.083	3.098	0.323
9	13.0	0.077	3.357	0.298
10	14.0	0.071	3.615	0.277
11	15.0	0.067	3.873	0.258
12	16.0	0.062	4.131	0.242
13	17.0	0.059	4.389	0.228
14	18.0	0.056	4.648	0.215
15	19.0	0.053	4.906	0.204
16	20.0	0.050	5.164	0.194

Six additional experimental runs are also conducted to determine how the Raspberry Pis perform when actually measuring the higher roll periods expected for the full-scale vessel. The equivalent roll periods and frequencies for this range are shown in Table 4.4.

TABLE 4.4: Full-scale and model roll periods and frequencies for additional runs

Run number	Up-scaled roll period (s)	Up-scaled roll frequency (Hz)	Model roll period (s)	Model roll frequency (Hz)
17	22.782	0.044	5.882	0.17
18	25.820	0.039	6.667	0.15
19	29.792	0.034	7.692	0.13
20	35.209	0.028	9.091	0.11
21	43.033	0.023	11.111	0.09
22	55.328	0.018	14.286	0.07
23	77.460	0.013	20.000	0.05

In order to ensure that roll motion measurements can be used to accurately detect roll period differences with an accuracy of more than ± 0.2 seconds, the minimum sample times shown in Table 4.5 are calculated using Equation 4.2.

$$\Delta f = \frac{f_s}{N} = \frac{f_s}{f_s \cdot t} = \frac{1}{t} \tag{4.2}$$

Table 4.5, visualised in Figure 4.6 shows that the minimum sample time required to maintain a resolution of 0.2 seconds increases exponentially as the roll period being measured increases. This is not expected to eliminate cost-effective technologies as a feasible solution for determining roll period because suggestions by the International Maritime Organization (IMO) et al. (2012) and other studies (Rojas et al., 2003) show that the maximum roll period for vessels of the length this is targeted at (less than 15m) is approximately 6 seconds.

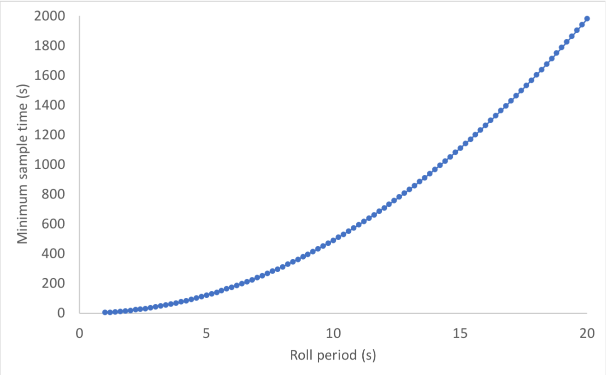

FIGURE 4.6: Exponentially increasing sample time as roll period increases

Table 4.5: Minimum sample time required for a resolution of 0.2 seconds at increasing roll periods

Model roll period (s)	Model roll frequency (Hz)	Model roll frequency difference (Hz)	Minimum sample time (s)
1.0	1.0000	-0.2500	4.0
1.2	0.8333	-0.1667	6.0
1.4	0.7143	-0.1190	8.4
1.6	0.6250	-0.0893	11.2
1.8	0.5556	-0.0694	14.4
2.0	0.5000	-0.0556	18.0
2.2	0.4545	-0.0455	22.0
2.4	0.4167	-0.0379	26.4
2.6	0.3846	-0.0321	31.2
2.8	0.3571	-0.0275	36.4
3.0	0.3333	-0.0238	42.0
3.2	0.3125	-0.0208	48.0
3.4	0.2941	-0.0184	54.4
3.6	0.2778	-0.0163	61.2
3.8	0.2632	-0.0146	68.4
4.0	0.2500	-0.0132	76.0
4.2	0.2381	-0.0119	84.0
4.4	0.2273	-0.0108	92.4
4.6	0.2174	-0.0099	101.2
4.8	0.2083	-0.0091	110.4
5.0	0.2000	-0.0083	120.0
5.2	0.1923	-0.0077	130.0

4.4 Results

Before presenting the results from all 23 runs, the last run is used to illustrate how the roll period is calculated from the recorded time series. Roll angles from the Raspberry Pi are computed using readings from both the accelerometer and gyroscope. Therefore, when calculating the roll period either the raw accelerometer and gyroscope readings shown in Figure 4.7 or the roll angle computed from the accelerometer and gyroscope shown in Figure 4.8 can be used.

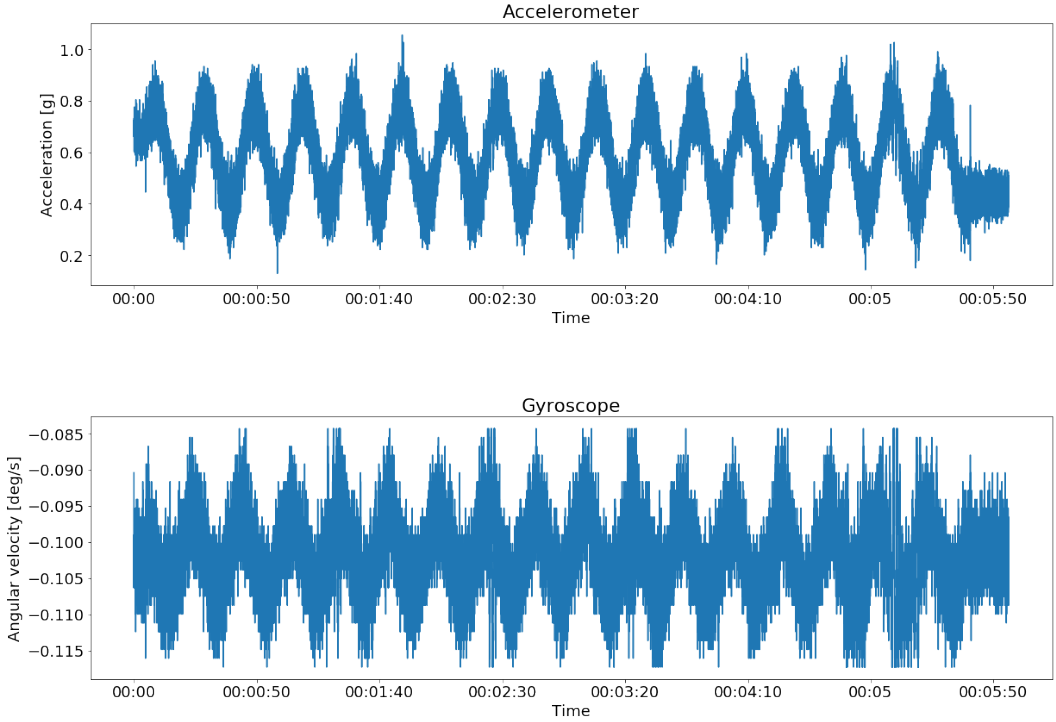

Figure 4.7: Raw accelerometer and gyroscope readings for Run 23 (0.05Hz motion)

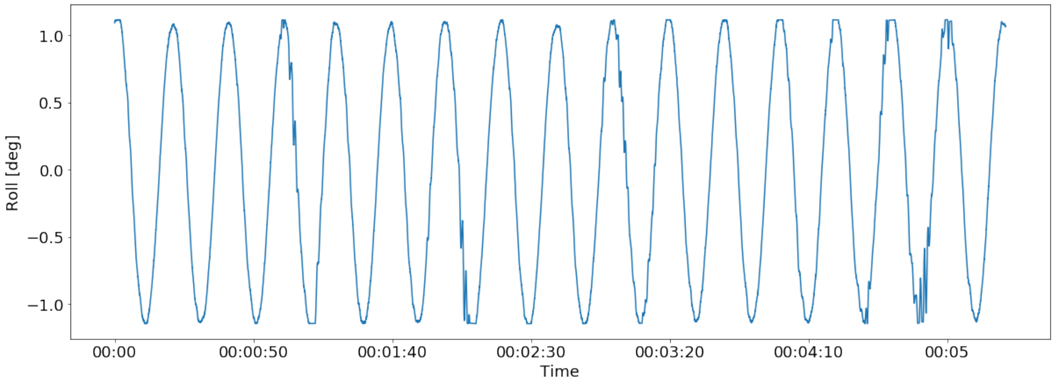

Figure 4.8: Roll angle readings for Run 23 (0.05Hz motion)

Before any of the time series data were analysed, a second-order low-pass Butterworth filter was used to eliminate any frequencies higher than 1.5 Hz. The Butterworth filter was used as this filter has been found to be the most appropriate for filtering noise and preserving motion (Gelin, 2013). Figure 4.9 and Figure 4.10 show the time series for Run 23 after the low pass filter was applied.

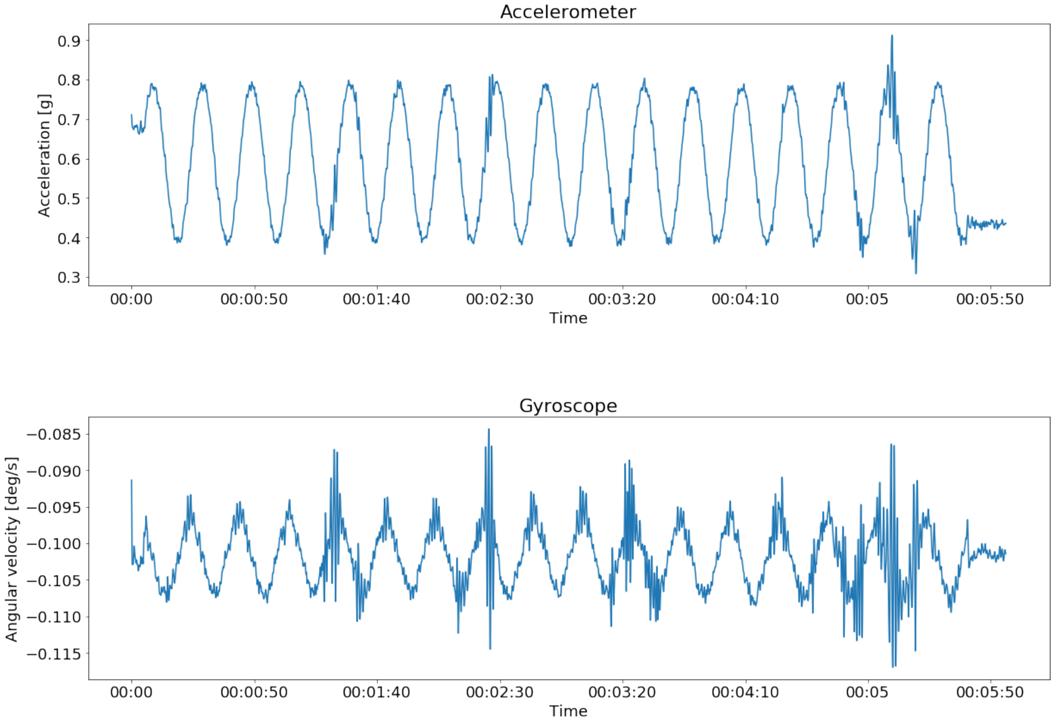

FIGURE 4.9: Filtered accelerometer and gyroscope readings for Run 23 (0.05Hz motion)

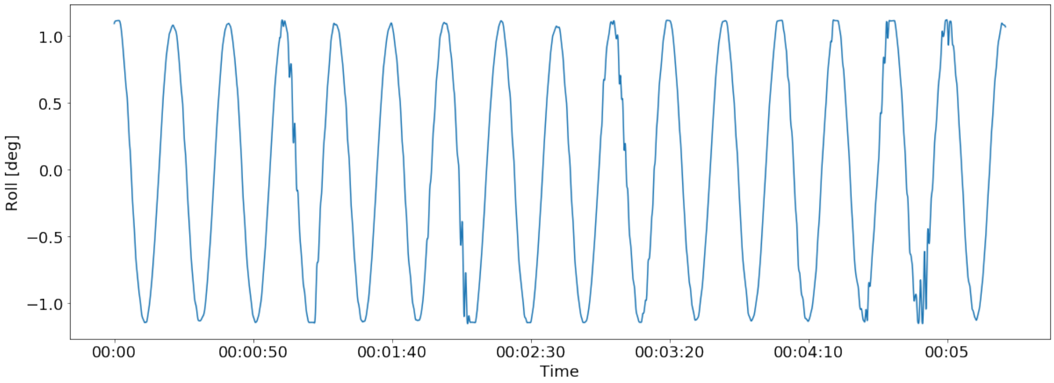

FIGURE 4.10: Filtered roll angle readings for Run 23 (0.05Hz motion)

After the low pass filter is applied, Welch's method (described in Section 2.3) is used to compute the spectra for each of the 3 time series as shown in Figure 4.11 and Figure 4.12. From these figures the peak frequencies were determined as the maximum frequencies in the spectra. The peak frequencies for all the runs determined from the 4 devices and the potentiometer are shown in Table 4.6. Once the peak frequencies were determined, the corresponding roll periods were calculated by taking the inverse of the frequencies as seen in Table 4.7.

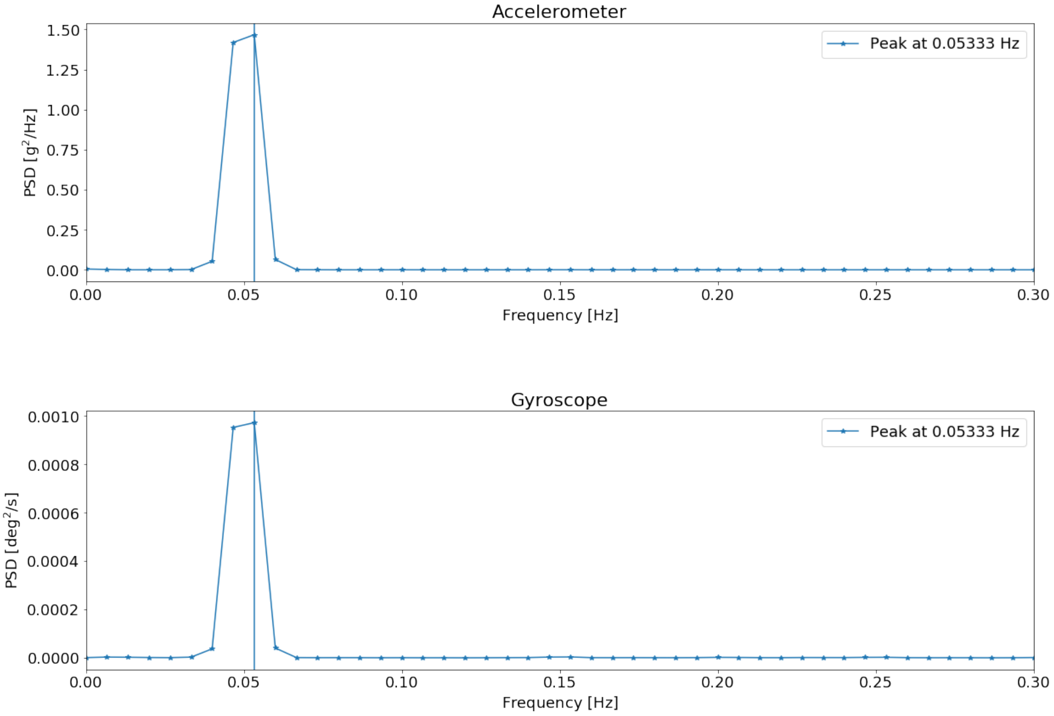

Figure 4.11: Power spectral density calculated from accelerometer and gyroscope readings

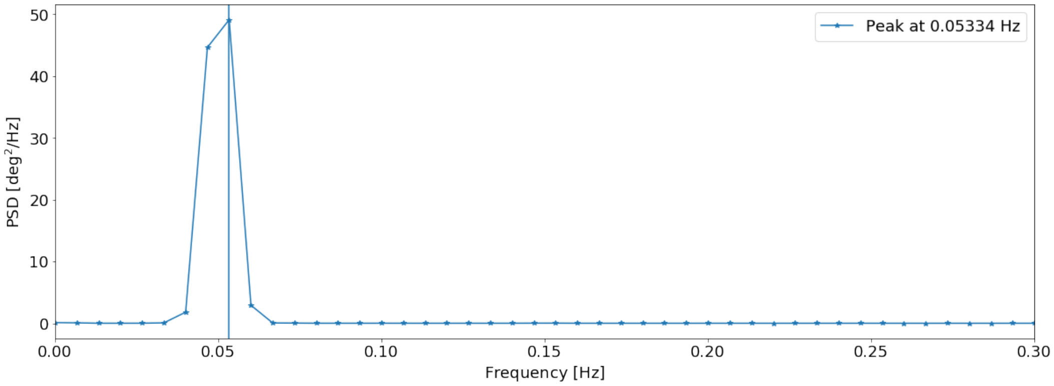

Figure 4.12: Power spectral density calculated from roll angle

In addition to the roll period, the roll amplitudes were also recorded for the runs as shown in Table 4.8. These were computed as half the difference between the maximum and the minimum roll angle.

Table 4.6: Peak frequencies (Hz) computed from spectra

Run number	Navio - 1	Navio - 2	Navio - 3	Navio - 4	Navio - Average	Potentiometer
1	0.77	0.73	0.77	0.77	0.76	0.77
2	0.65	0.61	0.65	0.65	0.64	0.65
3	0.56	0.53	0.53	0.56	0.54	0.56
4	0.48	0.48	0.49	0.47	0.48	0.48
5	0.45	0.43	0.43	0.43	0.43	0.43
6	0.38	0.40	0.38	0.38	0.39	0.39
7	0.35	0.33	0.35	0.35	0.35	0.35
8	0.32	0.32	0.32	0.32	0.32	0.32
9	0.28	0.29	0.30	0.30	0.30	0.30
10	0.27	0.28	0.28	0.28	0.28	0.28
11	0.26	0.25	0.26	0.25	0.26	0.26
12	0.24	0.25	0.25	0.21	0.24	0.24
13	0.22	0.23	0.23	0.23	0.23	0.22
14	0.22	0.22	0.22	0.22	0.22	0.21
15	0.20	0.21	0.20	0.21	0.21	0.20
16	0.19	0.19	0.19	0.19	0.19	0.19
17	0.17	0.17	0.17	0.17	0.17	0.17
18	0.15	0.15	0.15	0.15	0.15	0.15
19	0.13	0.13	0.13	0.13	0.13	0.13
20	0.11	0.11	0.11	0.11	0.11	0.11
21	0.09	0.09	0.09	0.09	0.09	0.09
22	0.07	0.07	0.07	0.07	0.07	0.07
23	0.05	0.05	0.05	0.05	0.05	0.05

Table 4.7: Roll periods (s) computed from peak frequencies

Run number	Navio - 1	Navio - 2	Navio - 3	Navio - 4	Navio - Average	Potentiometer
1	1.30	1.37	1.30	1.30	1.32	1.30
2	1.54	1.64	1.54	1.54	1.56	1.54
3	1.79	1.89	1.89	1.79	1.85	1.79
4	2.08	2.08	2.04	2.13	2.08	2.08
5	2.22	2.33	2.33	2.33	2.33	2.33
6	2.63	2.50	2.63	2.63	2.56	2.56
7	2.86	3.03	2.86	2.86	2.86	2.86
8	3.12	3.12	3.12	3.12	3.12	3.12
9	3.57	3.45	3.33	3.33	3.33	3.33
10	3.70	3.57	3.57	3.57	3.57	3.57
11	3.85	4.00	3.85	4.00	3.85	3.85
12	4.17	4.00	4.00	4.76	4.17	4.17
13	4.55	4.35	4.35	4.35	4.35	4.55
14	4.55	4.55	4.55	4.55	4.55	4.76
15	5.00	4.76	5.00	4.76	4.76	5.00
16	5.26	5.26	5.26	5.26	5.26	5.26
17	5.88	5.88	5.88	5.88	5.88	5.88
18	6.67	6.67	6.67	6.67	6.67	6.67
19	7.69	7.69	7.69	7.69	7.69	7.69
20	9.09	9.09	9.09	9.09	9.09	9.09
21	11.11	11.11	11.11	11.11	11.11	11.11
22	14.29	14.29	14.29	14.29	14.29	14.29
23	20.00	20.00	20.00	20.00	20.00	20.00

Table 4.8: Roll amplitudes (deg)

Run number	Navio - 1	Navio - 2	Navio - 3	Navio - 4	Navio - Average	Potentiometer
1	13.22	13.68	13.01	12.99	13.23	14.83
2	5.91	6.07	5.49	5.86	5.83	7.29
3	3.34	3.48	3.21	3.32	3.34	3.71
4	2.62	2.66	2.55	2.64	2.62	3.05
5	2.10	2.09	2.02	2.05	2.07	2.34
6	1.81	1.81	1.75	1.78	1.79	1.99
7	1.63	1.65	1.58	1.60	1.61	1.61
8	1.61	1.66	1.52	1.57	1.59	1.59
9	1.60	1.49	1.49	1.46	1.51	1.48
10	1.61	1.54	1.48	1.35	1.49	1.52
11	1.34	1.33	1.28	1.31	1.31	1.34
12	1.33	1.31	1.27	1.29	1.30	1.33
13	1.34	1.33	1.30	1.32	1.32	1.36
14	1.36	1.33	1.29	1.31	1.32	1.39
15	1.28	1.27	1.25	1.28	1.27	1.37
16	1.22	1.19	1.18	1.23	1.21	1.27
17	1.24	1.21	1.19	1.16	1.20	1.19
18	1.20	1.16	1.15	1.17	1.17	1.15
19	1.19	1.14	1.14	1.16	1.16	1.14
20	1.16	1.10	1.11	1.13	1.13	1.14
21	1.16	1.10	1.11	1.12	1.12	1.11
22	1.14	1.09	1.10	1.11	1.11	1.11
23	1.15	1.12	1.16	1.12	1.14	1.15

4.5 Discussion

The results show that there is no significant difference in peak frequencies computed from the Raspberry Pis and peak frequencies computed by the potentiometer. Across all 23 runs and all 4 devices the maximum difference in peak frequencies computed by the Raspberry Pis and the potentiometer is 0.04 Hz as shown in Table 4.9. The average difference between the Raspberry Pis and the potentiometer is 0.00152 Hz with a standard deviation of 0.00988 Hz. For roll period differences between the Raspberry Pis and the potentiometer, shown in Table 4.10, the average is 0.00315 seconds with a standard deviation of 0.10677 seconds. For roll amplitude differences between the Raspberry Pis and the potentiometer, shown in Table 4.11, the average is 0.201 degrees with a standard deviation of 0.437 degrees.

The results suggest that cost-effective computing technologies can be used to accurately detect the roll period of a vessel. In addition, roll period results obtained using these technologies have an accuracy higher than the benchmark of 0.2 seconds, which is the uncertainty associated with a timekeeper using a stopwatch. In addition to roll period measurements the Raspberry Pis can also be used to provide information on a vessel's roll amplitude, which the use of only a stopwatch in traditional roll period tests do not currently provide. This is important because roll period tests in which vessels roll too much produce invalid results. Traditionally this has been achieved by temporarily marking the vessel hull amidship at a distance above the waterline and ensuring this mark does not go below the water. Knowledge of the exact amplitude of roll provided by cost-effective technologies will provide operators with additional information useful in making decisions on the validity of roll period tests.

Table 4.9: Difference in peak frequencies (Hz) computed by Raspberry Pis and potentiometer

Run number	Navio - 1	Navio - 2	Navio - 3	Navio - 4	Navio - Average
1	0.00	0.04	0.00	0.00	0.01
2	0.00	0.04	0.00	0.00	0.01
3	0.00	0.03	0.03	0.00	0.02
4	0.00	0.00	-0.01	0.01	0.00
5	-0.02	0.00	0.00	0.00	0.00
6	0.01	-0.01	0.01	0.01	0.00
7	0.00	0.02	0.00	0.00	0.00
8	0.00	0.00	0.00	0.00	0.00
9	0.02	0.01	0.00	0.00	0.00
10	0.01	0.00	0.00	0.00	0.00
11	0.00	0.01	0.00	0.01	0.00
12	0.00	-0.01	-0.01	0.03	0.00
13	0.00	-0.01	-0.01	-0.01	-0.01
14	-0.01	-0.01	-0.01	-0.01	-0.01
15	0.00	-0.01	0.00	-0.01	-0.01
16	0.00	0.00	0.00	0.00	0.00
17	0.00	0.00	0.00	0.00	0.00
18	0.00	0.00	0.00	0.00	0.00
19	0.00	0.00	0.00	0.00	0.00
20	0.00	0.00	0.00	0.00	0.00
21	0.00	0.00	0.00	0.00	0.00
22	0.00	0.00	0.00	0.00	0.00
23	0.00	0.00	0.00	0.00	0.00

Table 4.10: Difference in roll periods (s) computed by Raspberry Pis and potentiometer

Run number	Navio - 1	Navio - 2	Navio - 3	Navio - 4	Navio - Average
1	0.00	-0.07	0.00	0.00	-0.02
2	0.00	-0.10	0.00	0.00	-0.02
3	0.00	-0.10	-0.10	0.00	-0.06
4	0.00	0.00	0.04	-0.05	0.00
5	0.11	0.00	0.00	0.00	0.00
6	-0.07	0.06	-0.07	-0.07	0.00
7	0.00	-0.17	0.00	0.00	0.00
8	0.00	0.00	0.00	0.00	0.00
9	-0.24	-0.12	0.00	0.00	0.00
10	-0.13	0.00	0.00	0.00	0.00
11	0.00	-0.15	0.00	-0.15	0.00
12	0.00	0.17	0.17	-0.59	0.00
13	0.00	0.20	0.20	0.20	0.20
14	0.21	0.21	0.21	0.21	0.21
15	0.00	0.24	0.00	0.24	0.24
16	0.00	0.00	0.00	0.00	0.00
17	0.00	0.00	0.00	0.00	0.00
18	0.00	0.00	0.00	0.00	0.00
19	0.00	0.00	0.00	0.00	0.00
20	0.00	0.00	0.00	0.00	0.00
21	0.00	0.00	0.00	0.00	0.00
22	0.00	0.00	0.00	0.00	0.00
23	0.00	0.00	0.00	0.00	0.00

Table 4.11: Difference in roll amplitudes (deg) from Raspberry Pis and potentiometer

Run number	Navio - 1	Navio - 2	Navio - 3	Navio - 4	Navio - Average
1	1.61	1.15	1.82	1.84	1.60
2	1.38	1.22	1.80	1.43	1.46
3	0.37	0.23	0.50	0.39	0.37
4	0.43	0.39	0.50	0.41	0.43
5	0.24	0.25	0.32	0.29	0.27
6	0.18	0.18	0.24	0.21	0.20
7	-0.02	-0.04	0.03	0.01	0.00
8	-0.02	-0.07	0.07	0.02	0.00
9	-0.12	-0.01	-0.01	0.02	-0.03
10	-0.09	-0.02	0.04	0.17	0.03
11	0.00	0.01	0.06	0.03	0.03
12	0.00	0.02	0.06	0.04	0.03
13	0.02	0.03	0.06	0.04	0.04
14	0.03	0.06	0.10	0.08	0.07
15	0.09	0.10	0.12	0.09	0.10
16	0.05	0.08	0.09	0.04	0.06
17	-0.05	-0.02	0.00	0.03	-0.01
18	-0.05	-0.01	0.00	-0.02	-0.02
19	-0.05	0.00	0.00	-0.02	-0.02
20	-0.02	0.04	0.03	0.01	0.01
21	-0.05	0.01	0.00	-0.01	-0.01
22	-0.03	0.02	0.01	0.00	0.00
23	0.00	0.03	-0.01	0.03	0.01
Average	0.17	0.16	0.25	0.22	0.20

4.6 Summary

This chapter assessed the ability of cost-effective computing technologies in accurately determining a range of roll periods and compared the results with results obtained from a potentiometer. The results show that these cost-effective technologies can be used to accurately determine the roll period of a vessel. Another advantage of conducting the roll period tests with the cost-effective technologies over the traditional method of using a stopwatch or the potentiometer are that the cost-effective technologies can also provide information on the vessel roll amplitude which the stopwatch cannot, and can be used in assessing the stability of a full-scale vessel, which the potentiometer cannot.

In the next chapter we will examine the ability of these cost-effective technologies in determining changes on a vessel due to a weight shifting vertically in terms of both roll period and roll amplitude.

Chapter 5

Ability to detect vertical weight shifts in waves

The previous chapter demonstrated that cost-effective technologies can be used to accurately determine a vessel's roll period and provide additional information on roll amplitude. This chapter will examine how both of these variables change in response to weights being moved vertically when the vessel is in waves.

5.1 Introduction

The movements of weights vertically on a vessel are a problem particularly relevant to fishing vessels because of the nature of vessel operations. Catch can be lifted above the deck (high height), can be placed on the deck (medium height) or placed in storage below deck (low height). The vertical position of weights onboard the vessel affects the vessel stability as it changes the height of the vessel's centre of gravity, in turn changing the metacentric height. The previous chapter showed that cost-effective technologies can be used to provide an indication of a vessel's stability before operation through the roll test, and also provide information on the vessel's roll amplitude. This chapter aims to demonstrate whether the same methodology applied in the previous chapter can be used detect changes in a vessel's stability as the vessel operates in waves.

5.2 Methodology

The same model vessel and towing tank used in the previous chapter are used in this chapter. The difference in methodology from the previous chapter is that rather than inducing the vessel to roll using rotating weights, the vessel rolls in waves generated using the wave maker with amplitudes of 0.06 metres and a wave frequency of 0.6 Hz. The runs examine the effect of placing three weights (1N, 5N, 10N) and three different vertical positions on the vessel (low, medium, high). The low position is at the bottom of the vessel with the medium and high positions being 0.130 m and 0.219 m above the low position respectively. On the full-scale vessel, these weight movements are equivalent to vertically moving weights of 337.5 kg, 1687.5 kg, and 3375.0 kg upwards by 1.950 m (medium) and 3.285 m (high)

5.3 Results

Similar to the results in the previous chapter the roll periods are computed by first applying a low-pass filter to the raw time-series, and computing the spectra using Welch's method. Once this is done the roll periods shown in Table 5.2 are computed as the inverse of the maximum roll frequencies shown in the Table 5.1. In addition to the roll period, the roll amplitudes were also recorded for the runs as shown in Table 5.3. These were computed as half difference between the maximum and the minimum roll angle.

Table 5.1: Peak frequencies (Hz) computed from spectra

Run Number	Weight [N]	Vertical Position	Navio 1	Navio 2	Navio 3	Navio 4	Navio Average	Potentiometer
1.0	1.0	Low	0.60	0.60	0.61	0.59	0.60	0.60
2.0	1.0	Medium	0.60	0.60	0.60	0.60	0.60	0.61
3.0	1.0	High	0.61	0.60	0.60	0.61	0.60	0.60
4.0	5.0	Low	0.59	0.60	0.60	0.61	0.60	0.60
5.0	5.0	Medium	0.59	0.61	0.60	0.61	0.60	0.60
6.0	5.0	High	0.61	0.61	0.60	0.61	0.61	0.60
7.0	10.0	Low	0.60	0.60	0.60	0.60	0.60	0.60
8.0	10.0	Medium	0.61	0.60	0.61	0.60	0.60	0.60
9.0	10.0	High	0.61	0.60	0.60	0.60	0.60	0.60

Table 5.2: Roll periods (s) computed from peak frequencies

Run Number	Weight [N]	Vertical Position	Navio 1	Navio 2	Navio 3	Navio 4	Navio Average	Potentiometer
1.0	1.0	Low	1.67	1.67	1.64	1.69	1.67	1.67
2.0	1.0	Medium	1.67	1.67	1.67	1.67	1.67	1.64
3.0	1.0	High	1.64	1.67	1.67	1.64	1.67	1.67
4.0	5.0	Low	1.69	1.67	1.67	1.64	1.67	1.67
5.0	5.0	Medium	1.69	1.64	1.67	1.64	1.67	1.67
6.0	5.0	High	1.64	1.64	1.67	1.64	1.64	1.67
7.0	10.0	Low	1.67	1.67	1.67	1.67	1.67	1.67
8.0	10.0	Medium	1.64	1.67	1.64	1.67	1.67	1.67
9.0	10.0	High	1.64	1.67	1.67	1.67	1.67	1.67

5.4 Discussion

The results show that there is no significant difference in peak frequencies computed from the Raspberry Pis and peak frequencies computed by the potentiometer as seen in the previous

Table 5.3: Roll amplitudes (deg)

Run Number	Weight [N]	Vertical Position	Navio 1	Navio 2	Navio 3	Navio 4	Navio Average	Potentiometer
1.0	1.0	Low	2.75	2.78	2.75	2.82	2.78	3.46
2.0	1.0	Medium	3.43	3.45	3.32	3.36	3.39	4.08
3.0	1.0	High	4.34	4.37	4.29	4.30	4.32	5.04
4.0	5.0	Low	3.40	3.32	3.26	3.28	3.31	3.99
5.0	5.0	Medium	3.52	3.54	3.45	3.52	3.51	4.16
6.0	5.0	High	4.59	4.58	4.53	4.57	4.57	5.20
7.0	10.0	Low	3.28	3.34	3.26	3.37	3.31	3.90
8.0	10.0	Medium	5.14	5.11	5.11	5.19	5.14	5.58
9.0	10.0	High	6.77	6.89	6.66	6.99	6.83	7.24

chapter. Across all runs and all 4 devices the maximum difference in peak frequency computed by the Raspberry Pis and the potentiometer is 0.01 Hz as shown in Table 5.4. The average difference between the Raspberry Pis and the potentiometer is -0.00138 Hz with a standard deviation of 0.00713 Hz. For roll period differences between the Raspberry Pis and the potentiometer, shown in Table 5.5, the average is 0.00499 seconds with a standard deviation of 0.020 seconds. For roll amplitude differences between the Raspberry Pis and the potentiometer, shown in Table 5.6, the average is 0.610 degrees with a standard deviation of 0.118 degrees.

The results in this chapter again suggest that cost-effective computing technologies can be used to accurately detect the roll period of a vessel and that results obtained using these technologies have an accuracy higher than the benchmark of 0.2 seconds.

Table 5.4: Difference in peak frequencies (Hz) computed by Raspberry Pis and potentiometer

Run Number	Weight [N]	Vertical Position	Navio 1	Navio 2	Navio 3	Navio 4	Navio Average
1.0	1.00	Low	0.00	0.00	-0.01	0.01	0.00
2.0	1.00	Medium	0.01	0.01	0.01	0.01	0.01
3.0	1.00	High	-0.01	0.00	0.00	-0.01	0.00
4.0	5.00	Low	0.01	0.00	0.00	-0.01	0.00
5.0	5.00	Medium	0.01	-0.01	0.00	-0.01	0.00
6.0	5.00	High	-0.01	-0.01	0.00	-0.01	-0.01
7.0	10.00	Low	0.00	0.00	0.00	0.00	0.00
8.0	10.00	Medium	-0.01	0.00	-0.01	0.00	0.00
9.0	10.00	High	-0.01	0.00	0.00	0.00	0.00
Average	-	-	-0.00	-0.00	-0.00	-0.00	0.00

Table 5.6: Difference in roll amplitudes (deg) from Raspberry Pis and potentiometer

Run Number	Weight [N]	Vertical Position	Navio 1	Navio 2	Navio 3	Navio 4	Navio Average
1.0	1.00	Low	0.71	0.68	0.71	0.64	0.68
2.0	1.00	Medium	0.65	0.63	0.76	0.72	0.69
3.0	1.00	High	0.70	0.67	0.75	0.74	0.72
4.0	5.00	Low	0.59	0.67	0.73	0.71	0.68
5.0	5.00	Medium	0.64	0.62	0.71	0.64	0.65
6.0	5.00	High	0.61	0.62	0.67	0.63	0.63
7.0	10.00	Low	0.62	0.56	0.64	0.53	0.59
8.0	10.00	Medium	0.44	0.47	0.47	0.39	0.44
9.0	10.00	High	0.47	0.35	0.58	0.25	0.41
Average	-	-	0.60	0.59	0.67	0.58	0.61

Table 5.5: Difference in roll periods (s) computed by Raspberry Pis and potentiometer

Run Number	Weight [N]	Vertical Position	Navio 1	Navio 2	Navio 3	Navio 4	Navio Average
1.0	1.00	Low	0.00	0.00	0.03	-0.02	0.00
2.0	1.00	Medium	-0.03	-0.03	-0.03	-0.03	-0.03
3.0	1.00	High	0.03	0.00	0.00	0.03	0.00
4.0	5.00	Low	-0.02	0.00	0.00	0.03	0.00
5.0	5.00	Medium	-0.02	0.03	0.00	0.03	0.00
6.0	5.00	High	0.03	0.03	0.00	0.03	0.03
7.0	10.00	Low	0.00	0.00	0.00	0.00	0.00
8.0	10.00	Medium	0.03	0.00	0.03	0.00	0.00
9.0	10.00	High	0.03	0.00	0.00	0.00	0.00
Average	5.33	NaN	0.01	0.00	0.00	0.01	0.00

In terms of the ability to detect changes due to vertical shifts in waves the results show that for the weights used during the tests, monitoring the roll periods in waves does not provide insights on changes due to vertical wave shifts as Table 5.1 and Table 5.2 do not show any significant changes when both the weights and the vertical position are changed. The roll periods measured are directly related to the encounter frequency of the waves.

Even though significant changes are not seen in the roll period due to vertical shifts in weight, trends in roll amplitude suggest that cost-effective technologies can still be used to monitor effects of changing position of weights on a vessel. Figure 5.1 shows that for all the weights, as the weights are moved higher on the vessel, the roll amplitudes increase, with the largest increase being observed by shifts in the largest weight (10N). These results are as expected considering the discussions in Chapter 2 show that the higher a vessel's centre of gravity, the smaller the metacentric height, and the more unstable it becomes. In that case, increasing the height of

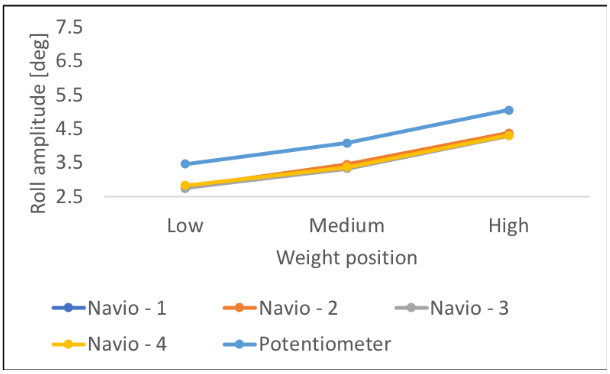

(A) 1N

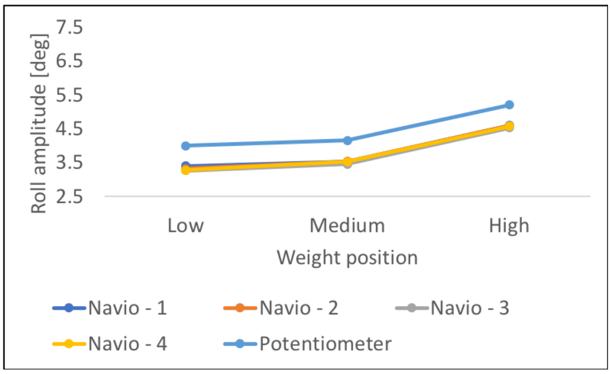

(B) 5N

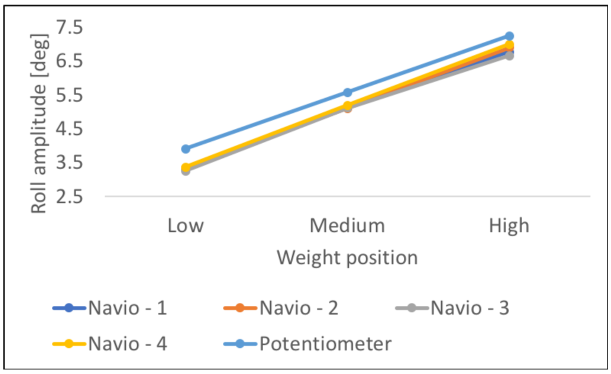

(C) 10N

Figure 5.1: Roll amplitudes for varying vertical heights of weights (1N, 5N, 10N)

the weights increases the height of the vessel's centre of gravity and decreases the metacentric height, resulting in the higher roll amplitudes for the same operating conditions.

5.5 Summary

In this chapter the ability of cost-effective computing technologies to detect changes in a vessel's stability due to vertical shifts of weights were investigated. It was found that even though vertical shifts in the weights used did not reflect in changes in roll period as the wave period determined the vessel's roll period, they did have an effect on the vessel's roll amplitude, given the same wave condition. The observed changes in roll amplitude, with larger amplitudes when the weights were moved higher were expected. This is because the vertical movement of weights upwards increases the vessel's centre of gravity while decreasing the metacentric height.

After investigating vertical weight shifts in this chapter, the next chapter investigates horizontal weight shifts and the use of cost-effective technologies in conducting the inclining experiment.

Chapter 6

Ability to detect horizontal weight shifts

The previous chapter investigated the use of cost-effective technologies in determining changes to a vessel in waves due to weights shifting vertically. This chapter investigates how the movements of weights horizontally can be used to assess the stability of vessels by using the inclining test to determine the metacentric height. In addition, the vessel's roll period is also recorded to investigate the relationship between the roll period and the metacentric height as recommended by the International Maritime Organization.

6.1 Introduction

Even though the roll period test is recommended as a method of assessing stability, the inclining test is the primary method for assessing vessel stability (International Maritime Organization, 2009) and is required for all vessels over 24 metres in length. As the displacement of vessels tend to increase in service with weight additions typically higher vertically on the vessel (Tupper, 1996), the inclining experiment is used to track these changes. These changes over time lead to changes in the vessel's metacentric height.

During the inclining experiment, known weights are shifted known distances to cause small angels of heel of the vessel. The angles of heel are typically measured by using suspended pendulums as shown in Figure 6.1. In this chapter, rather than using pendulums to measure the heel angle, the potentiometer and the Raspberry Pis are used to measure the heel angle. The metacentric height calculated using the heel angle readings from the potentiometer and the Raspberry Pis are then compared to assess the ability of using cost-effective technologies in assessing stability by using results from the inclining test to determine the vessel's metacentre.

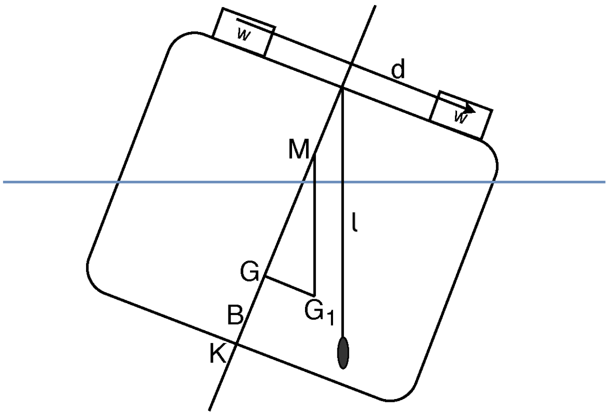

FIGURE 6.1: Inclining experiment for a vessel with a known weight (w) shifted by a distance (d). Adapted from *Ship Stability: Intact Stability Criteria and Inclining Experiment,* by Chakraborty (2017b)

6.2 Methodology

The same model vessel and towing tank used in the previous two chapters are used in this chapter. The difference in methodology from the previous chapters is that rather than inducing the vessel to roll using rotating weights as done in Chapter 4 or waves from the wavemaker in Chapter 5, the vessel is inclined to heel by shifting 4 weights of 2N on the vessel a distance of 0.18 metres from the centre line. The weight shifts are performed in nine sequences as shown in Figure 6.2.

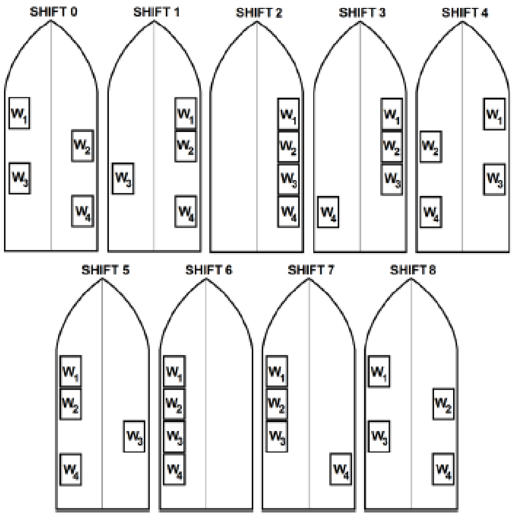

FIGURE 6.2: Weight shift sequence. Adapted from *Tearing down the wall - The inclining experiment,* by Karolius and Vassalos (2018a)

For each sequence the heel angle is recorded by the Raspberry Pis and the potentiometer. After the weight shift sequence, a roll period test is also conducted. This was done to enable comparisons between the roll period determined from the roll period test for this loading condition, and the roll period computed from the calculated metacentric height. The International Maritime

Organization (2009) presents the relationship between the roll period and the metacentric height in terms of a vessel's beam (B), length at waterline (L), and draft (D) as

$$T = \frac{2cB}{\sqrt{GM}} \qquad c = 0.373 + 0.023\frac{B}{D} - 0.043\frac{L}{100} \tag{6.1}$$

6.3 Results and discussion

The heel angle from each of the weight shift sequences are shown in Table 6.1 and illustrated in Figure 6.3. As expected as more weights are shifted to one side of the vessel, the higher the absolute magnitude of the heel angle.

TABLE 6.1: Heel angle for each weight shift sequence

Shift	Navio - 1	Navio - 2	Navio - 3	Navio - 4	Navio - Average	Potentiometer
0	0.56	0.56	0.41	0.48	0.51	0.27
1	-1.79	-1.70	-1.80	-1.44	-1.68	-2.09
2	-3.73	-3.86	-3.91	-3.80	-3.82	-4.68
3	-1.34	-1.36	-2.10	-1.58	-1.60	-2.93
4	0.69	0.91	0.49	0.71	0.70	0.34
5	3.44	3.34	3.24	3.35	3.34	3.02
6	5.45	5.44	5.28	5.24	5.35	5.33
7	2.64	2.65	2.39	2.48	2.54	1.71
8	0.26	0.40	0.08	0.16	0.23	-0.27

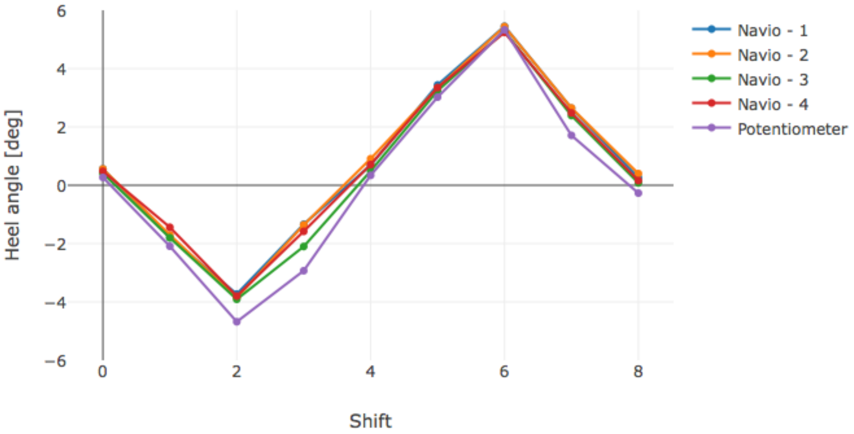

FIGURE 6.3: Heel angle for each weight shift sequence

The results show that the differences observed in heel angle readings between the Raspberry Pis and heel angle readings from the potentiometer are more significant than the differences observed in roll periods in previous chapters. Across all runs and all 4 devices the maximum difference in heel computed by the Raspberry Pis and the potentiometer is 1.59 degrees as shown in Table 6.2. The average difference between the Raspberry Pis and the potentiometer is -0.54 degrees with a standard deviation of 0.40 degrees.

TABLE 6.2: Difference between potentiometer and Raspberry Pi heel angles for each weight shift sequence

Shift	Navio - 1	Navio - 2	Navio - 3	Navio - 4	Navio - Average
0	-0.29	-0.29	-0.14	-0.21	-0.24
1	-0.30	-0.39	-0.29	-0.65	-0.41
2	-0.95	-0.82	-0.77	-0.88	-0.86
3	-1.59	-1.57	-0.83	-1.35	-1.33
4	-0.35	-0.57	-0.15	-0.37	-0.36
5	-0.42	-0.32	-0.22	-0.33	-0.32
6	-0.12	-0.11	0.05	0.09	-0.02
7	-0.93	-0.94	-0.68	-0.77	-0.83
8	-0.53	-0.67	-0.35	-0.43	-0.50
Average	-0.61	-0.63	-0.38	-0.54	-0.54

From the heel angles for each weight shift sequence, the metacentric height can be calculated. The classical method for calculating the metacentric height is based on the assumption that as the vessel is inclined for small angles during the experiment, the location of the metacentre is constant. From the inclining experiment, the metacentric height is calculated using the following Equation:

$$GM = \frac{w \times d}{W \tan\theta} \tag{6.2}$$

where:

w, is a known weight,

θ, is the heel angle,

d, is the distance the known weight is shifted, and

W, is the mass displacement of the ship.

Considering Equation 6.2, the metacentric height can be calculated by plotting each value of the moment divided by the vessel displacement ($\frac{w \times d}{W}$) against the tangent of the heel angle ($\tan\theta$) as shown in Figure 6.4. The slope of the best-fit line obtained by an ordinary least squares regression estimates the metacentric height from the readings by the Raspberry Pis and the potentiometer as summarised in Table 6.3

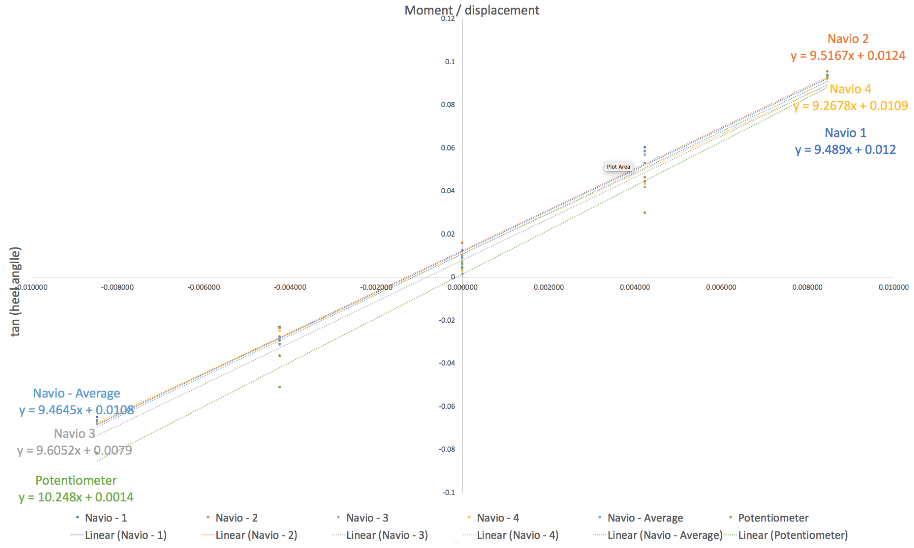

FIGURE 6.4: Moment divided by displacement against tangent of heel angle

The columns in Table 6.3 are obtained as follows;

- Metacentric height, GM (m): This is obtained from the slope when the moment divided by the displacement is plotted against the tangent of the heel angle as shown in Figure 6.4.
- R-squared: This is obtained from the ordinary least squares regression used to estimate the metacentric height.
- Peak frequency (Hz): This is obtained from the spectra computed using the time series measurements from a roll period test of the model.
- Measured roll period (s): This is the inverse of the peak frequency.
- Roll period estimated from GM (s): This is obtained from the relationship between the roll period and the metacentric height (International Maritime Organization, 2009). This relationship is in terms of the vessel's beam (B), length (L), and draft (D) as specified by Equation 6.3

$$T = \frac{2cB}{\sqrt{GM}} \qquad c = 0.373 + 0.023\frac{B}{D} - 0.043\frac{L}{100} \tag{6.3}$$

Table 6.3 shows that the heel angles for the weight shift sequences vary as expected. This is because the lines of best fit shown in Figure 6.4 have high R squared values which are indicators of goodness of fit. The R squared values in Table 6.3 for the cost-effective technologies have an average of 0.990 with a standard deviation of 0.001. The table also shows that the calculated metacentric height is as expected by comparing the measured roll period with the roll period calculated using Equation 6.3. The average difference between these roll periods for the model is 0.061 seconds with a standard deviation of 0.024 seconds.

Table 6.3: Model inclining test results

Device	Metacentric height GM (m)	R squared	Peak frequency (Hz)	Measured roll period (s)	Roll period estimated from GM (s)
Navio - 1	0.095	0.989	0.774	1.293	1.250
Navio - 2	0.095	0.993	0.762	1.312	1.248
Navio - 3	0.096	0.990	0.760	1.315	1.243
Navio - 4	0.093	0.989	0.770	1.299	1.265
Navio - Average	0.095	0.992	0.767	1.304	1.252
Potentiometer	0.102	0.978	0.766	1.305	1.203

The results shown in Table 6.3 are used to assess the difference between the Raspberry Pis and the potentiometer as shown in Table 6.4. Firstly, the difference in measured roll period is similar to findings in previous chapters with an average difference of 0.012 seconds between roll periods from the Raspberry Pis and the potentiometer. Even though the difference in roll periods estimated from the computed metacentric heights are higher with an average difference of 0.049 seconds, this is still not significant considering that the uncertainty associated with using a stopwatch to measure roll period is ± 0.2 seconds. The difference in metacentric heights and R-squared values between the Raspberry Pis and the potentiometer are also small with average differences of 0.008 m and 0.012 respectively.

Table 6.4: Difference between model inclining test results recorded by the Raspberry Pis and the potentiometer

Device	Metacentric height GM (m)	R squared	Peak frequency (Hz)	Measured roll period (s)	Roll period estimated from GM (s)
Navio - 1	0.008	-0.011	-0.007	0.012	-0.047
Navio - 2	0.007	-0.015	0.004	-0.007	-0.045
Navio - 3	0.006	-0.012	0.006	-0.010	-0.040
Navio - 4	0.010	-0.011	-0.004	0.006	-0.062
Navio - Average	0.008	-0.014	-0.000	0.001	-0.049

The results obtained from this inclining test are also considered at full-scale and presented in Table 6.5. The metacentric height, peak frequency, and measured roll period columns are obtained by applying Froude conversion laws to the model values in Table 6.3. The obtained full-scale metacentric heights are then used to calculate the roll period estimated from GM according to Equation 6.3. Similar to the model scale results, the full-scale results for the measured roll period and the roll period estimated from the metacentric height are similar with differences having an average of 0.366 seconds and a standard deviation of 0.092 seconds.

Table 6.5: Inclining test results at full-scale

Device	Metacentric height GM (m)	Peak frequency (Hz)	Measured roll period (s)	Roll period estimated from GM (s)
Navio - 1	1.423	0.200	5.007	4.712
Navio - 2	1.427	0.197	5.080	4.705
Navio - 3	1.441	0.196	5.093	4.683
Navio - 4	1.390	0.199	5.030	4.768
Navio - Average	1.420	0.198	5.052	4.718
Potentiometer	1.537	0.198	5.054	4.534

The differences between full-scale results from the Raspberry Pis and full-scale results from the potentiometer are shown in Table 6.6.

Table 6.6: Difference between inclining test results at full-scale by the Raspberry Pis and the potentiometer

Device	Metacentric height GM (m)	Peak frequency (Hz)	Measured roll period (s)	Roll period estimated from GM (s)
Navio - 1	0.114	-0.002	0.048	-0.178
Navio - 2	0.110	0.001	-0.026	-0.171
Navio - 3	0.096	0.001	-0.038	-0.149
Navio - 4	0.147	-0.001	0.025	-0.234
Navio - Average	0.117	-0.000	0.002	-0.184

6.4 Summary

This chapter demonstrated how heel angle readings from cost-effective technologies can be used to estimate a vessel's metacentric height. The differences between metacentric heights results from the Raspberry Pis and the potentiometer both at model scale and full-scale indicate that the Raspberry Pis have the potential to be used in inclining tests. The obtained metacentric heights were also validated by using them to compute the roll period and then comparing the computed roll period with roll period measured from a roll period test.

All the previous chapters have compared results from the Raspberry Pis with results from the potentiometer. The next chapter compares readings from a Raspberry Pi with readings from an industrial IMU and an optical motion capture system.

Chapter 7

Comparison between cost-effective technologies and the state-of-the-art

This chapter compares motion readings from the optical motion capture system with readings from an SBC coupled with an IMU and a commercial IMU. This comparison further assesses whether low-cost SBCs and IMUs can be used to measure vessel motion from which roll period and the metacentric height can be determined as seen in the previous chapters.

7.1 Introduction

Traditional methods of measuring a vessel's motion in 6 DOF, accelerations and velocities, in towing tanks include the use of wired instrumentation systems, optical systems or IMUs. A wired instrumentation system as used in the previous chapters requires the vessel to be connected to a towing carriage throughout the experiment. Figure 7.1 shows an example of such a setup.

There are disadvantages related to using wired instrumentation systems. Firstly, they require additional equipment to retrieve and analyse the data, such as amplifiers, cables, and laptops. In this setup, the vessel's surge and yaw accelerations are restricted, and if it is being towed at a fixed speed, the roll motion is also restricted. The use of a towing post in wired instrumentation systems assumes that surge is uncoupled from other motions, which in reality is not true.

Optical systems use a large number of cameras in combination with markers placed on the vessel to capture its acceleration by tracking the position of the markers over time. These systems do not require the vessel to be connected to the towing carriage. Currently, they are the most expensive type of system used to capture vessel motions in a towing tank. Similar to wired instrumentation systems, optical systems are not used in full-scale measurements because they

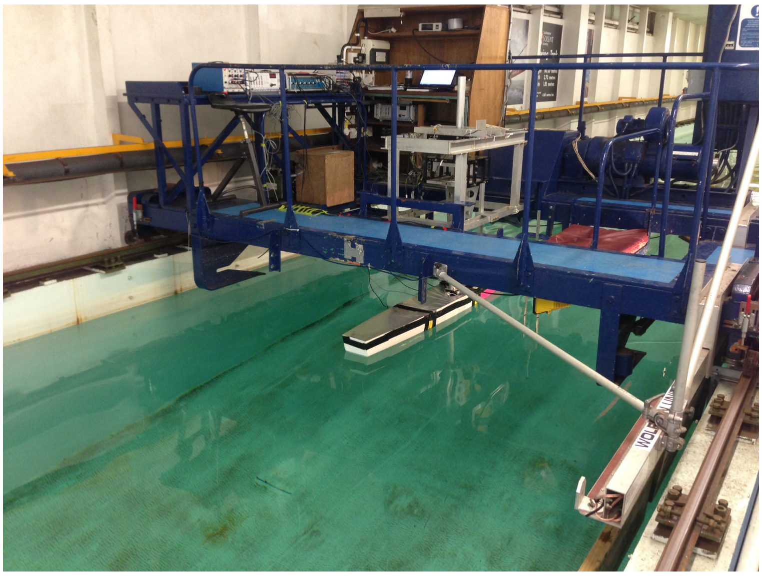

Figure 7.1: Wired measurement system in a towing tank.

both require a shore-based setup. For full-scale measurements, commercially available IMUs have been used by container ships in vessel stability monitoring systems such as those offered by Hoppe Marine (2018) and Totem Plus (2015). Similar IMUs have also been used in towing tanks to measure vessel motions (Bennett et al., 2014).

In this chapter, we compare measurements from an optical motion capture system with measurements from an SBC coupled with a low-cost IMU, and a commercial IMU. This was done to assess the possibility of replacing measurements from the optical motion capture system with readings from an cost-effective technologies. In order to make comparisons between the different measurements, the pitch motion of an autonomous surface vehicle (ASV) was used as measurements of angular motion. Pitch was used rather than roll in this chapter due to practical mounting restrictions and movement of the ASV.

7.2 Hardware

This section discusses the hardware which was compared. These were the Raspberry Pi coupled with the Navio2 shield, the XSens IMU, and the Qualisys optical motion capture system.

7.2.1 XSens

Sensors produced by XSens have been used by leading research institutions to measure vessel motion at full-scale (Koning, 2009). The XSens MTi 10 IMU was used in combination with a touchscreen laptop which was placed in the ASV since there was no way of communicating wirelessly with the IMU. The specifications for the gyroscope and accelerometer are given in Table 7.1. The XSens MT Software Suite running on the laptop was used to configure the IMU and control recording of data via the graphical user interface (GUI). The XSens recorded the accelerometer and gyroscope data at 400 Hz and recorded the magnetometer data at 100 Hz.

Table 7.1: MTi 10-series sensor specifications

	Gyroscope	**Accelerometer**
Standard full range	450 deg/s	50 m/s^2
Bias repeatability (1 yr)	0.2 deg/s	0.03 m/s^2
In-run bias stability	18 deg/h	40 μ g
Bandwidth (-3dB)	415 Hz	375 Hz
Noise density	0.03 deg/s/$\sqrt{\text{Hz}}$	80 $\mu g/\sqrt{\text{Hz}}$
g-sensitivity (calibrated)	0.006 deg/s/g	N/A
Non-orthogonality	0.05 deg	0.05 deg
Non-linearity	0.03 % FS	0.03 % FS

The XSens IMU costs $1122.84 (Farnell Element 4, 2016). In comparison with the other devices used in the experiment, it is not as expensive as the optical system but more expensive than the SBC.

7.3 Experimental Setup

The particulars of the free-running ASV used are given in Table 7.2. The autonomous surface vehicle, which had two submerged NACA0012 (Critzos et al., 1955) foils for propulsion along the towing tank (Bowker et al., 2016), was tested in head and following regular waves, which were kept at a constant wave height of 0.12 m. The wave frequency was increased from 0.5 Hz to 0.8 Hz at increments of 0.1 Hz as summarised in Table 7.3.

Table 7.2: Particulars of the autonomous surface vehicle

Parameter	**Value**	**Units**
Waterline length	2.27	m
Beam	0.30	m
Draft	0.10	m
Displacement	52.00	kg
Chord	0.23	m
Span	1.00	m
Foil type	NACA0012	-
Foil arm	0.40	m

The ASV was stationed at the carriage 30 m from the wavemaker and progressed towards the wavemaker in head waves before being turned around and tested in following waves. The period for each run varied from 60 to 180 seconds depending on the forward speed of the ASV and the wave reflection from the opposite end of the tank. During each run, the optical motion capture system (Qualisys) recorded the vessel's pitch and heave displacements and accelerations. The optical motion capture system consisted of eight Oqus 500+ cameras and captured the ASV's motions in six degrees of freedom (DOF) at a rate of 60 Hz. Each camera had a maximum capture distance of 25 m and a 49° horizontal field of vision (Qualisys Motion Capture Systems, 2018).

TABLE 7.3: Wave direction, wave amplitude, and wave frequency for each run

Run number	Vessel direction with respect to wavemaker	Wave Amplitude (m)	Wave Frequency (Hz)
1	Towards	0.06	0.50
2	Away	0.06	0.50
3	Towards	0.06	0.60
4	Away	0.06	0.60
5	Towards	0.06	0.70
6	Away	0.06	0.70
7	Towards	0.06	0.80
8	Away	0.06	0.80

FIGURE 7.2: Arrangement of 8 Oqus 500+ cameras alongside the towing tank.

As shown in Figure 7.2, all eight cameras were placed in a row along one side of the towing tank due to practical mounting restrictions. Eight cameras were used to ensure a long coverage volume. This enabled the ASV to remain within the view of the cameras for a sufficient amount of time while it travelled along the length of the towing tank. With the trajectory of the ASV 3.5 m from the cameras, each camera with a horizontal view of 49° covered a length of 3.2 m. Since each unit length was viewed by at least two cameras, the system covered a total length of 12.8 m.

The cameras were daisy-chained and connected to a laptop running the Qualisys Track Manager software (v2.12). This software's graphical user interface (GUI) enables the user to control the cameras' settings, start and stop recording, calibrate the system, and playback recorded runs. A summary of the camera marker settings and video settings used in this setup are presented in Table 7.4.

The Qualisys software computed 3-dimensional (3D) and 6 DOF data from 2-dimensional (2D) marker data. With a measuring volume of 1m x 5m x 10m, the system provides angular accuracy of 0.05° and spatial accuracy of 0.25 mm (Qualisys Motion Capture Systems, 2016). In order for

Table 7.4: Qualisys Camera Settings

(a) Marker Settings

Property	**Value**
Capture rate	60 Hz
Exposure time	0.0005 s
Marker threshold	15 %
Marker type	Passive
Sensor mode	4 MP at 179 Hz

(b) Video Settings

Property	**Value**
Capture rate	13 Hz
Exposure time	0.076903 s
Flash time	0.002 s
Gain	4
Sensor mode	4 MP at 179 Hz

the software to properly compute 3D data from 2D camera images, a wand calibration technique was used to determine the orientations of the cameras. This method used 2 objects to calibrate the optical motion capture system. These objects were an L-shaped structure with 4 markers and a wand with 2 markers. The wand was moved through as many different positions and orientations as possible through the volume the ASV was expected to operate in, with the cameras recording at 100 Hz. The L-frame was fixed throughout the experiment to determine the reference frame. Once the calibration was completed, when tracking markers, the system determined the 3D location of a marker $\begin{bmatrix} X_{\text{world}} & Y_{\text{world}} & Z_{\text{world}} & 1 \end{bmatrix}^T$ from the 2D camera image $\begin{bmatrix} x_{\text{camera}} & y_{\text{camera}} & 1 \end{bmatrix}^T$ using the pin-hole camera model (Faugeras, 1994; Shin and Mun, 2012; Borghese and Cerveri, 2000) represented in Equation 7.1.

$$\begin{bmatrix} x_{\text{camera}} \\ y_{\text{camera}} \\ 1 \end{bmatrix} = K \times [R \mid t] \times \begin{bmatrix} X_{\text{world}} \\ Y_{\text{world}} \\ Z_{\text{world}} \\ 1 \end{bmatrix} \tag{7.1}$$

where

K, is a 3 x 3 intrinsic camera property matrix,
R, is a 3 x 3 extrinsic rotation matrix,
t, is a 3 x 1 extrinsic translation matrix, and
$\times$, indicates the cross product of 2 matrices.

The optical motion capture system's reference frame is shown in Figure 7.3 with the positive x-direction being towards the wavemaker, the positive y-direction being towards the mounted cameras, and the positive z-direction being upwards. Figure 7.3 also shows the location of the five markers which indicate the locations of the acceleration readings. The markers were placed asymmetrically to enable the optical motion capture system to better distinguish between them, and for a unique definition of the ASV's orientation. Five markers were used in total as four markers are recommended for redundancy, with at least three required to define the ASV as a rigid body (Schoonderwaldt and Thompson, 2016).

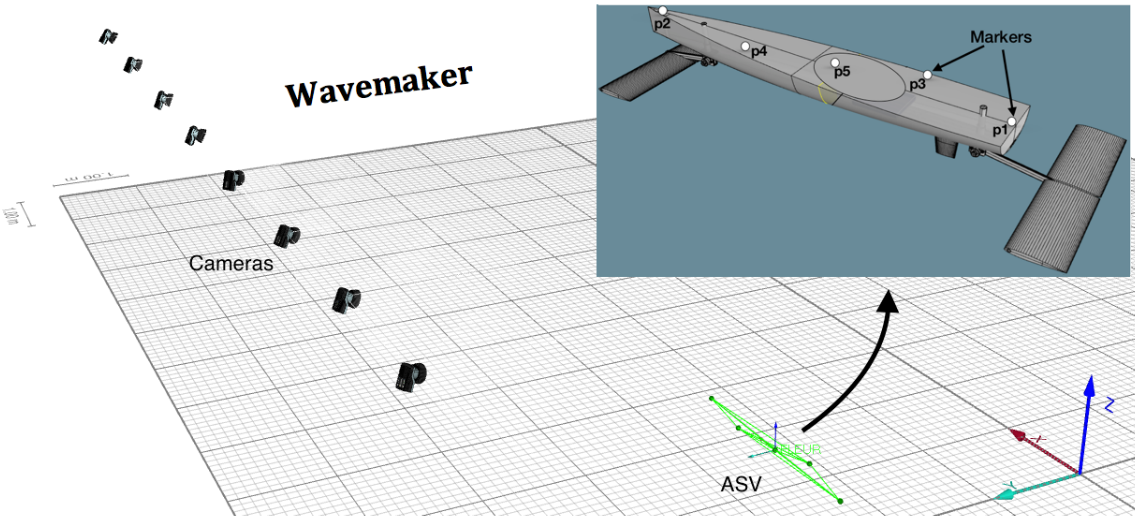

FIGURE 7.3: Experimental setup showing the 8 mounted cameras, the location of the wavemaker, and the position of the markers on the ASV.

7.4 Method

The ASV was tested in head and following regular waves, which were kept at a constant wave height of 0.12 m and the wave frequency was increased from 0.5 Hz to 0.8 Hz in increments of 0.1 Hz. During each run, the Raspberry Pi, the commercially available inertial sensor (XSens), and the optical motion capture camera system (Qualisys) recorded the ASV's pitch motions. As shown in Figure 7.4, the longitudinal location of the XSens IMU is 90.5 cm from the stern of the ASV. This was near the longitudinal centre of gravity (LCG) which was 98.0 cm from the stern of the ASV. The XSens IMU was 10.0 cm above the keel line. The Raspberry Pi was 85.0 cm from the stern of the ASV and 6.0 cm above the keel line.

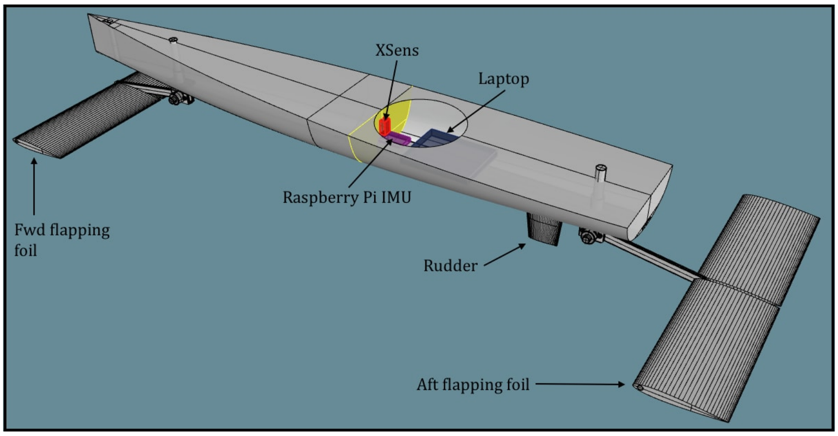

FIGURE 7.4: Sensor placement on ASV

The pitch values obtained from Qualisys, XSens and the Raspberry Pi were computed differently. The Qualisys system computed pitch from measured marker positions using the Qualisys Track Manager software. The Raspberry Pi computed pitch from the IMU data using the Madgwick et al. (2011) algorithm and the pitch measured by the XSens IMU was computed by the XSens MT Software Suite. Before analysing the pitch data for all sensors, all the time series were resampled to 20 Hz in order to have all of them at the same sample rate. Afterwards, any trends in any of the time series were removed by using a moving average (Smith, 2003) to estimate the trend and then subtract this from the time series.

7.5 Results and discussion

Figure 7.5 presents the pitch of the ASV during Run 1 recorded using XSens, Qualisys, and both IMUs used with the Raspberry Pi (LSM9DS1 and MPU9250) after detrending. The figures for all the runs were similar with slightly different amplitudes and frequencies. The time series were out of phase because the Raspberry Pi, XSens and Qualisys recordings were started at different times. Even though efforts were made to start each of these at precisely the same time, each system takes a different amount of time to start recording, resulting in the time series being unsynchronised. Synchronisation of the data recorded by the IMUs and Qualisys was required before any comparisons between the data could be made.

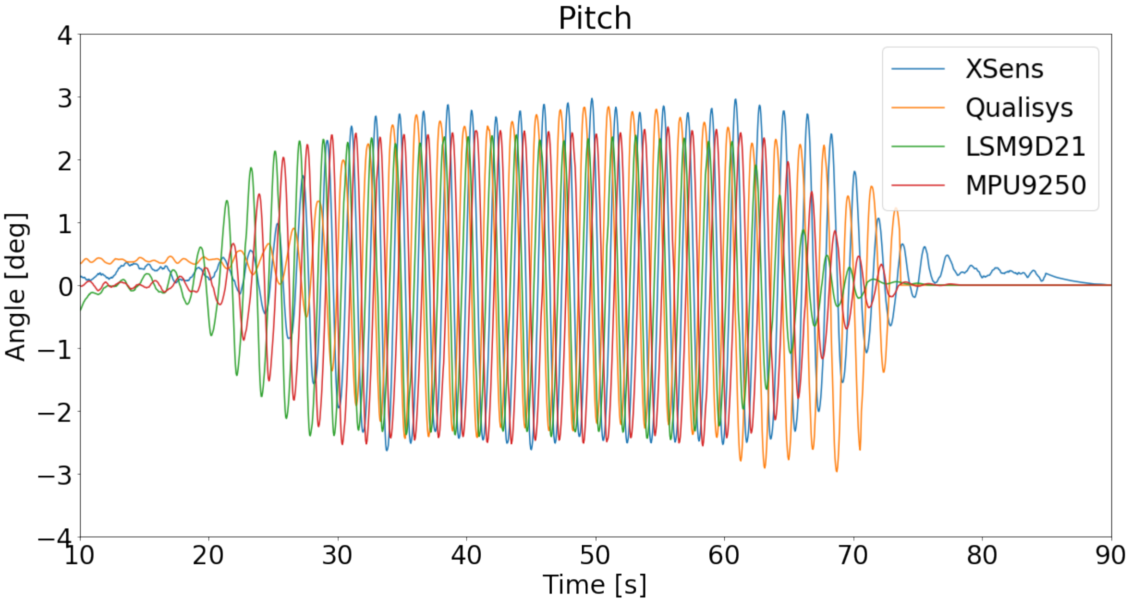

FIGURE 7.5: Data from Run 1 before synchronisation

The synchronisation of the different time series was achieved by minimising the Euclidean distance (L_2-norm) between them. The Euclidean distance between points in 2 time series (r and s) can be computed using Equation 7.2 (Morse and Patel, 2007).

$$L_2\text{−norm} = ||r_i - s_i||_2 = \sqrt{\sum_{i=1}^{n}(r_i - s_i)^2} \tag{7.2}$$

In this case, r_i was always the Qualisys data, thereby minimising the Euclidean distance between the Qualisys time series and all the others. The Euclidean distance is a simple method of synchronising the data and is competitive with more complex methods like Dynamic Time Warping (Ding et al., 2008). Figure 7.6 presents the pitch of the ASV during Run 1 after the time series of XSens, Qualisys, and both IMUs used with the Raspberry Pi (LSM9DS1 and MPU9250) had been synchronised.

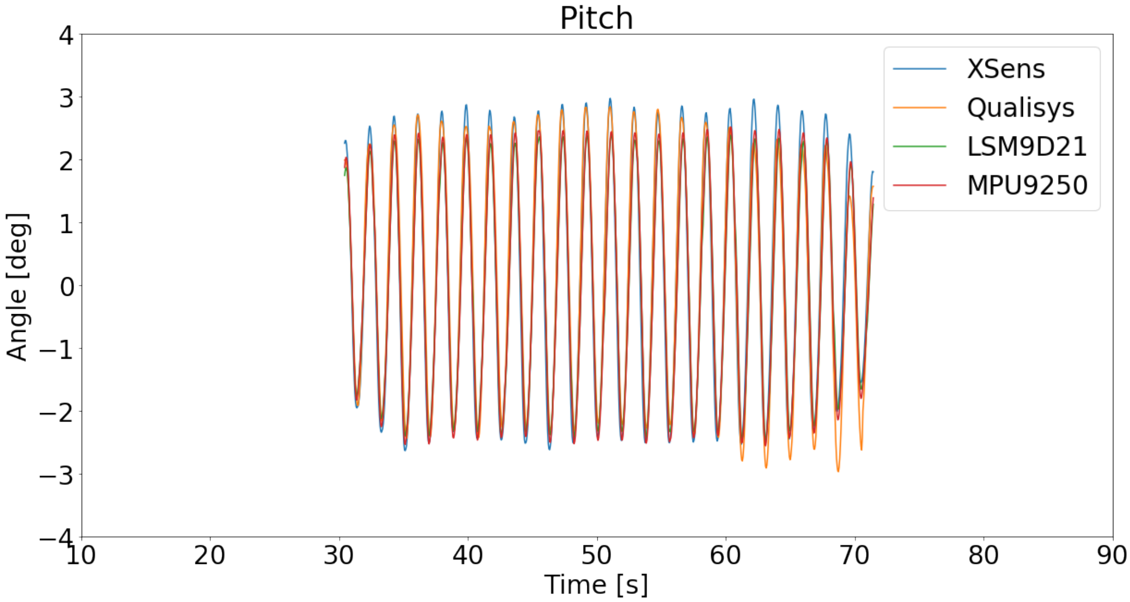

FIGURE 7.6: Data from Run 1 after synchronisation

After synchronisation, only a subsection of the data was used. This subsection excluded the beginning of the recording when the wavemaker was building up to the specified wave amplitude and the ending of the data when the waves had passed. In some instances, the ending of the data was also excluded because the ASV went outside the view of the cameras, resulting in an instantaneous flat line in the data recorded by the Qualisys system.

In assessing the accuracy of XSens and the 2 IMUs on the Navio2 Shield (MPU9250 and LSM9DS1), the mean absolute deviation (MAD) from Qualisys data for all data points and the root-mean-square deviation (RMSD) from Qualisys data were calculated using Equation 7.3 and Equation 7.4 respectively. These are presented in Table 7.5.

$$\mathrm{MAD} = \frac{1}{n}\sum_{i=1}^{n} |r_i - s_i| \tag{7.3}$$

$$\mathrm{RMSD} = \frac{1}{n}\sqrt{\sum_{i=1}^{n} (r_i - s_i)^2} \tag{7.4}$$

Table 7.5: Deviation of XSens, LSM9D2S1, and MPU9250 data from Qualisys data

(a) Mean absolute deviation (MAD)

Runs	**XSens (deg)**	**LSM 9DS1 (deg)**	**MPU 9250 (deg)**
1	0.30	0.37	0.34
2	0.27	0.48	0.37
3	0.29	0.46	0.43
4	0.16	0.40	0.29
5	0.35	0.51	0.53
6	0.33	0.39	0.30
7	0.33	0.39	0.41
8	0.27	0.28	0.24
Average	0.29	0.41	0.36

(b) Root-mean-square deviation (RMSD)

Runs	**XSens (deg)**	**LSM 9DS1 (deg)**	**MPU 9250 (deg)**
1	0.39	0.46	0.42
2	0.38	0.55	0.44
3	0.37	0.57	0.53
4	0.22	0.45	0.34
5	0.41	0.61	0.64
6	0.40	0.48	0.40
7	0.41	0.45	0.49
8	0.31	0.35	0.30
Average	0.36	0.49	0.45

The Qualisys dataset was used as the reference because the Qualisys system is known to have high accuracy. Qualisys systems have been used to accurately measure a variety of variables ranging from tooth displacements (Liu et al., 2007) to arm movements (Salim et al., 2010). With a measuring volume of 1m x 5m x 10m, the system provides an angular accuracy of 0.05° and spatial accuracy of 0.25 mm (Qualisys Motion Capture Systems, 2016).

The mean absolute deviation is the average magnitude of errors without considering the direction of these errors and measures accuracy for continuous variables. The mean absolute deviation weights all errors equally. The root-mean-square deviation also measures the average magnitude of the error. The root-mean-square deviation gives a relatively high weight to larger errors because errors are squared before averaging. It is a more useful measure when large errors are particularly undesirable. The root-mean-square deviation is always greater than or equal to the mean absolute error. The greater the difference between these 2 errors, the greater the variance in the individual errors in the sample.

From Table 7.5, it can be seen that the Xsens IMU had the least mean absolute deviation from Qualisys, followed by the MPU9250 IMU and then the LSM9DS1 IMU. They had average MAD values of 0.29°, 0.36°, and 0.41° respectively. The order of agreement is the same for the root-mean square deviation with the XSens IMU having the lowest RMSD value of 0.36° and the LSM9DS1 IMU having the largest RMSD value of 0.49°.

In addition to the errors already calculated, the Pearson correlation coefficient (Lane, 2013) between the Qualisys data and all the other data was computed. The Pearson correlation coefficient is used to benchmark linear relationships and shows the strength of a relationship between 2 variables. The Pearson coefficient, r, for 2 datasets x and y was calculated using Equation 7.5.

$$r = \frac{\Sigma(x_i - \bar{x})(y_i - \bar{y})}{\sqrt{\Sigma(x_i - \bar{x})^2 \Sigma(y_i - \bar{y})^2}} \tag{7.5}$$

The Pearson correlation coefficient for the XSens, MPU9250, and LSM9DS1 IMUs are presented in Table 7.6. As expected the correlation coefficient values for all the IMUs were high with the XSens IMU having a slightly higher value.

Table 7.6: Pearson Correlation Coefficient

Runs	**XSens**	**LSM 9DS1**	**MPU 9250**
1	0.978	0.974	0.977
2	0.990	0.993	0.993
3	0.988	0.981	0.983
4	0.996	0.994	0.994
5	0.978	0.974	0.967
6	0.992	0.983	0.988
7	0.961	0.965	0.950
8	0.994	0.971	0.976
Average	0.985	0.979	0.979

7.6 Summary

Comparisons between an optical motion capture system and a low-cost SBC coupled with an IMU showed the difference in pitch motion measurements between these devices to be less than 0.5 degrees. This work was motivated by the need for vessel operators to be able to monitor changes in how their vessels operate, the higher costs of current measurement systems, and the need for cheaper and more modular measurement techniques for measuring vessel motions. Improved orientation estimation techniques and sensor fusion algorithms can be implemented on the SBC to increase the accuracy of motion measurements. Also, due to the modular nature of the Raspberry Pi, the Navio2 shield can be substituted with cheaper, and more accurate IMUs as technology advances. As observed by comparing the LSM9DS1 IMU and the MPU9250 IMU, when choosing an IMU for measuring vessel motions the higher the sensitivity, the better the results.

Results show the developed system as a suitable substitute for measuring vessel motions in cases where cost is an essential factor, and the accepted margin of error for rotational motion is less than 0.5 degrees. Considering that optical motion capture systems cannot be used on vessels at sea because they require a shore-based setup, the results show that SBCs coupled with IMUs can be used to estimate the roll period a vessel at sea.

Chapter 8

Conclusion and further research

This chapter concludes this thesis with a summary of the main findings and how each chapter addresses the research questions posed in this thesis. The chapter ends with directions for further work.

8.1 Summary of thesis

Chapter 2 was a literature review of vessel stability and motion measurement, setting the stage for a discussion of the research questions. In this chapter, we introduced stability theory. A vessel's roll period and metacentric height were identified as parameter's which influence vessel stability. This chapter introduced an approach to computing the frequency/period of motion from recorded time series data using Welch's method. This was assessed by reproducing a known spectrum from time series data and then comparing the reproduced spectrum with the original spectrum. In addition, this method was used to compare different accelerometers in accurately detecting the period of simulated motion produced using a shaker table.

This thesis focused on using cost-effective technologies to measure the roll period and the metacentric height as indicators of safety. The use of cost-effective technologies in assessing changes in the roll period and the metacentric height were discussed in Chapters 4, 5, and 6 after the functional requirements were introduced in chapter 3. Before reviewing the research questions, the following provides a brief summary of the work presented in this thesis.

- Chapter 3 introduced the functional requirements for cost-effective technologies used to assess stability through the roll period and metacentric height. These requirements included accuracy, being sufficiently waterproof, easy installation and calibration, wireless communication, and being usable at full-scale.
- Chapter 4 assessed the ability of the cost-effective technologies in accurately detecting a range of roll periods of a model vessel computed from time series measurements using FFT. The results were assessed through comparisons with results from a potentiometer.

- Chapter 5 determined whether vertical movements of weights on a vessel in waves could be detected by the cost-effective technologies
- Chapter 6 assessed the ability of the cost-effective technologies in determining the metacentric height of a model vessel using heel angle readings from an inclining test. The metacentric height was also validated by comparing roll periods computed using the metacentric height with roll periods measured in a roll period test.
- Chapter 7 compared motion measurements from the cost-effective technologies with measurements from an industrial IMU and an optical motion capture system.

8.2 Review of research questions

The work presented in this thesis is assessed against the following research questions from Section 1.2:

1. How capable are cost-effective computing technologies in determining changes in roll period, a key parameter for vessel stability and how does this compare to calibrated test equipment?
2. To what extent can cost-effective computing technologies be used to able to assess changes in roll period due to movements of weights in waves?
3. How capable are cost-effective computing technologies in determining a vessel's metacentric height through an inclining test?
4. How do cost-effective computing technologies compare to existing, more expensive methods of measuring vessel motion?

How capable are cost-effective computing technologies in determining changes in roll period, a key parameter for vessel stability and how does this compare to calibrated test equipment?

Chapter 4 assessed the ability of cost-effective technologies in determining changes in roll period by comparing the roll period estimated from the Raspberry Pis with roll period estimated using a potentiometer. The average difference between the results was 0.00315 seconds with a standard deviation of 0.10677 seconds. This difference is less than the uncertainty associated with using a stopwatch to measure roll period (0.2 seconds) thereby satisfying the first functional requirement of accuracy. In addition, the cost-effective technologies recorded roll amplitudes which deviated from roll amplitudes recorded by the potentiometer by an average of 0.201 degrees. The cost-effective technologies are also sufficiently waterproof due to the IP65 waterproof case and took a shorter amount of time to set up on the vessel than setting up the potentiometer and all its associated equipment. Finally, the cost-effective technologies are capable of being used at full-scale since they are not shore-based while the potentiometer cannot be used at full-scale.

These findings suggest that cost-effective technologies are capable of determining changes in roll period.

To what extent can cost-effective computing technologies be used to able to assess changes in roll period due to movements of weights in waves

Chapter 5 addressed the question of whether cost-effective technologies can be used to evaluate changes in roll period due to movements of vessels in waves. By moving 3 different weights through 3 different vertical positions in waves, we found that the cost-effective technologies did not observe any significant changes in roll period due to these weight movements. On the other hand, changes in roll amplitude were detected, with larger amplitudes as weights were moved upwards. In addition, the increase in roll amplitudes were larger the larger the weight for the same increase in vertical position. Findings in this chapter suggest that even though monitoring stability changes due to vertical weight shifts onboard a vessel in waves may not be possible by monitoring the roll period, the roll amplitude can be used to observe changes in the vessel's behaviour due to the weight shifts.

How capable are cost-effective computing technologies in determining a vessel's metacentric height through an inclining test?

In regards to using cost-effective technologies in inclining tests to determine a vessel's metacentric height, Chapter 6 showed that the cost-effective technologies accurately detect the heel angle due to weight shifts used in calculating the metacentric height. This is with an average deviation from the potentiometer readings of 0.5 degrees and a standard deviation of 0.4 degrees. When these results are used to compute the metacentric height, the deviation between the metacentric height obtained from the cost-effective technologies and the metacentric height obtained from the potentiometer had an average deviation of 0.008 metres. The metacentric height obtained was further validated by comparing the roll period obtained by a roll period test of the vessel and the roll period calculated using the calculated GM. The results indicate the calculated metacentric height as valid since the difference between the 2 measurements was 0.061 seconds and suggest that cost-effective computing technologies are capable of determining a vessel's metacentric height through an inclining test.

How do cost-effective computing technologies compare to existing, more expensive methods of measuring vessel motion?

Chapter 6 compared motion measurements from the cost-effective technologies with motion measurements from an industrial IMU and an optical motion camera. The maximum difference in results between the cost-effective technologies and measurements from both the industrial IMU and the optical motion camera were less than 0.5 degrees. These cost-effective technologies have an additional advantage over the optical motion capture system as the optical motion capture system cannot be used at full-scale.

8.3 Future work

Based on the work done, this section suggests directions for future work. This includes the following:

Developing a simple user interface to improve the usability of the cost-effective technologies.

A simple user interface should be developed for the cost-effective technologies to improve usability for fishing vessel operators. There are a number of options which should be explored including a smartphone-based user interface that connects wirelessly or a touchscreen display connected directly to the cost-effective technologies. In addition, a distributed computing environment such as ROS could be used to develop a system in which multiple nodes of the developed cost-effective technologies can connect with each other when placed at different locations on a full scale vessel.

Deploying the cost-effective technologies at full-scale to measure a fishing vessel's roll period and metacentric height.

The experiments conducted in Chapter 4, Chapter 5, and Chapter 6 should be conducted on full-scale fishing vessel to assess the vessel's stability. This should be possible with the developed system as it has been able to detect stability changes at model scale (smaller amplitudes than at full scale) and tested at low frequencies equivalent to those at full scale. In these experiments, rather than comparing results with results from a potentiometer, the results from the cost-effective technologies should be compared with results from traditional methods of assessing vessel stability using a stopwatch and a pendulum. Particular attention should be paid to the magnitude of the difference between results from the cost-effective technologies and the traditional methods at full-scale.

Investigating the use of the cost-effective technologies as an early alert system for various modes of capsize such as parametric resonance.

Considering that this thesis has demonstrated that cost-effective technologies can be used to accurately determine roll period, future work should investigate the ability of the cost-effective technologies in providing an early warning for modes of capsize such as parametric resonance which occurs when the natural roll period of the vessel is approximately twice the wave encounter frequency, and the wavelength is between 0.8 and 2 times the ship length.

Investigating the use of cost-effective technologies in estimating the sea state from measured vessel response.

Current methods of obtaining data from which the sea state can be deduced include wave rider buoys, satellite measurements, and wave radar systems. Each of these methods has advantages and disadvantages. The advantage of wave rider buoys is that data obtained from them is freely available on the Internet through sources such as the National Oceanic and Atmospheric Administration's (NOAA) National Data Buoy Center (NDBC), the Met Office's Marine Automatic

Weather Stations (MAWS) network, the British Oceanographic Data Centre (BODC), and the Centre for Environment, Fisheries and Aquaculture Science (CEFAS). These buoys provide information such as the wind speed, wind direction, significant wave height, and dominant wave period. The disadvantage of using wave rider buoys is that they are in a fixed position and therefore provide information on a limited geographical region. There are also a small number of wave-buoys deployed. According to the NDBC, they have only 1372 stations deployed worldwide. Figure 8.1 shows how widely scattered these buoys are around the UK.

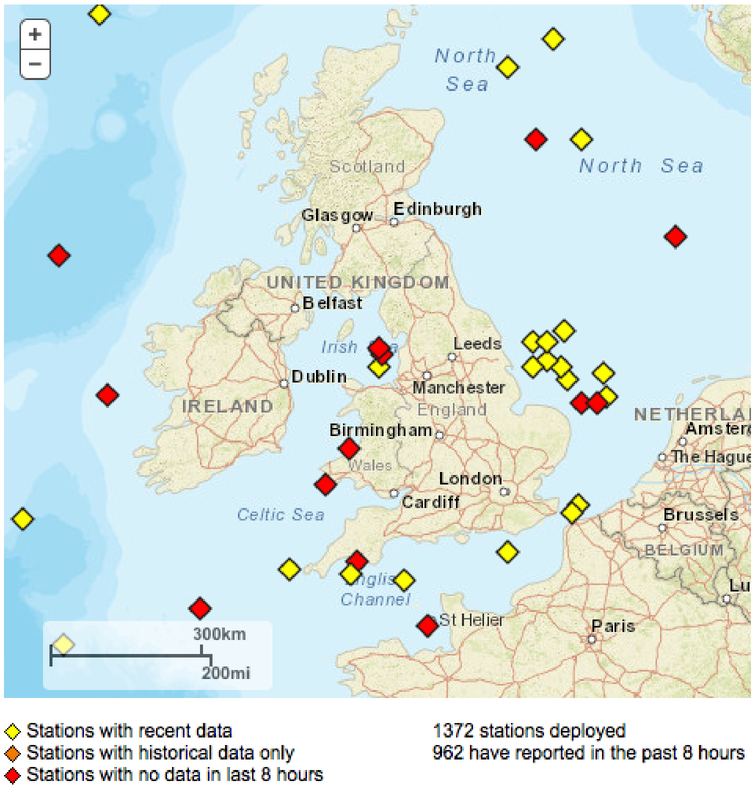

FIGURE 8.1: Wave buoys near the UK on 1st March 2018
by National Data Buoy Center (2018)

As compared to wave rider buoys, satellite measurements and wave radar systems have the advantage of being able to cover a larger region of interest. In addition, they are not fixed in position. However their disadvantages include their high initial costs and more complex computational hardware. Even though wave radar systems provide more information than several wave-buoys, they can cost up to four times the price of wave-buoys. Since knowledge of the sea state is needed to have an idea of how a vessel will respond during operation, and considering the advantages and disadvantages of wave-buoys, satellite measurements, and wave radar systems, it would be beneficial to be able to estimate the sea state from measured ship response through the use of sensor platforms in an in-service monitoring system. Such a system would be able to provide information regarding larger regions of interest since the vessels are not fixed in position. Information from such a system could be made available freely through automatic identification systems (AIS) used by vessel traffic services (VTS) such as Marine Traffic. In addition, such a system would be able to provide information at a much higher resolution on a region of interest due to the relatively high number of vessels in service. Figure 8.2 shows the high density of fishing vessels in the Marine Traffic Automatic Identification System. This system has approximately 69,000 live vessels and 508,000 vessels worldwide in its database. These numbers are significantly larger than the number of wave-buoys deployed worldwide.

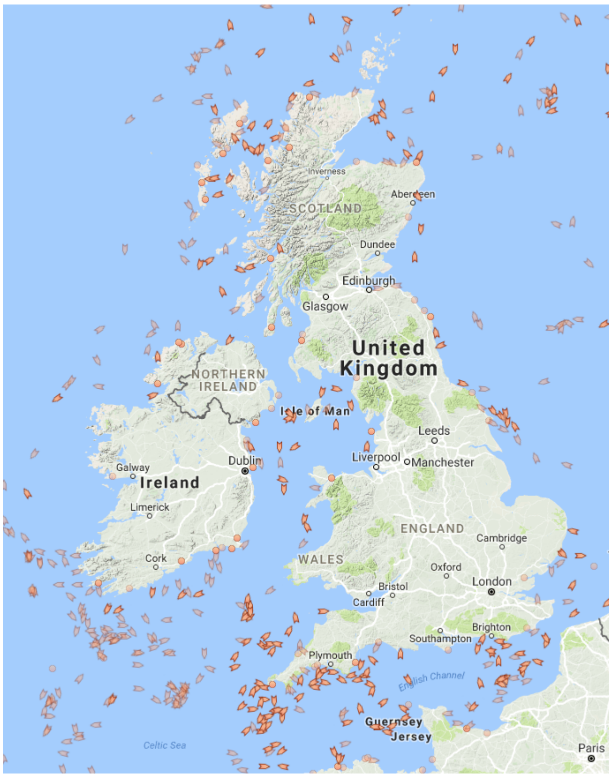

Figure 8.2: Fishing vessels near the UK on 1st March 2018 by MarineTraffic.com (2018)

Fishing remains one of the most dangerous jobs in the world and advances in cost-effective computing technologies can be used in the assessment of vessel stability in this industry. This thesis has presented an SBC coupled with an IMU for estimating a model vessel's roll period and metacentric height. The proposed technologies have been compared with other systems to assess its suitability for measuring vessel motion. By adopting low-cost computing technologies, fishing vessel operators obtain information which can be used to reduce fatality rates and improve safety at sea.

Appendix A

Effects of Changing Welch Method Parameters

Effect of changing the number of data points per segment

Changing the number of data points per segment in each time series, changes the number of periodograms used for averaging. The fewer the number of data points per segment, the more the number of periodograms used for averaging. Figures A.1 - A.10 show the spectra obtained for the x, y, and z time series for a different number of data points per segment between 30 and 300. From the results, it can be seen that the fewer the number of data points per segment, the lower the height of the maximum peak of the spectra, the fewer the peaks detected, and the flatter the spectra.

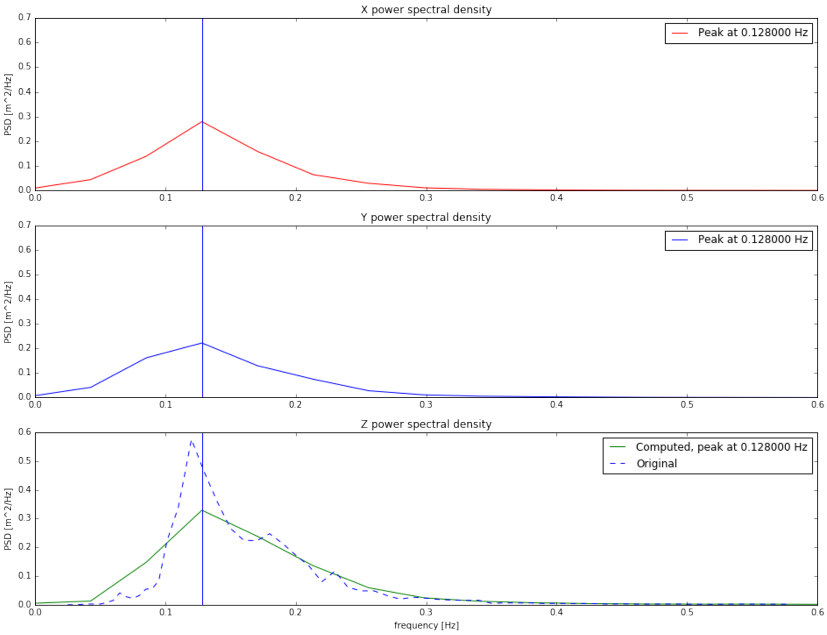

FIGURE A.1: Computed wave spectrum with 30 data points per segment

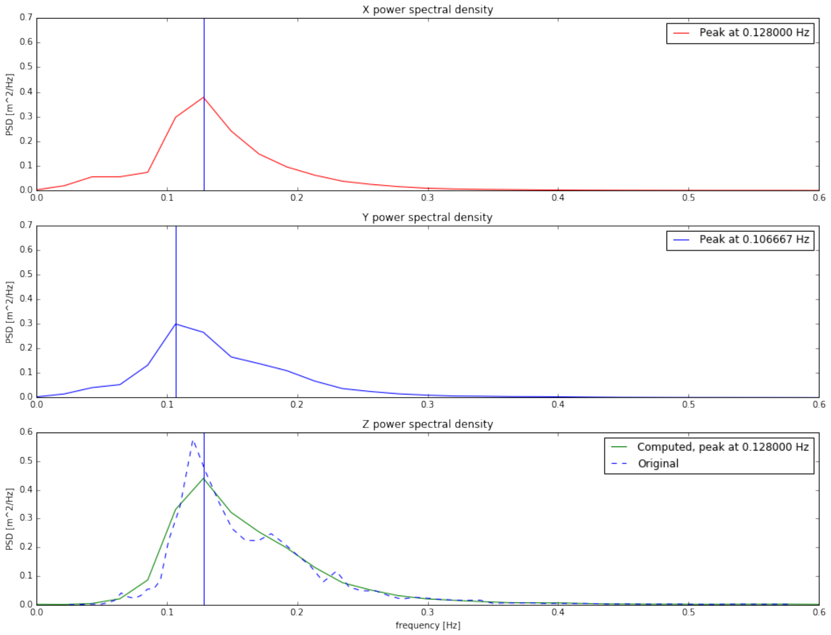

Figure A.2: Computed wave spectrum with 60 data points per segment

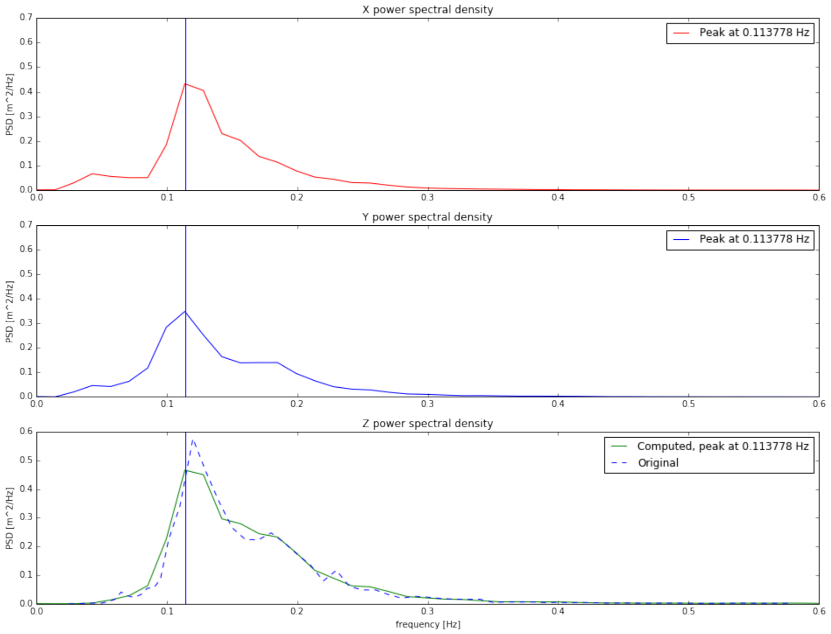

Figure A.3: Computed wave spectrum with 90 data points per segment

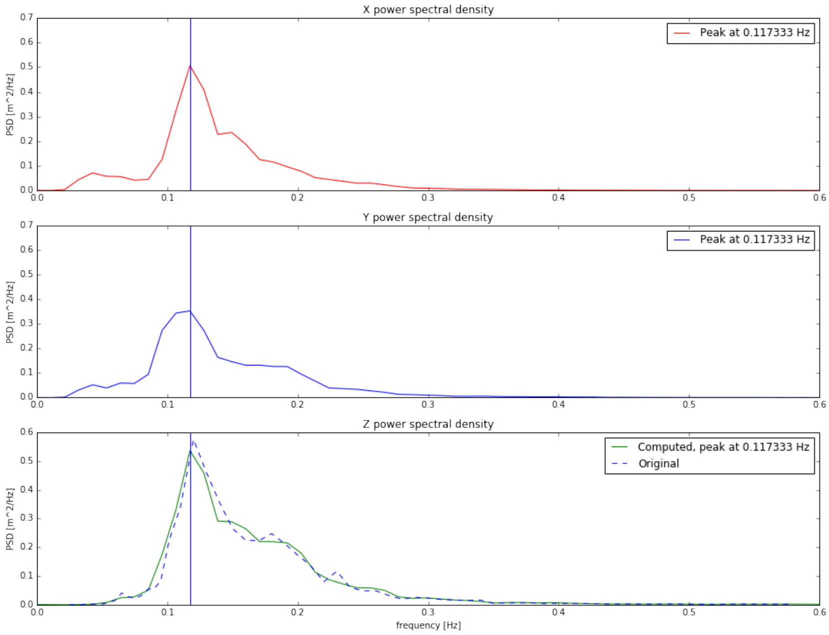

Figure A.4: Computed wave spectrum with 120 data points per segment

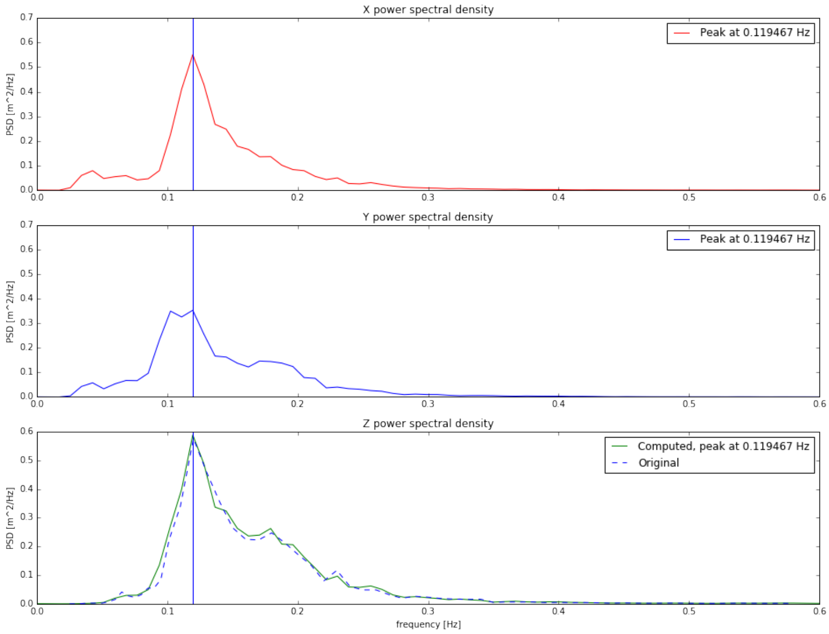

Figure A.5: Computed wave spectrum with 150 data points per segment

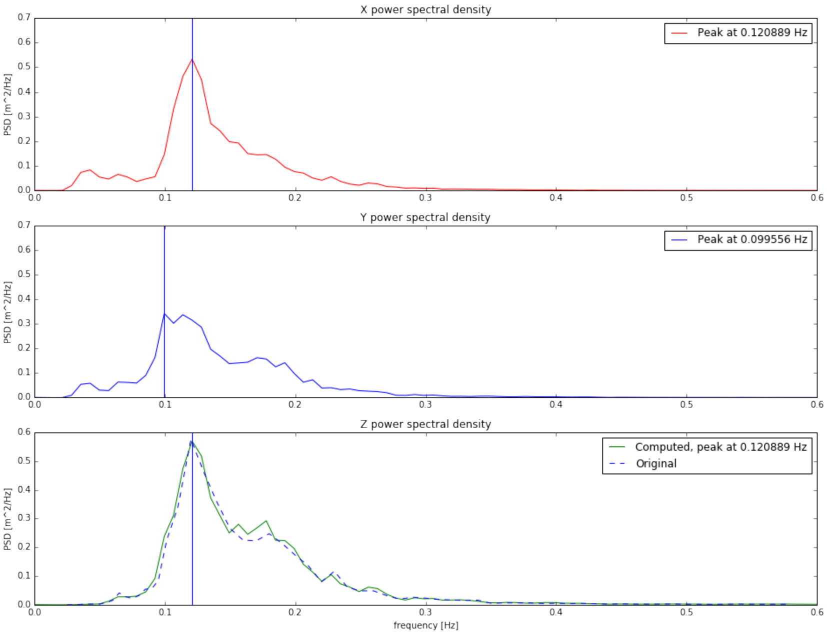

FIGURE A.6: Computed wave spectrum with 180 data points per segment

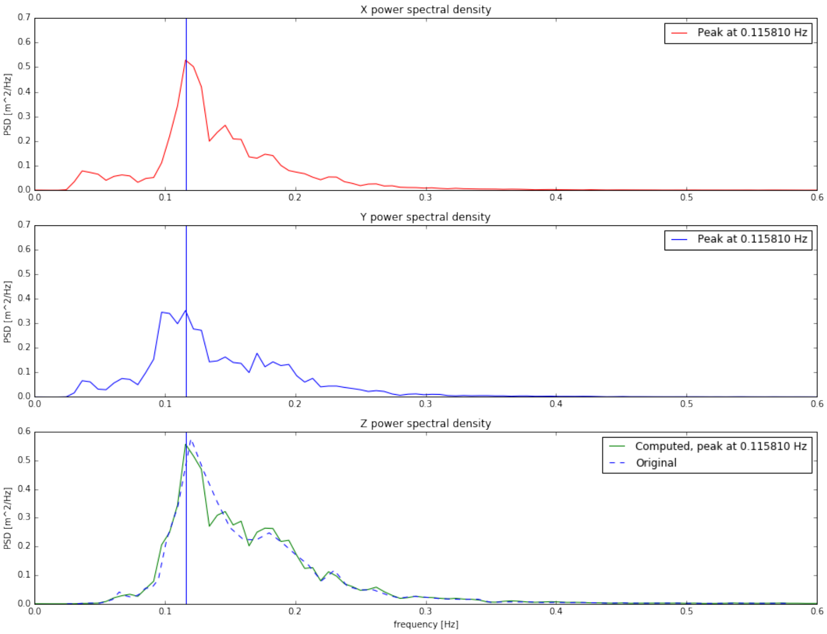

FIGURE A.7: Computed wave spectrum with 210 data points per segment

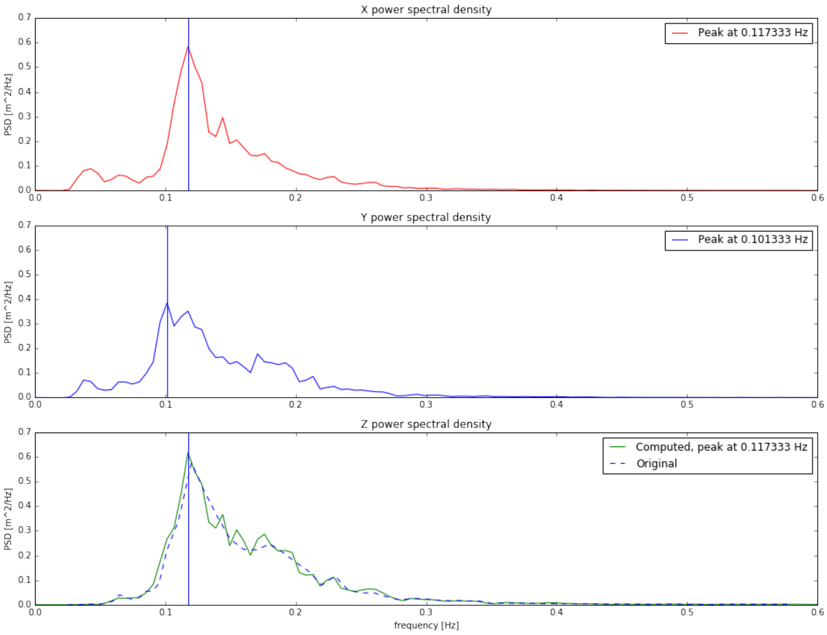

FIGURE A.8: Computed wave spectrum with 240 data points per segment

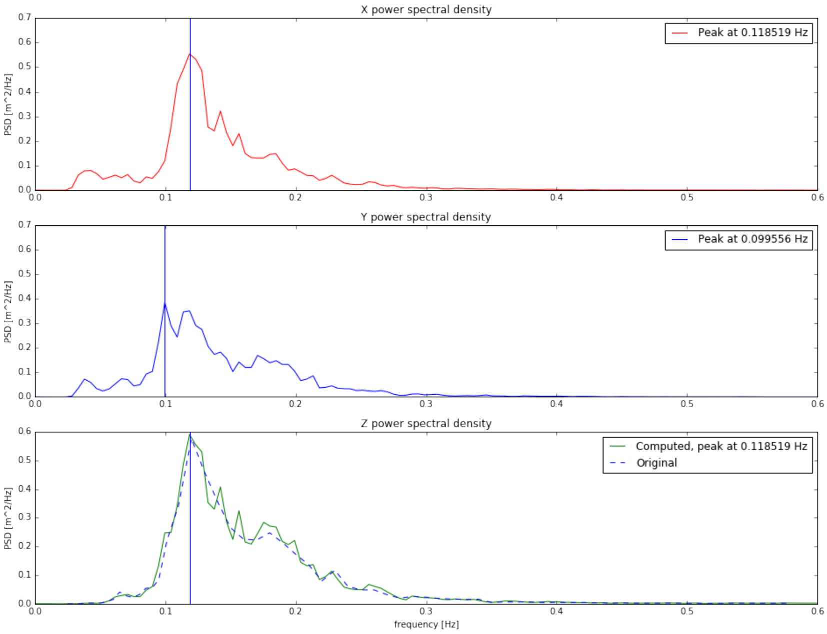

FIGURE A.9: Computed wave spectrum with 270 data points per segment

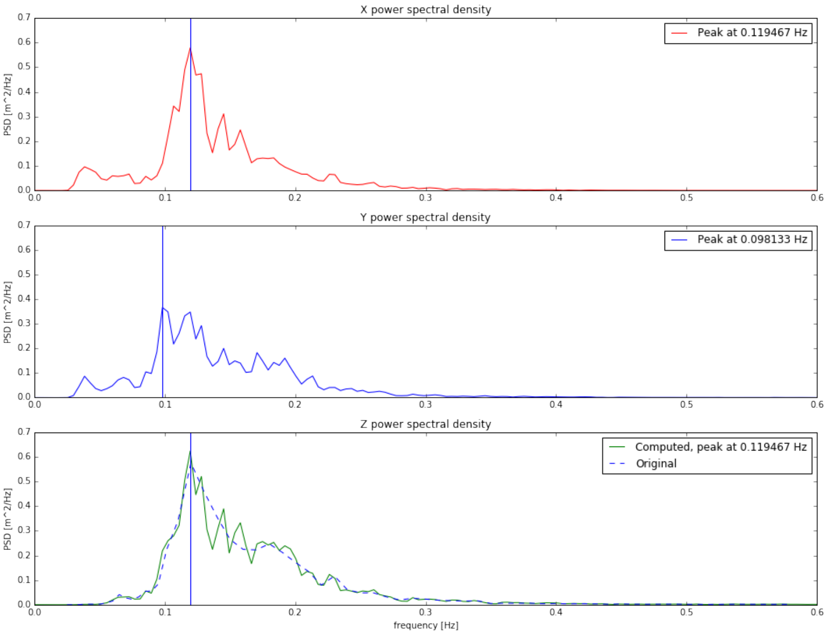

FIGURE A.10: Computed wave spectrum with 300 data points per segment

Effect of changing the window

Windowing functions are used when performing FFT to reduce the effects of spectral leakage. As seen earlier, this is as a result of performing FFT over a non-integer number of cycles. It achieves this by reducing the amplitude of discontinuities at the boundaries of each finite sequence (National Instruments (2015)). A number of different windows were tested, and Figures A.11, A.12, and A.13 show the results when using the Hanning, Barthann and Blackman window. As seen in the figures, the type of window chosen has a minimal effect on the spectra's peak frequency.

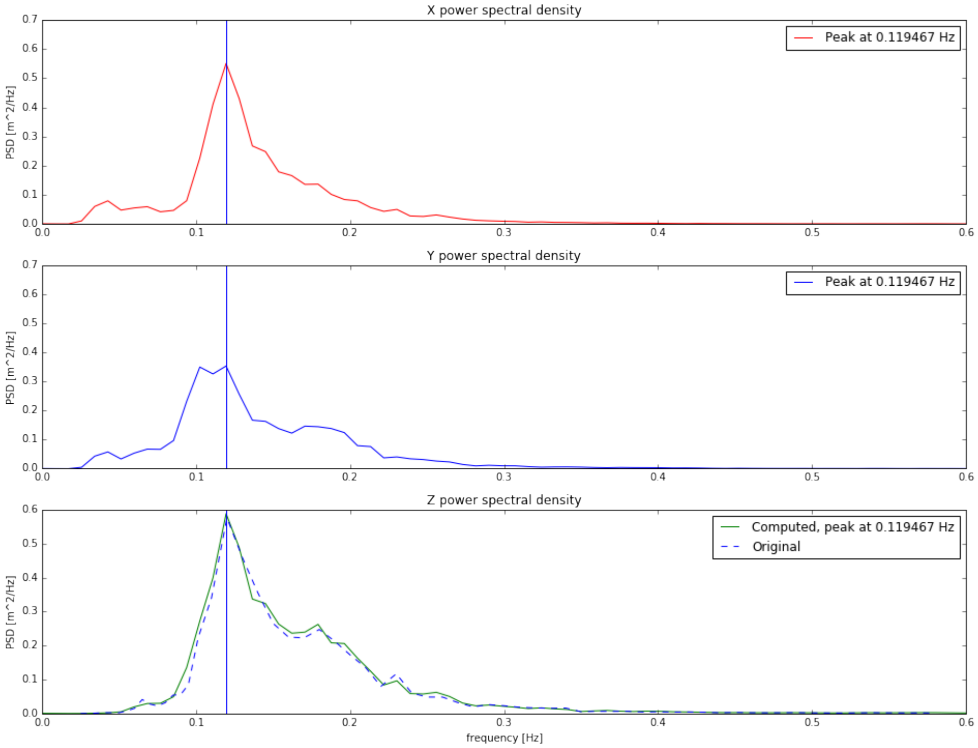

FIGURE A.11: Hanning window

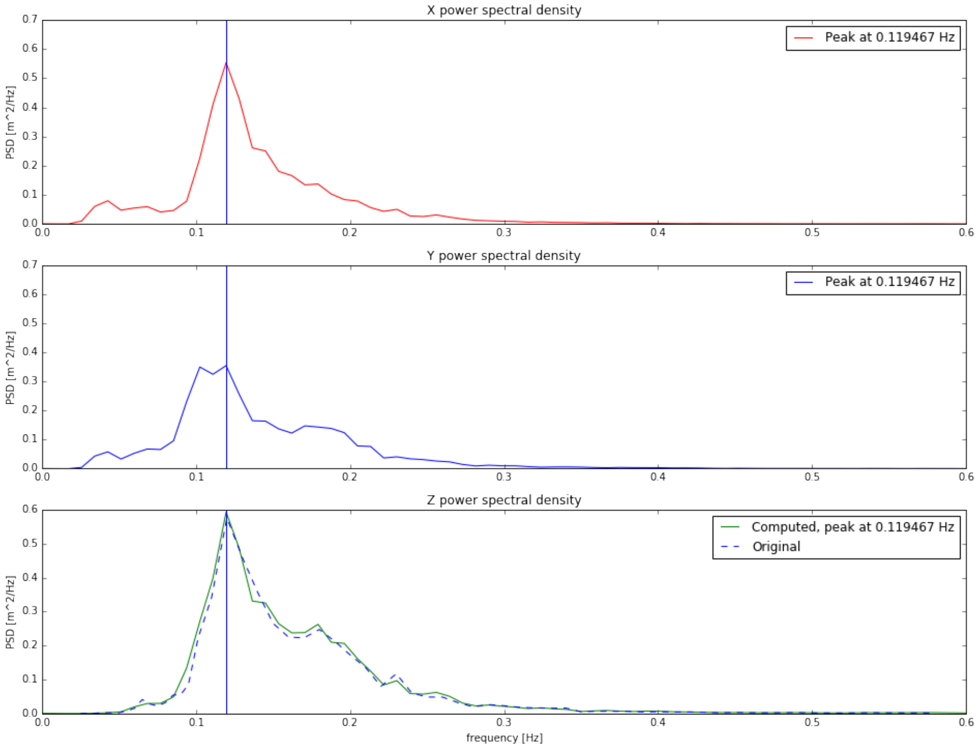

FIGURE A.12: Barthann window

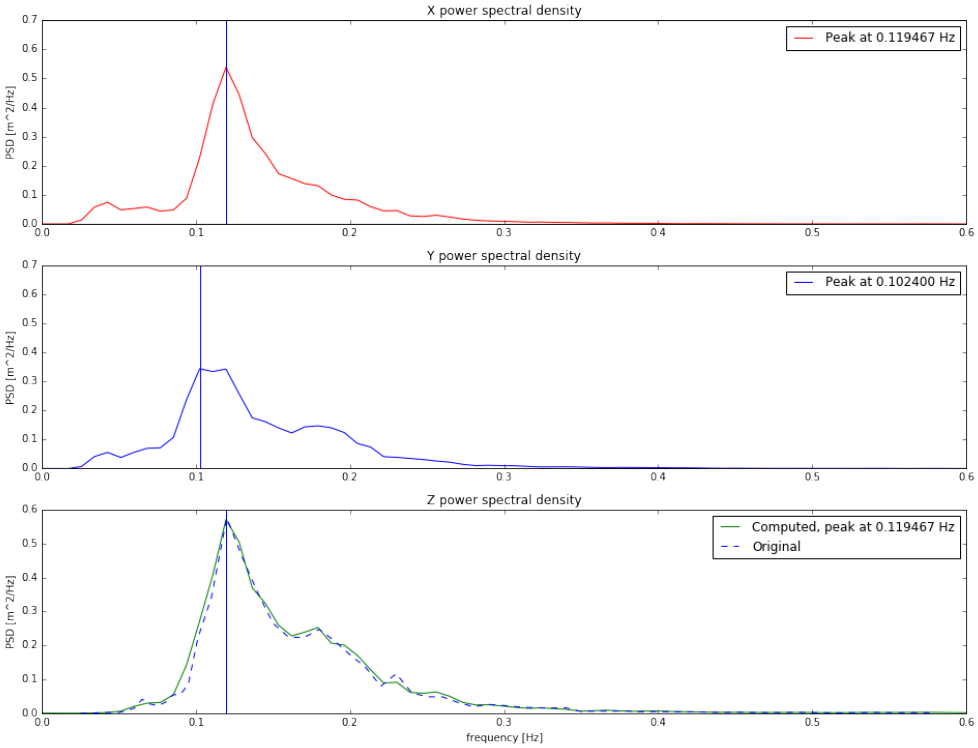

FIGURE A.13: Blackman window

Effect of changing how to detrend each segment

The detrend option specifies how to remove linear trends from the data. If the type of detrending chosen is 'linear', the result of a linear least-squares fit to data is subtracted from data. However if the type of detrending chosen is 'constant', only the mean of data is subtracted (SciPy, 2014). Similar to the type of window chosen, the type of detrending has a minimal effect on the spectra obtained as seen in Figures A.14 and A.15. However considering that pre-processing of the data by the CDIP would have accounted for causes of linear changes in the data such as drift from using a gyroscope, the constant detrending method is recommended.

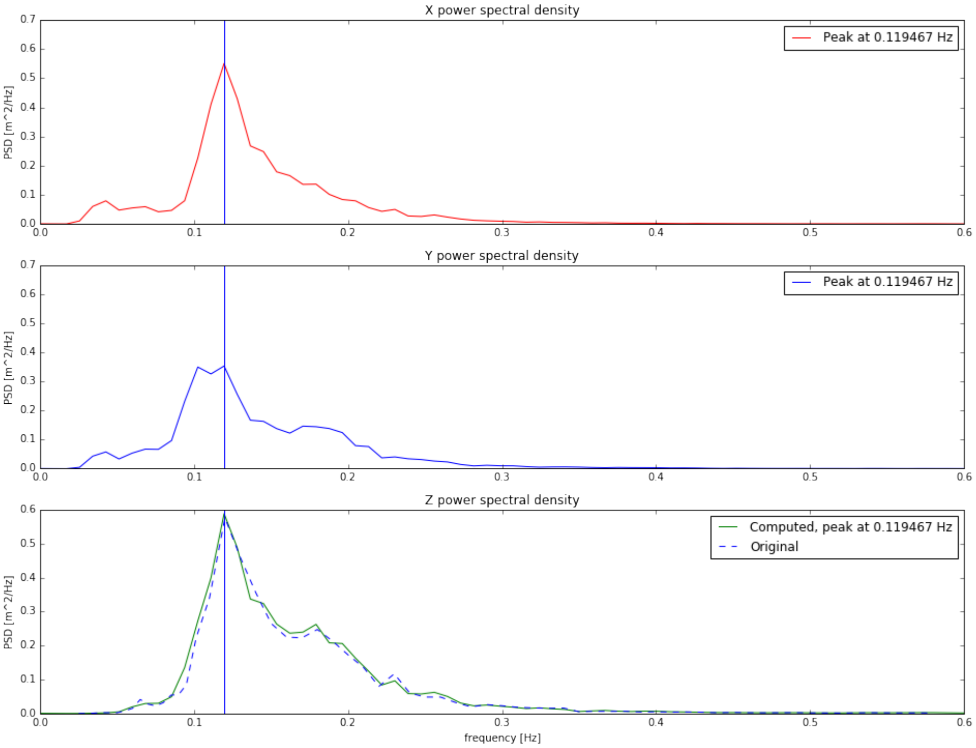

FIGURE A.14: Constant detrending

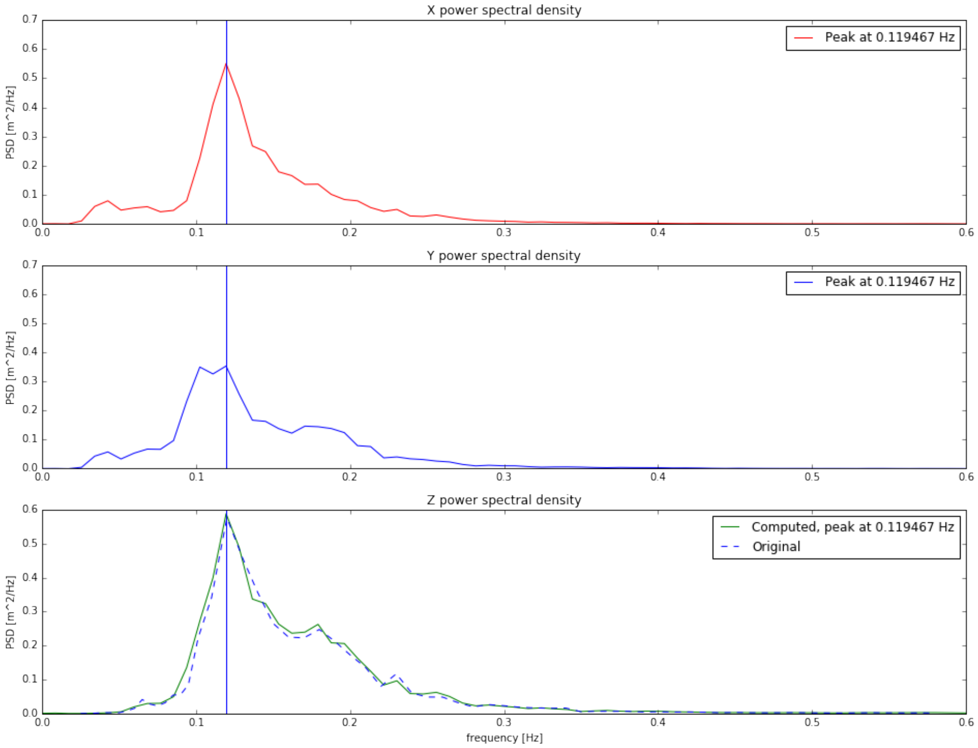

FIGURE A.15: Linear detrending

Appendix B

Python code for potentiometer calibration

```
from __future__ import division
from scipy import signal # Used for converting from time domain to power spectrum
from scipy import stats # Used for computing spectrtal moments
from scipy import interpolate # Used for smoothing graphs
import pandas as pd# Used for data handling and manipulation
import matplotlib.pyplot as plt # Used for plotting spectrum
import matplotlib
import matplotlib.pylab as pylab # Used for increasing size of plot
import numpy as np
import math
import datetime
import random
from tqdm import tqdm

import os
import peakutils

# For low pass filter
from scipy.signal import butter, lfilter, freqz, filtfilt

import statsmodels.api as sm
from statsmodels.sandbox.regression.predstd import wls_prediction_std

import os

import plotly.graph_objs as go
from plotly.offline import download_plotlyjs, init_notebook_mode, plot, iplot
init_notebook_mode(connected=True)
files = [ _pos25.lvm , _pos10.lvm , 0.lvm , _neg10.lvm , _neg25.lvm ]
values = [25, 10, 0, -10, -25]

for i in range(5):
```

```
globals()[ calib_%s  % i] = pd.DataFrame(columns=[ Angle ,  Voltage ])

df = pd.read_csv(”potentiometer/nana2_calib”+files[i], sep= \t , names = list(range(0,2)))
df_data = df[22:]
df_data.columns = df_data.iloc[0]
df_data = df_data[1:]
df_data.ROLL = df_data.ROLL.astype(float)

globals()[ calib_%s  % i].Voltage = df_data.ROLL.values
globals()[ calib_%s  % i].Angle = values[i]

all_calib = pd.concat([calib_0,calib_1,calib_2,calib_3,calib_4])
all_calib = all_calib.reset_index(drop=True)

X = all_calib.Voltage.values
X_with_const = sm.add_constant(X)     # Add intercept term

Y = all_calib.Angle.values

regression = sm.OLS(Y,X_with_const).fit()

print(regression.summary())

results = regression.get_prediction(X_with_const)
y_pred = results.summary_frame()

# PLOTS
trace1 = go.Scatter(x=X,
y=Y,
marker = dict(color=pot_colour),
mode= markers , name= Calibration data )

trace2 = go.Scatter(x=X,
y=y_pred[ mean ], marker = dict(color= blue ),
mode= lines , name= Regression line )

# upper_reg = go.Scatter(x=X,
#                       y=y_pred[ mean_ci_upper ], line = dict(color= blue , dash =  dot ),
#                       mode= lines , name= Regression + SE )

# lower_reg = go.Scatter(x=X,
#                       y=y_pred[ mean_ci_lower ], line = dict(color= blue , dash =  dot ),
#                       mode= lines , name= Regression - SE )

upper_pr = go.Scatter(x=X,
y=y_pred[ obs_ci_upper ],  line = dict(color= lightblue , dash =  dash ),
mode= lines , name= Upper 95% CI )

lower_pr = go.Scatter(x=X,
y=y_pred[ obs_ci_lower ],  line = dict(color= lightblue , dash =  dash ),
mode= lines , name= Lower 95% CI )
```

```
layout = go.Layout(title= Potentiometer Calibration ,
xaxis=dict(title= Voltage [V] ),
yaxis=dict(title= Angle [deg] ))

#data = [trace1, trace2, upper_reg, lower_reg, upper_pr, lower_pr]
data = [trace1, trace2, upper_pr, lower_pr]
fig = go.Figure(data=data, layout=layout)
iplot(fig)
```

Appendix C

Python code for computing roll period

```
from __future__ import division
from scipy import signal # Used for converting from time domain to power spectrum
from scipy import stats # Used for computing spectrtal moments
from scipy import interpolate # Used for smoothing graphs
import pandas as pd# Used for data handling and manipulation
import matplotlib.pyplot as plt # Used for plotting spectrum
import matplotlib
import matplotlib.pylab as pylab # Used for increasing size of plot
import numpy as np
import math
import datetime
import random
from tqdm import tqdm

import os
import peakutils

# For low pass filter
from scipy.signal import butter, lfilter, freqz, filtfilt

# LOW PASS FILTER
def butter_lowpass(cutoff, fs, order=5):
nyq = 0.5 * fs
normal_cutoff = cutoff / nyq
b, a = butter(order, normal_cutoff, btype= low , analog=False)
return b, a

def butter_lowpass_filter(data, cutoff, fs, order=5):
b, a = butter_lowpass(cutoff, fs, order=order)
#y = lfilter(b, a, data) # causal forward-in-time filtering only,
# similar to a real-life electronic filter.
# It can t be zero-phase
```

```
y = filtfilt(b, a, data)
# yfiltfilt is zero-phase filtering, which doesn t shift the signal as it filters.
# Since the phase is zero at all frequencies, it is also linear-phase.
# Filtering backwards in time requires you to predict the future, so it
# can t be used in ”online” real-life applications, only for offline
# processing of recordings of signals.
return y

for navio in [”navio_1”,”navio_2”,”navio_3”,”navio_4”]:
all_files = os.listdir(navio+”/AccelGyroMag”)
subset_files = [file for file in all_files if  lowfreq_test  in file]

results = {}

for i in tqdm(subset_files):
# Read data
# print(”BEGINNING....”, navio, i)
try:
df = pd.read_csv(navio+”/AccelGyroMag/”+i,
sep=” ”, header=None, skiprows=1)
df = df.iloc[100:-100]

# Deal with outliers
df[ (df[9].between(df[9].quantile(.005), df[9].quantile(.995)))] = np.nan
df = df.interpolate(method= linear , limit_direction= both , axis=0)

# Plot before Filter
plt.figure()
pylab.rcParams[ figure.figsize ] = 20, 14  # Length, Height
pylab.rcParams[ font.size ] = 18
plt.subplots_adjust(hspace=.5)

plt.subplot(2,1,1)
plt.plot(df.index,df[3])
plt.title( Accelerometer  +navio+   +i)
plt.xlabel( Time )
plt.ylabel( Acceleration [g] )

plt.subplot(2,1,2)
plt.plot(df.index,df[9])
plt.title( Gyroscope  +navio+   +i)
plt.xlabel( Time )
plt.ylabel( Angular velocity [deg/s] )

plt.savefig(navio+ _ +i+ before_filter.png )
plt.close()

# Find peaks
cb = df[9].values
indexes = peakutils.indexes(cb, thres=0.76, min_dist=100)
```

```
# Filter on peaks, calculate sample rate and times
df_filt = df[indexes[0]:indexes[-1]]
df_filt = df_filt.reset_index()

sample_rate = 1 / pd.to_datetime(df_filt[1]).diff().dt.total_seconds()[1:].mean()

# Time interval between readings
time_interval_sec = 1/sample_rate # in minutes

print(sample_rate, time_interval_sec)

# Create time column using average time_interval and index
df_filt[ Time_sec ]=df_filt.index*time_interval_sec
df_filt[ Time_min ]=df_filt.Time_sec/60

# Make time the index
df_filt.index = pd.DatetimeIndex(df_filt[ Time_sec ]*1000000000)

# Plot before low pass filter
plt.figure()
pylab.rcParams[ figure.figsize ] = 20, 14  # Length, Height
pylab.rcParams[ font.size ] = 18
plt.subplots_adjust(hspace=.5)

plt.subplot(2,1,1)
plt.plot(df_filt.index,df_filt[3])
plt.title( Accelerometer )
plt.xlabel( Time )
plt.ylabel( Acceleration [g] )

plt.subplot(2,1,2)
plt.plot(df_filt.index,df_filt[9])
plt.title( Gyroscope )
plt.xlabel( Time )
plt.ylabel( Angular velocity [deg/s] )

plt.savefig(navio+ _ +i+ before_low_pass.png )
plt.close()

# Low pass filter
df_lp = df_filt.copy()
cut_off = 1.5
ordr = 2

df_lp[3] = butter_lowpass_filter(df_lp[3], cutoff = cut_off, fs = sample_rate, order = ordr)
df_lp[9] = butter_lowpass_filter(df_lp[9], cutoff = cut_off, fs = sample_rate, order = ordr)

# Plot after low pass filter
plt.figure()
pylab.rcParams[ figure.figsize ] = 20, 14  # Length, Height
```

```
pylab.rcParams[ font.size ] = 18
plt.subplots_adjust(hspace=.5)

plt.subplot(2,1,1)
plt.plot(df_lp.index,df_lp[3])
plt.title( Accelerometer )
plt.xlabel( Time )
plt.ylabel( Acceleration [g] )

plt.subplot(2,1,2)
plt.plot(df_lp.index,df_lp[9])
plt.title( Gyroscope )
plt.xlabel( Time )
plt.ylabel( Angular velocity [deg/s] )

plt.savefig(navio+ _ +i+ after_low_pass.png )
plt.close()

# Find peak
# Peak calculated every  analysis_time  seconds
analysis_time = 300
num_points = analysis_time*sample_rate
num_chuncks = math.floor(len(df_lp)/num_points)

div = 2 # Divide analysis segment by

f_welch_acc, P_welch_acc = signal.welch(df_lp[3],
fs=sample_rate,
nperseg=num_points/div)
peak_acc = f_welch_acc[P_welch_acc.argmax()]


f_welch_gyro, P_welch_gyro = signal.welch(df_lp[9],
fs=sample_rate,
nperseg=num_points/div)
peak_gyro = f_welch_gyro[P_welch_gyro.argmax()]

plt.figure()
pylab.rcParams[ figure.figsize ] = 20, 14  # Length, Height
pylab.rcParams[ font.size ] = 18
plt.subplots_adjust(hspace=.5)

plt.subplot(2,1,1)
plt.plot(f_welch_acc, P_welch_acc,  *- ,label=”Peak at %0.5f Hz” %peak_acc)
plt.axvline(peak_acc)
plt.title( Accelerometer )
plt.xlim([0, 1.0])
plt.xlabel(r $\mathrm{Frequency\ [Hz]}$ )
plt.ylabel(r $\mathrm{PSD\ [g^2/Hz]}$ )
plt.legend()
```

```
plt.subplot(2,1,2)
plt.plot(f_welch_gyro, P_welch_gyro, *- ,label=”Peak at %0.5f Hz” %peak_gyro)
plt.axvline(peak_gyro)
plt.title( Gyroscope )
plt.xlim([0, 1.0])
plt.xlabel(r $\mathrm{Frequency\ [Hz]}$ )
plt.ylabel(r $\mathrm{PSD\ [deg^2/s]}$ )
plt.legend()

plt.savefig(navio+ _ +i+ peak.png )
plt.close()

results[i] = peak_gyro
except:
print(”Could not process ”, navio, i)

results_pdf = pd.DataFrame(list(results.items()),columns = [ file , peak_frequency ])
results_pdf[ navio ] = navio
results_pdf.to_csv(navio+ _low_freq_test.csv , index=False)

results_1 = pd.read_csv( navio_1_low_freq_test.csv )
for col in results_1.columns:
results_1 = results_1.rename(columns={col:col+ _1 })

results_2 = pd.read_csv( navio_2_low_freq_test.csv )
for col in results_2.columns:
results_2 = results_2.rename(columns={col:col+ _2 })

results_3 = pd.read_csv( navio_3_low_freq_test.csv )
for col in results_3.columns:
results_3 = results_3.rename(columns={col:col+ _3 })

results_4 = pd.read_csv( navio_4_low_freq_test.csv )
for col in results_4.columns:
results_4 = results_4.rename(columns={col:col+ _4 })

all_results = results_1.merge(results_2, left_index=True, right_index=True)
all_results = all_results.merge(results_3, left_index=True, right_index=True)
all_results = all_results.merge(results_4, left_index=True, right_index=True)

for i in [ peak_frequency_1 , peak_frequency_2 , peak_frequency_3 , peak_frequency_4 ]:
all_results[ peak_period +i[-2:]] = 1/all_results[i]

all_results = all_results[1:]
all_results = all_results.sort_values( peak_frequency_1 , ascending=False)
all_results = all_results.reset_index()
all_results.index = all_results.index + 1

all_results[[ peak_frequency_1 ,
 peak_frequency_2 ,
 peak_frequency_3 ,
```

```
 peak_frequency_4  ,]]

# all_results[[ peak_frequency_1  , file_1  ,
#               peak_frequency_2  , file_2  ,
#               peak_frequency_3  , file_3  ,
#               peak_frequency_4  , file_4  ]]
```

Bibliography

Abankwa, N. O., Squicciarini, G., Johnston, S. J., Scott, M., and Cox, S. J. An evaluation of the use of low-cost accelerometers in assessing fishing vessel stability through period of heave motion. In *2016 International Conference for Students on Applied Engineering (ICSAE)*, pages 59–63, Newcastle upon Tyne, UK, 20 - 21 Oct 2016. doi:10.1109/ICSAE.2016.7810161.

Al-Rawashdeh, Y. M., Elshafei, M., and Al-Malki, M. F. In-flight estimation of center of gravity position using all-accelerometers. *Sensors*, 14(9):17567–17585, 2014. doi:10.3390/s140917567.

Ali, M., Vlaskamp, J. H. A., Eddin, N. N., Falconer, B., and Oram, C. Technical development and socioeconomic implications of the Raspberry Pi as a learning tool in developing countries. In *2013 5th Computer Science and Electronic Engineering Conference (CEEC)*, pages 103–108, Colchester, UK, 17 - 18 Sept 2013. doi:10.1109/CEEC.2013.6659454.

Amazon. *SanDisk Extreme PRO 64GB SDXC Memory Card up to 170MB/s, UHS-1, Class 10, U3, V30*, 2019a. URL https://www.amazon.co.uk/SanDisk-Extreme-SDXC-Memory-Class/dp/B07H9J1YXN/ref=sr_1_3?adgrpid=55670976840&dchild=1&gclid=EAIaIQobChMIsJ7gt4DD8AIVzYKDBx3JJgKeEAAYASAAEgJVT_D_BwE&hvadid=259048229164&hvdev=c&hvlocphy=9044965&hvnetw=g&hvqmt=e&hvrand=15619423278371308912&hvtargid=kwd-300561881172&hydadcr=5060_1827832&keywords=sd+64gb+memory+card&qid=1620783343&sr=8-3. [Online; accessed 9 April 2021].

Amazon. *125mm x 125mm x 100mm Waterproof Dustproof IP65 Junction Box DIY Case Enclosure Gray*, 2019b. URL https://www.amazon.co.uk/gp/product/B06ZY2XPG5/ref=ppx_od_dt_b_asin_title_s01?ie=UTF8&psc=1. [Online; accessed 9 April 2018].

Anker. *Anker PowerCore 10000 - The Compact High-Capacity Portable Charger*, 2019. URL https://www.anker.com/store/powercore-10000/A1263011. [Online; accessed 9 April 2018].

Aronica, S., Fontana, I., Giacalone, G., Basilone, G., Langiu, A., Gattuta, L. L., Pulizzi, M., Genovese, S., Mangano, S., Calandrino, P., Mazzola, S., and Bonanno, A. iSAFETY - Integrated System for an Automatic Support to Fishing Vessel Security. In *Intelligent Systems Conference*, London, UK, 7 - 8 September 2017. doi:10.1109/IntelliSys.2017.8324305.

Banos, O., Toth, M. A., Damas, M., Pomares, H., and Rojas, I. Dealing with the effects of sensor displacement in wearable activity recognition. *Sensors*, 14(6):9995–10023, 2014. doi:10.3390/s140609995.

Barrass, B. and Derrett, D. R. Chapter 6: Transverse statical stability. In *Ship stability for masters and mates*, pages 44–50. Elsevier, 6th edition, 2006. doi:10.1016/B978-075066784-5/50008-3.

Bartlett, M. S. Periodogram analysis and continuous spectra. *Biometrika*, 37(1):1–16, 1950. doi:10.2307/2332141.

Basford, P. J., Bragg, G. M., Hare, J. S., Jewell, M. O., Martinez, K., Newman, D. R., Pau, R., Smith, A., and Ward, T. Erica the rhino: A case study in using raspberry pi single board computers for interactive art. *Electronics*, 5(3), 2016. doi:10.3390/electronics5030035.

Beck, R. and Reed, A. Modern seakeeping computations for ships. In *Twenty-Third Symposium on Naval Hydrodynamics*, pages 1–45, Val de Reuil, France, 17 - 22 September 2000. National Academy Press. URL https://www.nap.edu/read/10189/chapter/2.

Bennett, S., Brooks, C., Winden, B., Taunton, D., Forrester, A., Turnock, S., and Hudson, D. Measurement of ship hydroelastic response using multiple wireless sensor nodes. *Ocean Engineering*, 79:67 – 80, 2014. doi:10.1016/j.oceaneng.2013.12.011.

Bockmann, E. and Steen, S. Model test and simulation of a ship with wavefoils. *Applied Ocean Research*, 57:8 – 18, 2016. doi:https://doi.org/10.1016/j.apor.2016.02.002.

Borghese, N. A. and Cerveri, P. Calibrating a video camera pair with a rigid bar. *Pattern Recognition*, 33(1):81 – 95, 2000. doi:10.1016/S0031-3203(99)00033-3.

Bouguer, P. *Traité du navire, de sa construction et de ses mouvemens*. Jombert, 1746.

Bowker, J., Townsend, N., Tan, M.-Y., and Shenoi, A. Experimental analysis of submerged flapping foils; implications for autonomous surface vehicles (asvs). In *OCEANS 2016 MTS/IEEE Monterey*. IEEE, December 2016. doi:10.1109/OCEANS.2016.7761324).

British Broadcasting Corporation. *The most dangerous job in the UK*, 2010. URL http://www.bbc.co.uk/news/uk-10923190. [Online; accessed 22 February 2018].

Burckle, R. A. *The Evolution of Single Board Computers*. Technical report, WinSystems, Inc. URL https://connectedworld.com/wp-content/uploads/2014/07/Whitepaper_WinSystems_TheEvolutionOfSingleBoardComputers.pdf. [Online; accessed 2 June 2018].

Business Insider Intelligence. *The Internet of Everything*, 2015. URL https://intelligence.businessinsider.com. [Online; accessed 3 June 2018].

Cerna, M. and Harvey, A. *The Fundamentals of FFT-Based Signal Analysis and Measurement*. Application Note 041, National Instruments, 2000. URL http://www.iaa.ncku.edu.tw/~jjmiau/download/FFTAnalysis.pdf. [Online; accessed 1 March 2018].

Chakraborty, S. *Ship Stability: Understanding Curves of Static Stability*, 2017a. URL https://www.marineinsight.com/naval-architecture/ship-stability-understanding-curves-static-stability/. [Online; accessed 10 March 2018].

Chakraborty, S. *Ship Stability: Intact Stability Criteria and Inclining Experiment*, 2017b. URL https://www.marineinsight.com/naval-architecture/ship-stability-intact-stability-criteria-and-inclining-experiment/. [Online; accessed 10 March 2018].

Chauvin, C., Le Bouar, G., and Lardjane, S. Analysis of occupational injuries in the sea fishing industry according to the type of fishery and the fishing activity. *International Maritime Health*, 68(1):31–38, 2017. doi:10.5603/IMH.2017.0006.

Coastal Data Information Program. *Masonboro Inlet*, 2015. URL http://cdip.ucsd.edu. [Online; accessed 21 May 2018].

Comstock, J. *Principles of Naval Architecture.* New York: Society of Naval Architects and Marine Engineers, 1967. ISBN 9-9974-6255-6.

Cox, S. J., Cox, J. T., Boardman, R. P., Johnston, S. J., Scott, M., and O'Brien, N. S. Iridis-pi: a low-cost, compact demonstration cluster. *Cluster Computing*, 17(2):349–358, 2014. doi:10.1007/s10586-013-0282-7.

Critzos, C. C., Heyson, H. H., and Boswinkle, R. W. *Aerodynamic Characteristics of NACA 0012 Airfoil Section at Angles of Attack from 0 to 180 degrees.* Technical note 3361, National Advisory Committee for Aeronautics, 1955. URL http://www.dtic.mil/dtic/tr/fulltext/u2/a377080.pdf. [Online; accessed 1 March 2018].

Dallinga, R., Blok, J., and H.R, L. Excessive rolling of cruise ships in head and following waves. In *International Conference on Ship Motions and Manoeuvring, RINA*, 1997.

Data Physics Corporation. *SignalCalc Ace - Ultra-Portable, Cost-Effective, Dynamic Signal Analysers*, 2016a. URL http://www.dataphysics.com/gb/products-and-solutions/dynamic-signal-analyzers-signalcalc/signalcalc-ace.html. [Online; accessed 3 June 2018].

Data Physics Corporation. *SignalCalc Software*, 2016b. URL http://www.dataphysics.com/gb/products-and-solutions/dynamic-signal-analyzers-signalcalc/signalcalc-software.html. [Online; accessed 3 June 2018].

Dell. *Latitude E6430 Premier Laptop*, 2013. URL https://www.dell.com/en-uk/work/shop/laptops/dell-latitude-e6430-premier-laptop/spd/latitude-e6430. [Online; accessed 3 June 2018].

Dimension Engineering. *A beginner's guide to accelerometers*, 2014. URL http://www.dimensionengineering.com/info/accelerometers. [Online; accessed 3 December 2015].

Ding, H., Trajcevski, G., Scheuermann, P., Wang, X., and Keogh, E. Querying and mining of time series data: Experimental comparison of representations and distance measures. *Proc. VLDB Endow.*, 1(2):1542–1552, August 2008. doi:10.14778/1454159.1454226.

Earle, M. D. *Nondirectional and Directional Wave Data Analysis Procedures*. NDBC Technical Document 96 - 01, National Oceanic and Atmospheric Administration, 1996. URL http://www.ndbc.noaa.gov/wavemeas.pdf. [Online; accessed 3 June 2018].

Emery, W. J. and Thomson, R. E. Chapter 5 - Time-series Analysis Methods. In *Data Analysis Methods in Physical Oceanography*, pages 371 – 567. Elsevier Science, Amsterdam, 2001. ISBN 978-0-4445-0756-3. doi:10.1016/B978-044450756-3/50006-X.

Emlid. *Navio2 - Linux autopilot on Raspberry Pi*, 2018. URL https://emlid.com/navio/. [Online; accessed 3 June 2018].

Emlid. *C++ and Python sensor examples for developers*, 2019a. URL https://github.com/emlid/Navio2. [Online; accessed 9 April 2018].

Emlid. *Navio2 Hardware setup*, 2019b. URL https://docs.emlid.com/navio2/ardupilot/hardware-setup/. [Online; accessed 10 November 2019].

Enshaei, H. *Prevention of extreme roll motions through measurements of ship's motion responses*. PhD thesis, Newcastle University, 2013.

Farnell Element 4. *Xsens MTi 10 series motion tracking system*, 2016. URL http://uk.farnell.com/xsens-mti-10-series. [Online; accessed 3 June 2018].

Faugeras, O. *Three-Dimensional Computer Vision: A Geometric Viewpoint.* MIT Press, 1994. ISBN 0-2620-6158-9.

Faux, D. A. and Godolphin, J. Manual timing in physics experiments: Error and uncertainty. *American Journal of Physics*, 87(2):110–115, 2019. doi:10.1119/1.5085437. URL https://doi.org/10.1119/1.5085437.

Ferrier, B. and Manning, T. Simulation and testing of the landing period designator (LPD) helicopter recovery aid. *Naval Engineers Journal*, 112(4), 1998. doi:10.1111/j.1559-3584.1998.tb02396.x.

Fornasini, P. *The Uncertainty in Physical Measurement: An Introduction to Data Analysis in the Physics Laboratory.* Springer, 2008. doi:10.1007/978-0-387-78650-6.

Fraden, J. *Handbook of Modern Sensors. Physics, Designs, and Applications.* Springer, 4th edition, 2010. ISBN 978-1-4419-6465-6.

Garcia, R. F., Antonio, C., and Ameal, F. Ship stability monitoring by motion frequency analysis. *IFAC Proceedings Volumes*, 34(7):39 – 43, 2001. doi:https://doi.org/10.1016/S1474-6670(17)35056-5.

Gelin, C. *Motion Observation and Experimental Results*, pages 37–60. Springer Berlin Heidelberg, Berlin, Heidelberg, 2013. ISBN 978-3-642-32015-6.

Gomez, A., Cuinas, D., Catala, P., Xin, L., Li, W., Conway, S., and Lack, D. Use of single board computers as smart sensors in the manufacturing industry. *Procedia Engineering*, 132:153 – 159, 2015. doi:https://doi.org/10.1016/j.proeng.2015.12.461.

Gonzalez, M. M., Sobrino, P. C., Alvarez, R. T., Casas, V. D., Lopez, A. M., and Pena, F. L. Fishing vessel stability assessment system. *Ocean Engineering*, 41:67 – 78, 2012. doi:10.1016/j.oceaneng.2011.12.021.

Gonzalez, M. M., Casas, V. D., and Caamano, L. S. Real-time stability assessment in mid-sized fishing vessels. In *Proceedings of the 15th International Ship Stability Workshop*, Stockholm, Sweden, 13 - 15 June 2016.

Grayson, D. E. *MinIMU9 - AHRS*, 2014. URL https://github.com/DavidEGrayson/minimu9-ahrs. [Online; accessed 3 June 2018].

Gudmundsson, A. *Safety practices related to small fishing vessel stability.* Technical paper 517, Food and Agriculture Organization, 2009. URL http://www.fao.org/docrep/011/i0625e/i0625e00.htm. [Online; accessed 1 March 2018].

Herder, J. L. and Schwab, A. L. On dynamically equivalent force systems and their application to the balancing of a broom or the stability of a shoe box. In *Proceedings of DETC'04 ASME Design Engineering Technical Conferences and Computers and Information in Engineering Conference*, New York, USA, 2004. doi:10.1115/DETC2004-57188.

Holdowsky, J., Mahto, M., Raynor, M. E., and Cotteleer, M. *Inside the Internet of Things (IoT).* Technical report, Deloitte, 2015. URL https://www2.deloitte.com/content/dam/insights/us/articles/iot-primer-iot-technologies-applications/DUP_1102_InsideTheInternetOfThings.pdf. [Online; accessed 13 April 2018].

Hoppe Marine. *Dynamic Floating Monitoring*, 2018. URL http://www.hoppe-marine.com/?q=en/node/19. [Online; accessed 24 May 2018].

Hosseini, S. H. S. *CFD prediction of ship capsize: parametric rolling, broaching, surf-riding, and periodic motions.* PhD thesis, University of Iowa, 2009.

Hudspeth, R. T., Mazenot, F., Carter, W. G., and Gentle, T. H. *Using the Rolling-Period Test To Estimate Fishing Vessel Stability*, 2004. URL https://ir.library.oregonstate.edu/downloads/0r967460r. [Online; accessed 7 March 2018].

Ibrahim, R. and Grace, I. Modeling of ship roll dynamics and its coupling with heave and pitch. *Mathematical Problems in Engineering*, 2010. doi:10.1155/2010/934714.

Igor, S. *How to work with I2C communication in Raspberry Pi.* Technical report, RadioStudio, 2018. URL https://radiostud.io/howto-i2c-communication-rpi/. [Online; accessed 2 June 2019].

International Maritime Organization. *International Code on Intact Stability.* IMO, September 2009. ISBN 978-9-2801-1506-2.

International Maritime Organization (IMO), Food and Agriculture Organization of the United Nations (FAO), and International Labour Organization (ILO). *Safety Recommendations for Decked Fishing Vessels of Less than 12 metres in Length and Undecked Fishing Vessels.* FAO, 2012. ISBN 978-9-2510-7397-1.

InvenSense. *MPU-9250 Nine-Axis (Gyro + Accelerometer + Compass) MEMS MotionTracking Device*, 2016. URL https://www.invensense.com/products/motion-tracking/9-axis/mpu-9250/. [Online; accessed 3 June 2018].

Islam, M., Jahra, F., and Hiscock, S. Data analysis methodologies for hydrodynamic experiments in waves. *Journal of Naval Architecture and Marine Engineering*, 13:1, 06 2016. doi:10.3329/jname.v13i1.25347.

ITTC Specialist Committee on Stability. *Final Report and Recommendations to the 22nd ITTC.* Technical paper, International Towing Tank Conference, 1999. URL https://ittc.info/media/1512/specialist-committee-on-stability.pdf. [Online; accessed 1 March 2018].

Jackson, K. *Optical vs. Inertial Motion Capture*, 2017. URL https://www.gearssports.com/optical-vs-inertial-motion-capture/. [Online; accessed 3 June 2018].

Jiao, J., Ren, H., Adenya, C. A., and Chen, C. Development of a Shipboard Remote Control and Telemetry Experimental System for Large-Scale Model's Motions and Loads Measurement in Realistic Sea Waves. *Sensors*, 17(11), 2017. doi:10.3390/s17112485.

Johnson, M. C. and Wilson, P. A. Sea state estimated from ship motions by a statistical approach. *Transactions of The Royal Institution of Naval Architects Part A: International Journal of Maritime Engineering*, pages 35–51, 2005. doi:10.3940/rina.ijme.2005.a1.050161.

Johnston, S., Apetroaie-Cristea, M., Scott, M., and Cox, S. IoT Applications. In *Internet of Things. Principles and Paradigms*, chapter 15, pages 277–297. Elsevier, Cambridge, 2016. ISBN 978-0-1280-5395-9.

Karolius, K. B. and Vassalos, D. Tearing down the wall - the inclining experiment. *Ocean Engineering*, (148):442–475, 2018a. doi:10.1016/j.oceaneng.2017.11.037.

Karolius, K. B. and Vassalos, D. Tearing down the wall – the inclining experiment. *Ocean Engineering*, 148:442 – 475, 2018b. doi:10.1016/j.oceaneng.2017.11.037.

Kat, J. O. and Paulling, J. R. Prediction of extreme motions and capsizing of ships and offshore marine vehicles. In *Proceedings of the 20th International Conference on Offshore Mechanics and Arctic Engineering (OMAE)*, Rio de Janeiro, Brazil, 3 - 8 June 2001.

Koning, J. *Lashing at Sea - Executive Summay*, 2009. URL http://www.marin.nl/web/JIPs-Networks/Archive-JIPs-public/Lashingsea.htm. [Online; accessed 7 November 2015].

Krishna, P. R. A. and Andrews, J. PSD Computation using modified Welch algorithm. *International Journal of Scientific Research Engineering and Technology (IJSRET)*, 4(9), September 2015.

Lane, D. M. *Introduction to Statistics: An Interactive e-Book*, 2013. URL https://itunes.apple.com/us/book/introduction-to-statistics/id684001500?mt=11. [Online; accessed 9 January 2018].

Levadou, M. and Gaillarde, G. Operational guidance to avoid parametric roll. In *RINA Conference on Designa dn Operation of Container Ships*, pages 75–86, London, United Kingdom, 2003.

Liu, H., Holt, C., and Evans, S. Accuracy and repeatability of an optical motion analysis system for measuring small deformations of biological tissues. *Journal of Biomechanics*, 40(1):210 – 214, 2007. doi:10.1016/j.jbiomech.2005.11.007.

Liu, S., Xing, B., Li, B., and Gu, M. Ship information system: overview and research trends. *International Journal of Naval Architecture and Ocean Engineering (IJNAOE)*, 6:670 – 684, 2014. doi:10.2478/IJNAOE-2013-0204.

Lyons, R. Reducing FFT Scalloping Loss Errors Without Multiplication. In *IEEE Signal Processing Magazine*, March 2011. doi:10.1109/MSP.2010.939845.

Madgwick, S. O. H., Harrison, A. J. L., and Vaidyanathan, R. Estimation of imu and marg orientation using a gradient descent algorithm. In *2011 IEEE International Conference on Rehabilitation Robotics*, pages 1–7, June 2011. doi:10.1109/ICORR.2011.5975346.

Marine Accident Investigation Branch. *MAIB Analysis of UK Fishing Vessel Safety 1992 to 2006*, 2008. URL https://www.gov.uk/government/uploads/system/uploads/attachment_data/file/377352/FishingVesselSafetyStudy.pdf. [Online; accessed 22 February 2018].

Marine Accident Investigation Branch. *MAIB Annual Report 2016*, 2017. URL https://www.gov.uk/government/uploads/system/uploads/attachment_data/file/634809/MAIB_AnnualReport2016.pdf. [Online; accessed 28 May 2018].

Marine Management Organisation. *UK Sea Fisheries Statistics 2016*, 2017. URL https://www.gov.uk/government/uploads/system/uploads/attachment_data/file/647482/UK_Sea_Fisheries_Statistics_2016_Full_report.pdf. [Online; accessed 22 February 2018].

MarineTraffic.com. *Live Map*, 2018. URL https://www.marinetraffic.com/en/ais/home/centerx:-3.9/centery:54.8/zoom:6. [Online; accessed 1 March 2018].

Maritime and Coastguard Agency. *MGN 427 - Stability Guidance for Fishing Vessels of under 15m Overall Length*, 2010. URL https://www.gov.uk/government/publications/mgn-427-stability-guidance-for-fishing-vessels-under-15m. [Online; accessed 27 February 2018].

Maritime and Coastguard Agency. *Procedure for carrying out a roll or heel test to assess stability for fishing vessel owners and skippers*, 2014. URL https://www.gov.uk/government/uploads/system/uploads/attachment_data/file/243952/draft-guidance-note.pdf. [Online; accessed 3 June 2018].

Maritime New Zealand. *A guide to fishing vessel safety*, 2011. URL https://www.maritimenz.govt.nz/commercial/safety/vessel-stability/documents/fishing-vessel-stability-guidelines.pdf. [Online; accessed 1 June 2018].

Maritime Research Institute Netherlands. *Motion monitoring*, 2012. URL http://www.marin.nl/web/Research-Topics/Offshore-operations/Motion-monitoring.htm. [Online; accessed 3 June 2018].

Maul, G. A. *The Oceanographer's Companion*. CRC Press, 2017. ISBN 978-1-4987-7306-5.

McCue, L. Putting vessel motion research into the hands of operators. In *Proc. 11th International Conference on the Stability of Ships and Ocean Vehicles*, Athens, Greece, September 2012.

McCue, L. On the use of mobile apps for improved maritime safety. In *Safety and energy efficiency in river transportation for a sustainable development of the peruvian Amazon region*, pages 22–1 – 22–15, Iquitos, Peru, July 2013.

McGoodwin, J. R. Chapter 2: Cultural characteristics of small-scale fishing communities. In *Understanding the Cultures of Fishing Communities: A Key to Fisheries Management and Food Security*. Food and Agriculture Organization (FAO), 2001. ISBN 9-2510-4606-9.

Mégel, J. and Kliava, J. Metacenter and ship stability. *American Journal of Physics*, 78(7): 19–21, 2010. doi:10.1119/1.3285975.

Molland, A. F. Chapter 3 - flotation and stability. In *The Maritime Engineering Reference Book*, pages 75 – 115. Butterworth-Heinemann, Oxford, 2008. doi:10.1016/B978-0-7506-8987-8.00003-2.

Morse, M. D. and Patel, J. M. An efficient and accurate method for evaluating time series similarity. In *Proceedings of the 2007 ACM SIGMOD International Conference on Management of Data*, SIGMOD '07, pages 569–580, New York, NY, USA, 2007. ACM. ISBN 978-1-5959-3686-8. doi:10.1145/1247480.1247544.

Mouser. *Adafruit Raspberry Pi 3 Model B+*, 2019. URL https://www.mouser.co.uk/new/adafruit/adafruit-raspberry-pi3-modelbplus/. [Online; accessed 10 November 2019].

National Data Buoy Center. *Stations Map*, 2018. URL http://www.ndbc.noaa.gov/obs.shtml. [Online; accessed 1 March 2018].

National Instruments. *Understanding FFTs Windowing*, May 2015. URL http://www.ni.com/white-paper/4844/en/. [Online; accessed 3 June 2018].

National Instruments. *PXI-6221 Multifunction I/O Module*, 2019a. URL https://www.ni.com/en-gb/support/model.pxi-6221.html. [Online; accessed 9 April 2018].

National Instruments. *PXI-6704 analog output module*, 2019b. URL https://www.ni.com/en-gb/support/model.pxi-6704.html. [Online; accessed 9 April 2018].

National Instruments. *SCB-68 and SCB-68A : DAQ Multifunction I/O Accessory Guide*, 2019c. URL https://www.ni.com/en-gb/support/documentation/supplemental/17/scb-68-and-scb-68a---daq-multifunction-i-o-accessory-guide.html. [Online; accessed 19 September 2019].

National Instruments. *NI 7330/7340/7350 Motion Controllers and P7000 Series Stepper Drives*, 2019d. URL http://www.ni.com/pdf/manuals/372324d. [Online; accessed 9 April 2018].

National Instruments. *MID-7604/7602 Stepper Power Motor Drive*, 2019e. URL http://www.ni.com/pdf/manuals/372454g.pdf. [Online; accessed 9 April 2018].

National Instruments. *PXI-8101 embedded controller*, 2019f. URL https://www.ni.com/en-gb/support/model.pxie-8101.html. [Online; accessed 9 April 2018].

National Instruments. *PXI-1036 PXI Chassis (Legacy)*, 2019g. URL https://www.ni.com/en-gb/support/model.pxi-1036.html. [Online; accessed 9 April 2018].

National Semiconductor Corporation. *Power Spectra Estimation*, 1980. URL http://www.dcs.warwick.ac.uk/~feng/teaching/PowerSpectrum.pdf. [Online; accessed 1 March 2018].

Negri, L. H. *PeakUtils*, 2016. URL https://pypi.python.org/pypi/PeakUtils. [Online; accessed 3 June 2018].

Noel, J. V., editor. *Knight's Modern Seamanship.* John Wiley and Sons, 18th edition, 1989. ISBN 0-4712-8948-5.

Nowacki, H. and Ferreiro, L. D. *Historical Roots of the Theory of Hydrostatic Stability of Ships*, pages 141–180. Springer Netherlands, Dordrecht, 2011. doi:10.1007/978-94-007-1482-3_8.

Nunez, J. M., Araujo, M. G., and Garcia-Tunon, I. Real-Time Telemetry System for Monitoring Motion of Ships Based on Inertial Sensors. *Sensors*, 17(5), 2017. doi:10.3390/s17050948.

Oakley, O. H., Paulling, J. R., and Wood, P. D. Ship motions and capsizing in astern seas. In Cooper, R. D. and Doroff, S. W., editors, *Tenth Symposium on Naval Hydrodynamics - Hydrodynamics for Safety*, chapter IV, pages 297–350. Office of Naval Research, Department of the Navy, Cambridge, Massachusetts, 1974.

Oppenheim, A. V., Schafer, R. W., and Buck, J. R. *Discrete-Time Signal Processing.* Prentice-Hall Inc, New Jersey, USA, 2nd edition, 1999. ISBN 0-1375-4920-2.

O'Reilly, P. J. F. Aircraft/Deck Interface Dynamics for Destroyers. *Marine Technology*, 24(1): 15–25, 1987.

Ortmeyer, C. *Then and Now. A Brief History of Single Board Computers*. Technical Report 6, ElectronicDesign, 2014. URL http://www.newark.com/wcsstore/ExtendedSitesCatalogAssetStore/cms/asset/pdf/americas/common/NE14-ElectronicDesignUncovered-Dec14.pdf. [Online; accessed 13 April 2018].

Paroka, D. and Umeda, N. Effect of freeboard and metacentric height on capsizing probability of purse seiners in irregular beam seas. *Journal of Marine Science and Technology*, 12(3):150 – 159, 2017. doi:10.1007/s00773-007-0247-8.

Pascoal, R. and Soares, C. G. Non-parametric wave spectral estimation using vessel motions. *Applied Ocean Research*, 30(1):46–53, 2008.

Patterson, C. and Ridley, J. *Ship Stability, Powering and Resistance*, volume 13. Bloomsbury, 2014. ISBN 1-4081-7612-2.

PCB Piezotronics MTS Systems Corporation. *Accelerometer Model 352C22*, 2016. URL https://www.pcb.com/Products/model/352C22. [Online; accessed 3 June 2018].

Pololu Robotics and Electronics. *MinIMU-9 v3 Gyro, Accelerometer, and Compass (L3GD20H and LSM303D Carrier)*, 2016. URL https://www.pololu.com/product/2468. [Online; accessed 3 June 2018].

Qualisys Motion Capture Systems. *Qualisys Mocap System Summary and Purchasing information*, 2016. URL http://teachers.d11.org/teachers/wybrasr/Shared%20Documents/FlightGrantQuotes/QualisysInfo.pdf. [Online; accessed 3 June 2018].

Qualisys Motion Capture Systems. *Oqus Cameras*, 2018. URL https://www.qualisys.com/cameras/oqus/#tech-specs. [Online; accessed 27 June 2018].

Radner, W., Diendorfer, G., Kainrath, B., and Kollmitzer, C. The accuracy of reading speed measurement by stopwatch versus measurement with an automated computer program (rad-rd). *Acta Ophthalmologica*, 95(2):211–216, 2017. doi:10.1111/aos.13201. URL https://onlinelibrary.wiley.com/doi/abs/10.1111/aos.13201.

Raspberry Pi Foundation. *Raspberry Pi 2 Model B*, 2015. URL https://www.raspberrypi.org/products/raspberry-pi-2-model-b/. [Online; accessed 3 June 2018].

RaspberryPi.org. *Setting up a Raspberry Pi as a Wireless Access Point*, 2019a. URL https://www.raspberrypi.org/documentation/configuration/wireless/access-point.md. [Online; accessed 9 April 2018].

RaspberryPi.org. *Downloads*, 2019b. URL https://www.raspberrypi.org/downloads/. [Online; accessed 9 April 2018].

Roberts, S. E. Hazardous occupations in great britain. *The Lancet*, 360(9332):543 – 544, 2002. doi:10.1016/S0140-6736(02)09708-8.

Rodri-guez Martin, D., Perez-Lopez, C., Sama, A., Cabestany, J., and Catala, A. A wearable inertial measurement unit for long-term monitoring in the dependency care area. *Sensors*, 13 (10):14079–14104, 2013. doi:10.3390/s131014079.

Rojas, P., Abad, L., Arribas, F. P., and Arias, C. Some experimental results on the stability of fishing vessels. In *8th International Conference on the Stability of Ships and Ocean Vehicles*. CROMO IMAGEN, 2003.

Rye, H. The stability of some currently used wave parameters. *Coastal Engineering*, 1:17 – 30, 1977. doi:10.1016/0378-3839(77)90004-7.

Salim, M. S., Lim, H. N., Salim, M. S. M., and Baharuddin, M. Y. Motion analysis of arm movement during badminton smash. In *Biomedical Engineering and Sciences (IECBES), 2010 IEEE EMBS Conference on*, pages 111–114, Kuala Lumpur, Malaysia, 30 Nov - 2 Dec 2010. doi:10.1109/IECBES.2010.5742210.

SBG Systems. *Ekinox Series; Tactical Grade MEMS Inertial Systems*, 2017. URL http://www.sbg-systems.com/docs/Ekinox_Series_Leaflet.pdf. [Online; accessed 2 March 2018].

Scarponi, M. Use of the wolfson stability guidance for appraising the operational stability of small fishing vessels. In *Proceedings of the 16th International Ship Stability Workshop*, Belgrade, Serbia, 5 - 7 June 2017.

Schoonderwaldt, E. and Thompson, D. *Learn about 6DOF*, 2016. URL https://www.qualisys.com/webinars/learn-about-6dof/. [Online; accessed 27 June 2018].

Schuster, A. On the investigation of hidden periodicities with application to a supposed 26 day period of meteorological phenomena. *Terrestrial Magnetism*, 3(1):13–41, March 1898. doi:10.1029/TM003i001p00013.

SciPy. *Remove linear trend along axis from data*, 2014. URL http://docs.scipy.org/doc/scipy-0.14.0/reference/generated/scipy.signal.detrend.html#scipy.signal.detrend. [Online; accessed 3 June 2018].

Scipy. *Estimate power spectral density using Welch's method*, 2014. URL https://docs.scipy.org/doc/scipy-0.14.0/reference/generated/scipy.signal.welch.html. [Online; accessed 3 June 2018].

Seaman, A. and McPhee, J. Comparison of optical and inertial tracking of full golf swings. *Procedia Engineering*, 34:461 – 466, 2012. doi:https://doi.org/10.1016/j.proeng.2012.04.079.

Sen, D. T. and Vinh, T. C. Determination of added mass and inertia moment of marine ships moving in 6 degrees of freedom. *International Journal of Transportation Engineering and Technology*, 2(1):8 – 14, 2016. doi:10.11648/j.ijtet.20160201.12.

Sevgi, L. Numerical Fourier Transfroms: DFT and FFT. *IEEE Antennas and Propagation Magazine*, 49(3):238–243, June 2007. URL https://ieeexplore.ieee.org/stamp/stamp.jsp?arnumber=4293982.

Shin, K.-Y. and Mun, J. H. A multi-camera calibration method using a 3-axis frame and wand. *International Journal of Precision Engineering and Manufacturing*, 13(2):283–289, Feb 2012.

Simpson, L. and Lamb, R. *IoT: Looking at sensors*. Technical report, Jefferies Equity Research, 2014.

Slant. *What are the best single-board computers?*, 2018. URL https://www.slant.co/topics/1629/~single-board-computers. [Online; accessed 3 June 2018].

Smith, S. W. *Digital Signal Processing: A Practical Guide for Engineers and Scientists.* Newnes, 2003.

ST Microelectronics. *LIS331DL MEMS motion sensor: 3-axis smart digital output accelerometer datasheet*, 2007. URL http://www.digchip.com/datasheets/parts/datasheet/456/LIS331DL-pdf.php. [Online; accessed 17 May 2018].

ST Microelectronics. *L3G4200D MEMS motion sensor: three-axis digital output gyroscope datasheet*, 2010. URL http://www.digchip.com/datasheets/parts/datasheet/456/L3G4200D-pdf.php. [Online; accessed 17 May 2018].

ST Microelectronics. *LSM303DLHC:Ultra-compact high-performance eCompass module: 3D accelerometer and 3D magnetometer Datasheet* [Online; accessed 2 March 2018], 2013. URL http://www.st.com/content/ccc/resource/technical/document/datasheet/56/ec/ac/de/28/21/4d/48/DM00027543.pdf/files/DM00027543.pdf/jcr:content/translations/en.DM00027543.pdf. [Online; accessed 1 June 2018].

ST Microelectronics. *LSM9DS1 - iNEMO inertial module:3D accelerometer, 3D gyroscope, 3D magnetometer datasheet*, 2016. URL http://www.st.com/en/mems-and-sensors/lsm9ds1.html. [Online; accessed 11 February 2018].

Terada, D., Tamashima, M., Nakao, I., and Matsuda, A. Estimation of the metacentric height by using onboard monitoring roll data based on time series analysis. In *Proceedings of the 15th International Ship Stability Workshop*, Stockholm, Sweden, 13 - 15 June 2016.

The Pi Hut. *WiFi Dongle - Ultra Long Range High Gain w/ 5dBi Antenna*, 2018. URL https://thepihut.com/products/wifi-dongle-ultra-long-range-high-gain-w-5dbi-antenna. [Online; accessed 9 April 2018].

The Pi Hut. *Raspberry Pi 3 Model B+*, 2019. URL https://thepihut.com/products/raspberry-pi-3-model-b-plus?src=raspberrypi. [Online; accessed 9 April 2018].

The Pi Hut. *Adafruit PiRTC - PCF8523 Real Time Clock for Raspberry Pi*, 2021. URL https://thepihut.com/products/adafruit-pirtc-pcf8523-real-time-clock-for-raspberry-pi. [Online; accessed 9 April 2021].

Thomas, B. E., John, S., and Abe, S. Power spectral density computation using modified welch method. *International Journal of Science Technology and Engineering (IJSTE)*, 2(4), October 2015.

Titus, J. Build 'dyna-micro', an 8080 microcomputer. *Radio-Electronics*, pages 33 – 36, 1976.

Totem Plus. *Integrated Monitoring, Alarm and Control Systems*, 2015. URL http://www.totemplus.com. [Online; accessed 1 June 2018].

Tuck, K. *The Trade-off Between High Resolution and Low Power Using Oversampling Modes*, 2010. URL http://cache.freescale.com/files/sensors/doc/app_note/AN4075.pdf. [Online; accessed 10 March 2018].

Tupper, E. *Introduction to Naval Architecture*. Butterworth-Heinemann, 3rd edition, 1996. ISBN 0-7506-2529-5.

Ueng, S. Physical Models for Simulating Ship Stability and Hydrostatic Motions. *Journal of Marine Science and Technology*, 21(6):674–685, 2013. doi:10.6119/JMST-012-1121-1.

Umeda, N., Takaishi, Y., Matsuda, A., Suzuki, S., Watanabe, K., Hamamoto, M., Chiba, Y., Sera, W., and Spyrou, K. Model experiments of ship capsize in astern seas. *Journal of the Society of Naval Architects of Japan*, 177, 1995.

US Bureau of Labour Statistics. *National census of fatal occupational injuries in 2016*, 2017. URL https://www.bls.gov/news.release/pdf/cfoi.pdf. [Online; accessed 3 June 2018].

Walker, J. *Fast Fourier Transforms, Second Edition*. Studies in Advanced Mathematics. Taylor and Francis, 1996. ISBN 978-0-8493-7163-9.

Wawrzynski, W. and Krata, P. Method for ship's rolling period prediction with regard to non-linearity of GZ curve. *Journal of Theoretical and Applied Mechanics*, 54(4):1329 – 1343, 2016. doi:10.15632/jtam-pl.54.4.1329.

Weisstein, E. W. Fourier series. In *MathWorld - A Wolfram Web Resource*, 2018. URL http://mathworld.wolfram.com/FourierSeries.html.

Welch, P. D. The use of fast fourier transform for the estimation of power spectra: A method based on time averaging over short, modified periodograms. *IEEE Trans. Audio and Electroacoust*, 15(2):70 – 73, 1967.

Wolfson Unit. *Research Project 560: Simplified Presentation of FV Stability Information for Vessels 12 m Registered Length and Over*. Final Report 1905/2, Maritime and Coastguard Agency, 2006. URL http://www.wumtia.soton.ac.uk/sites/default/files/1905_2bd.pdf. [Online; accessed 1 March 2018].

Wolfson Unit. *Model Basins*, 2016. URL http://www.wumtia.soton.ac.uk/facilities/model-basins. [Online; accessed 2 June 2018].

Womack, J. and Johnson, B. *A Guide to Fishing Vessel Stability*. Technical and Research Bulletin 4-24, Society of Naval Architects and Marine Engineers, 2004. URL https://www.ntsb.gov/news/events/Documents/2010_Fishing_Vessel_Safety_FRM-2-SNAMEGuidetoFVStability07-14-04.pdf. [Online; accessed 1 March 2018].

Woodward, M. D., van Rijsbergen, M., Hutchinson, K. W., and Scott, A. Uncertainty analysis procedure for the ship inclining experiment. *Ocean Engineering*, 114:79 – 86, 2016. doi:10.1016/j.oceaneng.2016.01.017.

Yaakob, O., Hashim, F. E., Jalal, M. R., and Mustapa, M. A. Stability, seakeeping and safety assessment of small fishing boats operating in southern coast of peninsular malaysia. *Journal of Sustainability Science and Management*, 10(1):50 – 65, 2015.

Young, P. and Barrass, B. *Ship stability: Notes and Examples*. Butterworth-Heinemann, 3rd edition, 2001. ISBN 0-7506-4850-3.